Atoms, Molecules and Clusters in Intense Laser Fields

by

Zachary B. Walters

B.S., Harvey Mudd College, 2002

A thesis submitted to the

Faculty of the Graduate School of the

University of Colorado in partial fulfillment

of the requirements for the degree of

Doctor of Philosophy

Department of Physics

2009

This thesis entitled:
Atoms, Molecules and Clusters in Intense Laser Fields
written by Zachary B. Walters
has been approved for the Department of Physics

Chris H. Greene

Murray Holland

Date

The final copy of this thesis has been examined by the signatories, and we find that both the content and the form meet acceptable presentation standards of scholarly work in the above mentioned discipline.

Walters, Zachary B. (Ph.D., Physics)

Atoms, Molecules and Clusters in Intense Laser Fields

Thesis directed by Chris H. Greene

Recent advances in the technology of intense, short laser pulses have opened the possibility of investigating processes in atoms, molecules and clusters in which the normal intramolecular forces between electrons and nuclei, and between different electrons, are rivaled in strength by interactions with the driving laser, or with a cluster plasma. Experiments using rescattered electrons offer a means of probing atomic and molecular processes on ultrafast timescales.

This thesis extends techniques and concepts of atomic and molecular physics to describe physics in the strong field regime. This involves investigating how electron scattering from atoms and molecules is affected by the intense and time-varying electric field of the laser, the effect of such scattering on experimental observables, and the role of intramolecular structure on strong field processes.

Also investigated is the evolution of van der Waals atomic clusters when subject to intense laser pulses in the VUV regime. Here processes such as photoionization, inverse bremsstrahlung heating, and collisional ionization and recombination are affected both by the non-hydrogenic nature of the relevant atomic potentials but also by the screening of these potentials by the cluster plasma.

Dedication

To my family.

Acknowledgements

Many people helped make this thesis possible, and I would like to express my gratitude to them all. More than anyone, I must thank my advisor, Chris Greene, for many patient years as a teacher and mentor. Along with his unparalleled knowledge of atomic and molecular physics, Chris has a wonderful grasp of the subtle art of turning a physical insight into a physical theory.

Physics can be a talkative subject, and there are many people I would like to thank on this front. Robin Santra, Seth Rittenhouse, Nirav Mehta, Jose D'Incao, Stefano Tonzani, Roman Curik, Dan Haxton, Javier von Stecher, Jia Wang, Josh Dunn and Heather Crowell were all members of the Greene group during my graduate career, and I would like to thank each of them for many animated hours in front of a whiteboard during my graduate career. Ed Meyer also deserves thanks for his helpful explanations of quantum chemistry.

Much of the work in this thesis was inspired by experiments performed by the group of Henry Kapteyn and Margaret Murnane. Aside from Henry and Margaret, I would like to thank Nick Wagner, Andrea Wuest, Robynne Lock, Wen Li and Xibin Zhou for many stimulating and informative discussions.

Pete Ruprecht had the sometimes thankless task of keeping all the computers working, and has been a fount of useful information about programming issues.

Finally I would like to thank Pam Leland for her administrative support.

The funding for this research was provided by the Department of Energy and the National Science Foundation Extreme Ultraviolet Engineering Research Center. Computational support was provided by the W.M. Keck Foundation.

Contents

Chapter

Figures

Figure

Chapter 1

Introduction and Physical Principles

Under normal circumstances, an atom or a molecule passes through space like a passenger train speeding through the night. As a passenger on the train, interactions with other passengers are direct and immediate. No two passengers may sit in the same seat, and one may be attracted to some passengers and repelled from others. Some passengers may be liable to move about the cars, while others may spend the entire journey dozing in the same seat.

In contrast, the outside world is experienced at one remove. If one side of the train has a particularly stunning view, you might turn to look at it while still maintaining your distance from the crying baby in front of you and your proximity to the interesting conversationalist in the back. Likewise, if a fellow passenger disembarks you might settle happily into his seat while caring nothing about which station he left at or why. Most of the time, atomic and molecular physics works in the same way. The forces between electrons and nuclei, or between different electrons in the same atom completely dominate anything the outside world can bring to bear.

Much of the interest of intense laser-target interactions is that the interaction with the outside world – in this case with the field imposed by the laser – can rival the strength of the interactions within the original system. To return to the train metaphor, suppose the glare from the rising sun made sitting on one side of the car extremely irritating. Even though all passengers relate to one another in the same way,

the seating arrangement might end up entirely different. If the train were following a switchback, causing the glare to alternate which sides of the train it affected, the resulting arrangement of passengers might be extremely complex and time dependent.

In contrast to the molecule-centric perspective of AMO physics, strong field physics might occasionally be accused of ignoring atoms and molecules completely. Primarily concerned with the ways in which electrons interact with the strong electromagnetic fields encountered in an intense laser beam, frequently used theories often treat atoms and molecules as an afterthought, a generic coulomb potential which alters a few results in non-essential ways. Two examples of this will be seen in later chapters. In semiclassical theories of high harmonic generation, encountered in Chapter 4 the Coulomb potential slightly alters the trajectories which contribute to a particular harmonic, but play little role in the intensity of that harmonic or the energy at which the spectrum dies off. If the laser should happen to hit a cluster and create a nanoscale plasma as in Chapter 5, the treatment of that plasma is not particularly different if the individual atoms are xenon than if they were hydrogen.

A major goal of this thesis has been to unite these two perspectives: to do atomic and molecular physics in a regime where external forces rival internal forces in strength, or strong field physics in a way where the individual characteristics of particular atoms and molecules may be accounted for.

Because this is such a broad topic, no thesis can hope to describe all cases of interest. In the pages that follow, different aspects of the laser-target interaction will be dealt with in problem-specific ways. A common theme will be that the identity of a particular atom or molecule makes itself important when continuum electrons scatter from that particle. Far from the particle, there is little to distinguish one ion of a particular charge from another; it is only when an electron feels a short range potential that the identity of the particle becomes significant.

In the region close to the molecule, internal forces dominate. The electronic part

of a molecular wavefunction will consist of many core electrons which are contained in deeply bound orbitals, plus a few electrons contained in less deeply bound valence orbitals. Because these valence electrons are screened from the nuclear potentials by the core electrons, they are much freer to rearrange themselves when subject to the field of a strong laser.

It is readily apparent that a full treatment of the dynamics of such a system will rapidly become intractable. Because every new particle in the system introduces three new spatial degrees of freedom, a simple nitrogen molecule will already require 14*3=42 dimensions for the electronic wavefunctions alone! For this reason, most current theories of strong field physics prefer to work with as few active electrons as possible, and usually only the electron in the highest occupied molecular orbital (HOMO) is allowed to respond to the laser field.

This lone electron will then feel a strong but local potential due to interactions with the parent ion, plus a weaker (typically on the order of a few tenths or hundredths of an atomic unit) but long range electric field applied by the driving laser. Far from the molecule, the oscillating electric field becomes the dominant force felt by the electron.

Because the effects of the parent ion are felt only at short range, the interactions of molecules with intense lasers share many characteristics regardless of the choice of molecule. These characteristics can be explained semiclassically using the three step model introduced by Paul Corkum [7, 33]. In this model, electrons enter the continuum by tunneling away from the parent ion, then follow classical trajectories in the oscillating laser field before recolliding with the parent ion. Because the electron is being accelerated by the electric field of the laser , it can have a much greater energy at the time of recollision than at the time of tunneling. If the electron then recollides with the parent ion, it can emit a photon with an energy much higher than the frequency of the driving laser. Alternatively, the electron may scatter elastically from the ion and be accelerated once again by the driving laser, or it can scatter inelastically and liberate

additional electrons from the parent ion.

The three step model is at its best in describing the evolution of the electron while it is far away from the parent ion, and in describing gross features of the experimental observables. Because the tunneling and rescattering both occur at the location of the parent ion, there are calculable maximum energies of the electron at the time of recollision, and after scattering from the parent ion. However, the semiclassical approximations at the heart of the three step model will be at their worst in describing the electron in the vicinity of the parent ion, where the potential of the parent ion becomes paramount and the classical trajectories become very complicated. More sophisticated treatments of scattering are necessary to adequately describe this terminal phase.

Chapters 2 and 3 are concerned with details of the rescattering process. Chapter 2 addresses the question of how scattering features such as shape resonances are affected by the intense, time dependent field of the laser. Chapter 3 addresses the question of how electron-molecule scattering affects efforts such as molecular tomography, which attempt to reconstruct molecular properties from experimental data.

Chapter 4 moves beyond the single active electron model to consider the evolution of the molecule's vibrational wavefunction during the high harmonic process. In addition, the three step Corkum model is extended to connect with more sophisticated short range models of electron-molecule scattering, thereby helping to unify the molecule-centric and strong field-centric approaches to HHG.

Chapter 5 deals with the problem of an atomic cluster in an intense beam of x-rays. In contrast with earlier chapters, here only single photon processes are important. The complications arise due to the dense and rapidly heating cluster plasma which develops during the course of the pulse. This plasma acts to screen the atomic electrons, lowering the binding energies and affecting cross sections for photoionization and inverse bremsstrahlung heating.

Chapter 2

Scattering Resonances in the Presence of Intense Laser Fields

A central feature of many current efforts to probe molecular properties on ultrafast timescales is the use of rescattered electrons as probes. Rescattering [7] occurs when an electron tunnels free from a parent ion, accelerates in the field of the driving laser, then recollides with the parent ion. Information about the molecule may then be found by monitoring various scattering output channels. If the electron recollides with the parent ion, its high kinetic energy results in the emission of very high energy photons. Alternatively, the electron may scatter elastically from the target or cause the target to break up into two or more fragments. Understanding the scattering process is thus a necessary step in interpreting rescattering experiments.

Aside from its experimental relevance, the rescattering process is interesting in its own right, as an exotic variant of scattering. Because rescattering necessarily takes place in the presence of an intense, time varying laser field, familiar results from zero field, time independent calculations may be altered in the context of strong field physics. This chapter investigates the familiar concepts of shape resonances and potential barriers in the context of a rescattering experiment.

Commonly encountered in scattering physics, a shape resonance consists of a quasi-bound state at positive energy. A potential barrier traps the scattering particle in a local potential well, where it may survive for a long time before tunneling through the barrier to the continuum. The scattering wavefunction will often have a very large

amplitude in the region behind the potential barrier over large energy ranges, with correspondingly large effects on experimental observables such as photoionization or -recombination cross sections [55].

The presence of a strong laser field complicates the static view of shape resonances. In the static limit, potential barriers may be wiped out by the strength of the applied field at times during the laser cycle. Furthermore, in a time dependent treatment, nonadiabatic coupling between scattering channels could limit the buildup of the scattering wavefunction near the target, thereby diluting the impact of a resonance in a particular channel.

This chapter addresses the phenomenon of shape resonance in high harmonic generation. It uses novel doubly adiabatic potential energy curves which illuminate the effects of a strong field on energy barriers in particular channels[14]. These curves are then used to construct a basis for the propagation of the time-dependent Schrödinger equation. Finally, the effects of a shape resonance on a high harmonic spectrum are shown by comparing high harmonic spectra which are affected by a shape resonance to spectra which are not affected.

In the single active electron approximation, the Hamiltonian for an electron in the presence of a spherically symmetric atomic potential U(r) and an external laser electric field of strength $F(t)$ is given by

$$\hat{H} = \hat{T}_r + \hat{L}^2/(2r^2) + V(r) + F(t)r\cos(\theta) = \hat{T}_r + \hat{H}|_{(r,t)} \tag{2.1}$$

Time dependent adiabatic channel functions and potential energy curves may be found by diagonalizing $\hat{H}|_{(r,t)}$ at every value of (r,t)

$$\hat{H}|_{(r,t)}\phi_\mu(r,t,\Omega) = U_\mu(r,t)\phi_\mu(r,t,\Omega). \tag{2.2}$$

We perform this diagonalization in a spherical harmonic basis

$$\phi_\mu(r,t,\Omega) = \sum_{l=0}^{l_{\max}} A_l^\mu(r,t)Y_{l0}(\Omega). \tag{2.3}$$

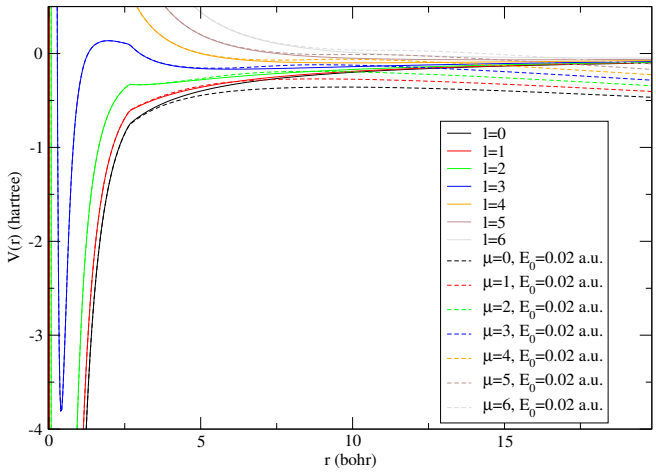

Figure 2.1: Adiabatic potential energy curves for Cs^+, calculated for $E_0 = 0$ and $E_0 = .02$. The potential curves depart from each other at long range, but are largely unaffected in the region of the f-wave potential energy well.

Because cylindrical symmetry is not broken, $m = 0$ always.

In the limit that $F(t) \to 0$, the problem reduces to the familiar case of an atom in isolation, with $A_l^\mu(r,t) \to \delta_{l,\mu}$ and $U_\mu(r) \to (\frac{l(l+1)}{2r^2} + V(r))\delta_{l,\mu}$.

The resulting potential energy curves serve to give insight into whether the shape resonance survives the presence of an intense electric field. Figure 2.1 shows the potential energy curves for Cs^+ at various electric field strengths, and at various points in the laser cycle.

As time goes by, this picture is complicated by the changing $F(t)$, which has the effect of mixing the different channels together. The time dependent Schrödinger equation is written as an infinite, truncatable set of coupled differential equations

$$[i\partial/\partial t - \hat{T}_r - U_\mu]F_\mu(r,t) = -\sum_v [\frac{1}{2}Q_{\mu\nu}(r,t) + W_{\mu\nu}(r,t) + P_{\mu\nu}(r,t)\partial/\partial r]F_\nu(r,t) \quad (2.4)$$

where $P_{\mu\nu} =<< \phi_\mu(r,t,\Omega)|\frac{\partial}{\partial r}\phi_\nu(r,t,\Omega) >>$ is the radial nonadiabatic coupling and $W_{\mu\nu} =<< \phi_\mu(r,t,\Omega)|\frac{\partial}{\partial t}\phi_\nu(r,t,\Omega) >>$ is the temporal nonadiabatic coupling. By the Hellman-Feynman theorem, $P_{\mu\nu} = 3F(t)C_{\mu\nu}(r,t)$, and $W_{\mu\nu}(r,t) = r\dot{F}(t)C_{\mu\nu}(r,t)$,

where

$$C_{\mu\nu}(r,t) = \begin{cases} \frac{<<\phi_\mu(r,t,\Omega)|\cos(\theta)|\phi_\nu(r,t,\Omega)>>}{U_\nu(r,t)-U_\mu(r,t)} & \mu \neq \nu \\ 0 & \mu = \nu \end{cases} \tag{2.5}$$

The coupling due to the electric field is given by $F(t)Z_{\mu\nu}$, where $Z_{\mu\nu} = r(U_\nu(r,t) - U_\mu(r,t))C_{\mu\nu}(r,t)$. It is worth noting that the $C_{\mu\nu}(r,t)$ term which appears in the electric field and the nonadiabatic couplings will be finite for finite r. At zero field, $U_\mu(r) \rightarrow (\frac{l(l+1)}{2r^2} + V(r))\delta_{l,\mu}$ and the energy denominator $U_\mu(r,t) - U_\nu(r,t) \rightarrow \delta_{l,\mu}\delta_{l',\nu}\frac{l(l+1)-l'(l'+1)}{2r^2}$. When the field is nonzero, $U_\mu(r,t)$ and $U_\nu(r,t)$ for $\mu \neq \nu$ are distinct eigenvalues of the irreducible (since m is restricted to be 0) Hamiltonian. Thus $U_\mu(r,t) \neq U_\nu(r,t)$ and the resulting nonadiabatic couplings are finite.

In order to avoid time-dependent channel functions and couplings, time propagation was performed in the basis

$$\chi_\alpha(r,\Omega) = \sum_\mu F_\mu^{(\alpha)}(r)\phi_\mu(r,\Omega) \tag{2.6}$$

of eigenfunctions of the Hamiltonian calculated with the field at maximum strength and setting $W_{\mu\nu} = 0$. Here the time-independent Schrödinger equation is given by

$$(E_\alpha - \hat{T}_r - U_\mu)F_\mu^{(\alpha)}(r,t) = -\sum_\nu (\frac{1}{2}Q_{\mu\nu}(r) + P_{\mu\nu}(r)\partial/\partial r)F_\nu^{(\alpha)}(r,t), \tag{2.7}$$

where E_α is the energy eigenvalue corresponding to basis state $\chi_\alpha(r,\Omega)$.

This calculation was performed using FEM-DVR basis functions[45]. These functions are orthonormal in the limit of Gauss-Lobatto quadrature and yield a banded matrix for the kinetic energy operator $\hat{T}_r$. Herman-Skillman atomic potentials [22] were used for $V(r)$. In addition, a complex absorbing potential was added in order to absorb flux past a cutoff point. The resulting Hamiltonians were therefore sparse and complex symmetric but not Hermitian. Use of the non-Hermitian Hamiltonian requires use of a different orthogonality relation: $\langle\phi_\mu^*|\,|\phi_\nu\rangle = \delta_{\mu,\nu}$, where the extra conjugation on the left-hand function causes the unconjugated function to appear in the integral[50].

In the following calculations, an initial wavefunction was found by diagonalizing the field-off Hamiltonian, then projected onto a basis of eigenfunctions of the field-on Hamiltonian, calculated at the maximum of the electric field strength. For the field strengths ($E_0 \leq 0.02$) used in these calculations, the field-on basis was truncated using an energy cutoff of 4 hartree. As this energy is far above the harmonic and above threshold ionization cutoffs for these fields, such a cutoff should not affect the calculated spectra, and changing the cutoff from 4 to 8 hartree did not affect the results.

High harmonic spectra were calculated by taking the Fourier transform of the time-dependent recombination dipole $d(t) = \langle \psi_g | \, z \, | \psi(t) \rangle$. The resulting HHG spectra for hydrogen is compared with results found in [28] in Figure 2.2, which was found using a different form of the dipole $d(t) = \langle \psi(t) | \, z \, | \psi(t) \rangle$. The disagreement is of the same order as was found in [28] to arise between the different forms of the dipole.

Several difficulties arise when trying to extract scattering information from an observable such as the high harmonic spectrum. These difficulties arise from the complex complex rescattering wavefunction, which must undergo a complicated evolution between the initial state and recollision. In order to contribute to $d(\omega)$, an electron must tunnel free of the parent ion and propagate in the continuum before colliding once again with the parent ion. Furthermore, there are two times during any laser cycle when the original tunneling may occur, and these times will vary as the intensity envelope increases or decreases. As a result, the recolliding wavefunction will have a complex nature which will not be easy to separate from the high harmonic spectrum in order to find the recombination dipole. An additional practical problem arises from the comblike nature of the spectrum: information from most scattering energies will be lost due to destructive interference between photons produced during different half-cycles of the laser pulse. Thus, scattering properties reconstructed from the harmonic spectrum will have data points separated by 2ω, making it difficult to resolve narrow scattering features. For a typical titanium-sapphire laser with driving wavelength 800 nm, $\omega = 0.0565$

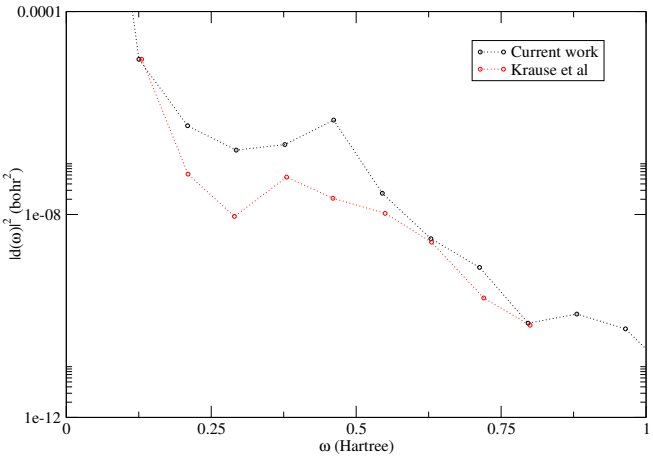

Figure 2.2: Comparison between recombination dipole calculated in this work and by Krause et al [28].

hartree, making the spacing between adjacent harmonics equal to 0.113 hartree = 3 eV. For this reason, it would be desirable to perform such experiments using as small a value for ω as possible.

In order to minimize the effects of the continuum wavefunction, it is desirable to compare two harmonic spectra with similar rescattering wavefunctions, but which result from recombination into different orbitals. The effects of the rescattering wavefunction can then be minimized by examining the ratio of the spectra as a function of the rescattering electron energy $E_{\text{scat}} = w - Ip$.

As will be shown in Chapter 4, the structure of the rescattering wavefunction is primarily determined by the local potential felt by the electron at the time of rescattering; the impact of the initial orbital is mostly felt in the amplitude of the rescattering wavefunction and an overall phase. For this reason, high harmonic spectra were calculated for two exited states of Cs^+: $5p^5 6s^1$ and $5p^5 5d^1$, hereafter referred to as the s state and d state, respectively. The potential experienced by these electrons was approximated by a Herman Skillman potential which gave the bound state energy for the d orbital as 0.24 H, compared with 0.30 for the s orbital. Due to the similarity in binding energy, the ionization amplitude will be approximately the same as a function of electric field strength for the two electronic states.

These two orbitals were chosen with the goal of seeing the f-wave shape resonance known to exist in xenon-like atoms [54, 55, 56]. Due to dipole selection rules[1] , the resonant f-wave continuum electron can recombine into the d orbital, but not the s.

In the vicinity of xenon, both the d- and f-wave potentials rapidly become more attractive with increasing nuclear charge. The f-wave potentials for a variety of atoms in this region are shown in figure 2.3. By the time that Z=57 for lanthanum, the f-wave potential has become sufficiently attractive to support a bound state. Cs^+ was chosen

[1] Strictly speaking, l is no longer a good quantum number in the presence of the laser's electric field. However, near the atom the channel wavefunctions $\psi_\mu(r, \Omega)$ are nearly diagonal in l, so arguments based on selection rules are useful, if no longer exact.

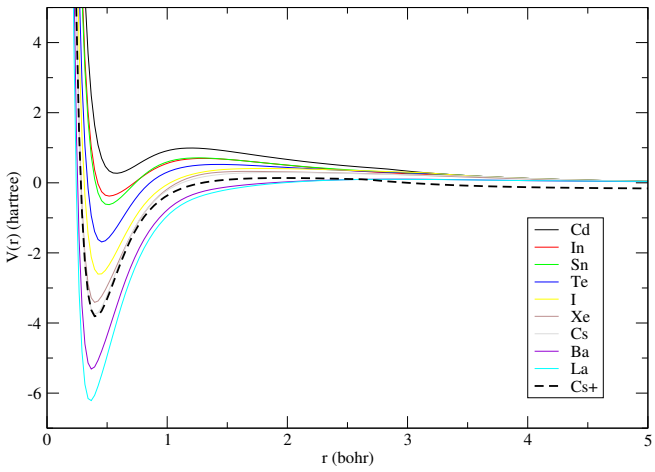

Figure 2.3: In the vicinity of xenon, the f wave potential falls rapidly with increasing nuclear charge. At lanthanum (Z=57), the potential supports a bound state. Here f wave Herman-Skillman potentials, are plotted for a variety of xenon-like atoms.

for the combination of having a relatively deeply bound 5d orbital at 0.23 H and a low energy f-wave resonance, which occurs at a scattering electron energy of 0.1 H. In addition, the relatively weak potential barrier may be affected more strongly by the laser electric field than are the more robust barriers seen in Xe or Cs, thereby increasing the visibility of electric field effects.

The photoionization cross section at zero field for the Cs^+ 5d electron is shown in figure 2.4a, while figure 2.4b shows the p- and d-wave quantum defects. The shape resonance is visible as a peak in the cross section, combined with a Π phase shift in the f-wave quantum defect. Figure 2.5 shows the same information for the 6s photoionization cross section, which does not exhibit a shape resonance.

As an additional aide to understanding the high harmonic spectra, photoionization calculations were made using field-on adiabatic potential energy curves, but neglecting nonadiabatic coupling terms in r and t. The associated angular functions were approximated as pure $Y_{l,0}$ spherical harmonics. The resulting one-dimensional continuum wavefunctions were then normalized by matching the calculated wavefunctions to

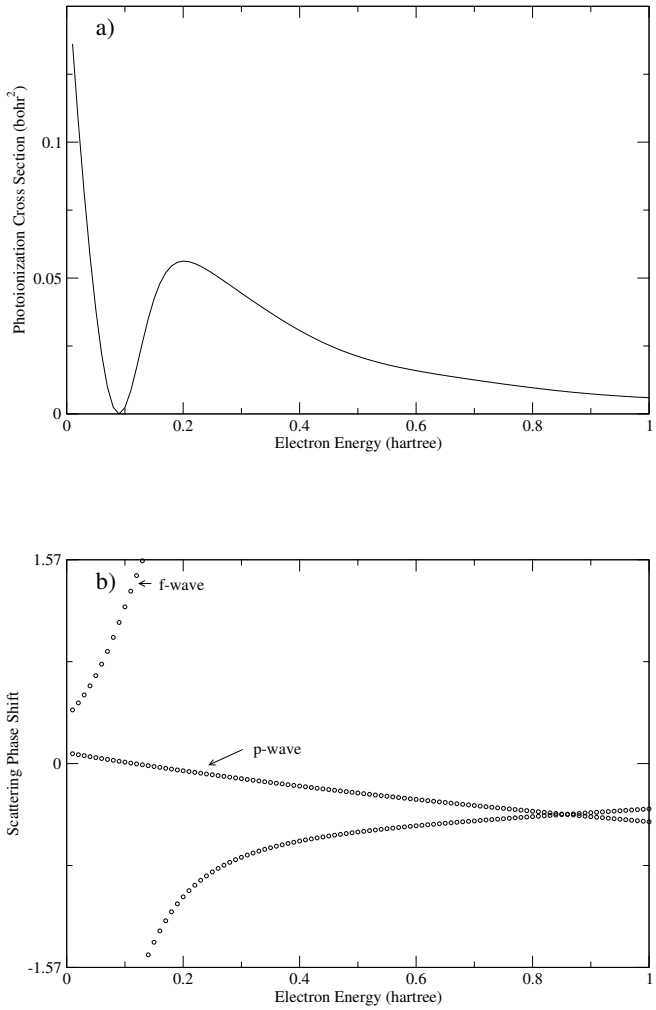

Figure 2.4: a) Photoionization cross section vs energy for the 5d subshell of Cs^+ in the $5p^5 5d^1$ excited state. b) p- and f-wave scattering phase shifts vs energy. The shape resonance corresponds with a change in the f-wave phase shift of π.

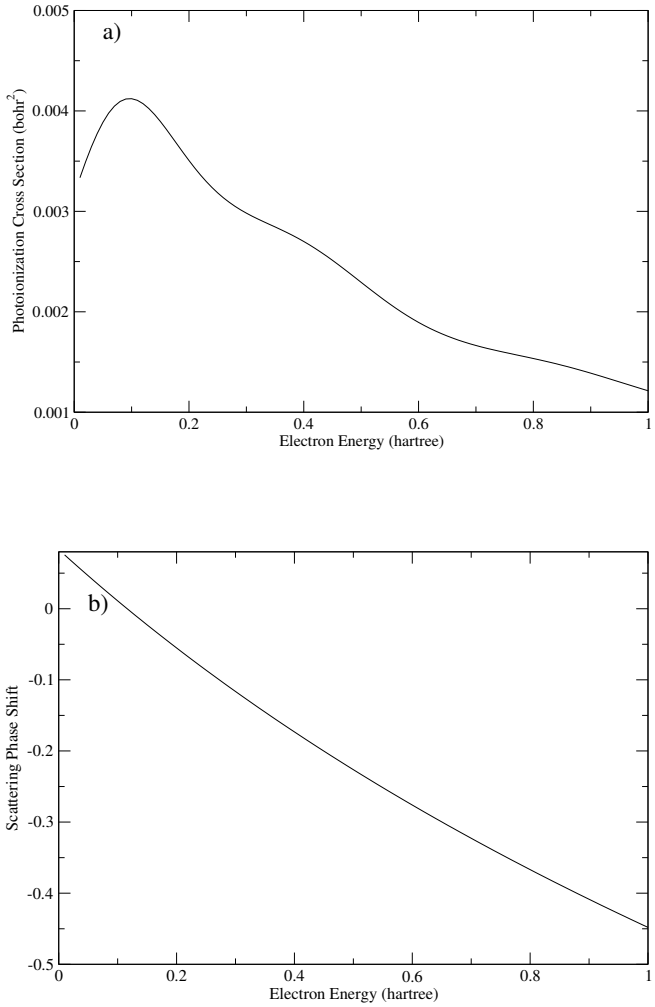

Figure 2.5: a) Photoionization cross section vs energy for the 6s subshell of Cs^+ in the $5p^5 6s^1$ excited state. b) p-wave scattering phase shifts vs energy for Cs^+. In contrast to the 5d shell, no shape resonance effects are present.

to WKB solutions

$$\psi(r') = \sqrt{\frac{2}{\pi k(r')}}(\cos\delta\cos(\int^{r'} k(r)dr) + \sin\delta\sin(\int^{r'} k(r)dr)). \tag{2.8}$$

Although nonadiabatic coupling is necessary for a complete calculation, the single channel calculation illustrates how the relatively slight change to the potential energy curves caused by a nonzero electric field can affect the cross section. Single channel photoionization cross sections are shown for a variety of electric field strengths in figures 2.6 and 2.7. Figure 2.7 uses the peak electric field strengths experienced in the pulse, while figure 2.6 uses lower electric field strengths, consistent with the strength of the field at the time of recollision in the three step model, where the electrons return to the parent ion while the field is near a minimum. Figures 2.6c and 2.7c show the ratios of the d- and s cross sections as a function of the electron scattering energy, the quantity that comparison of high harmonic spectra is intending to find.

Inspecting figures 2.6 and 2.7, it is apparent that the d state photoionization cross section is relatively unaffected by the small electric field strengths used in these calculations. At higher field strengths, the maximum splits into three separate peaks. In contrast, the s state photoionization cross section experiences a much greater change, developing several maxima spaced by approximately 0.2 hartree. At the lower electric field strengths consistent with the field strength at the time of recombination, almost all variation in the d/s comparison spectra comes from changes in the s cross section, while the d cross section undergoes relatively little change.

This pattern is repeated in the d/s ratios as interpolated from the high harmonic spectra shown in figure 2.8. These spectra were made by first integrating the harmonic intensity from $(n - 1/2)\omega$ to $(n + 1/2)\omega$. The logarithms of the resulting intensities were then interpolated as a function of the scattering electron energy $E_{scat} = n\omega - I_p$ to find the envelope of the high harmonic spectrum as a function of energy. The ratio of the recombination dipoles for the d and s spectra was then found by taking the square

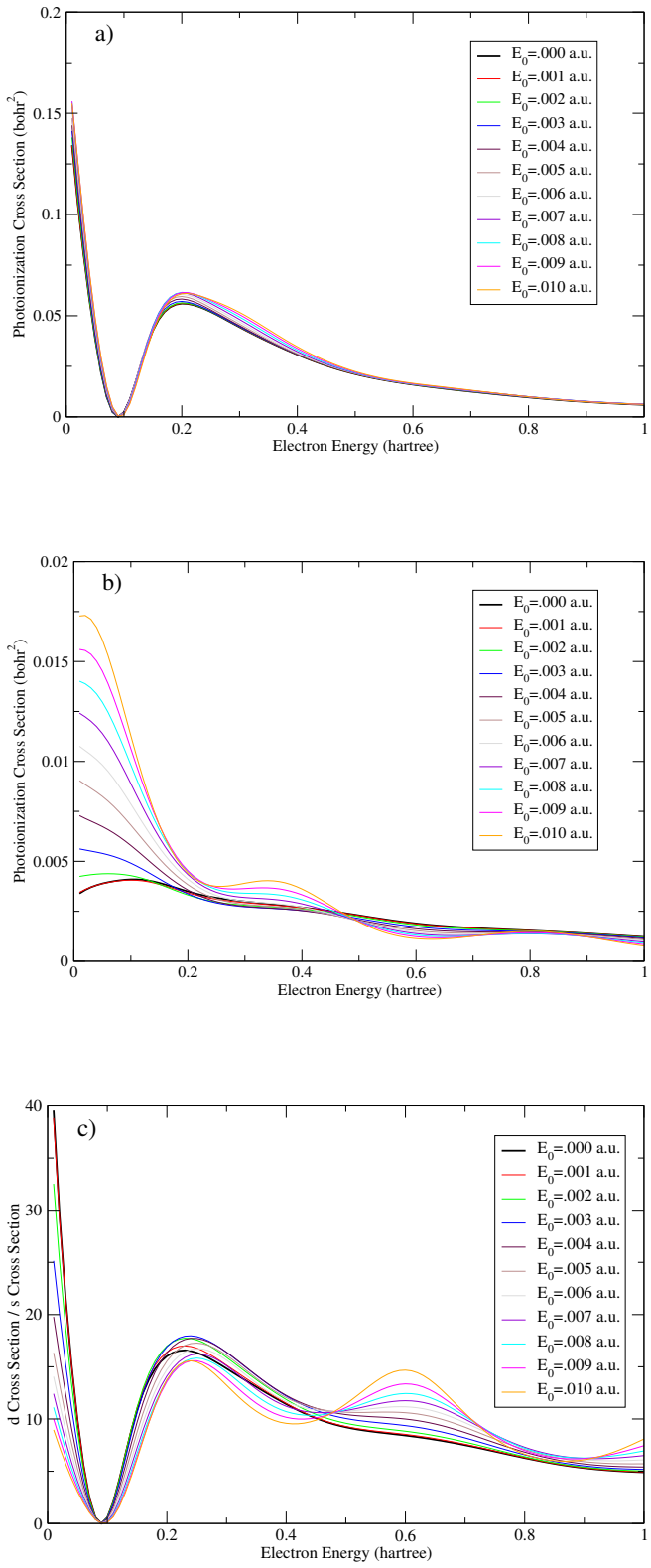

Figure 2.6: a) Cs^+ 5d single channel photoionization cross section vs energy at low electric field strengths. b)Cs^+ 6s single channel photoionization cross section vs energy at low electric field strengths. c) ratio of 5d to 6s photoionization cross sections vs energy at low electric field strengths.

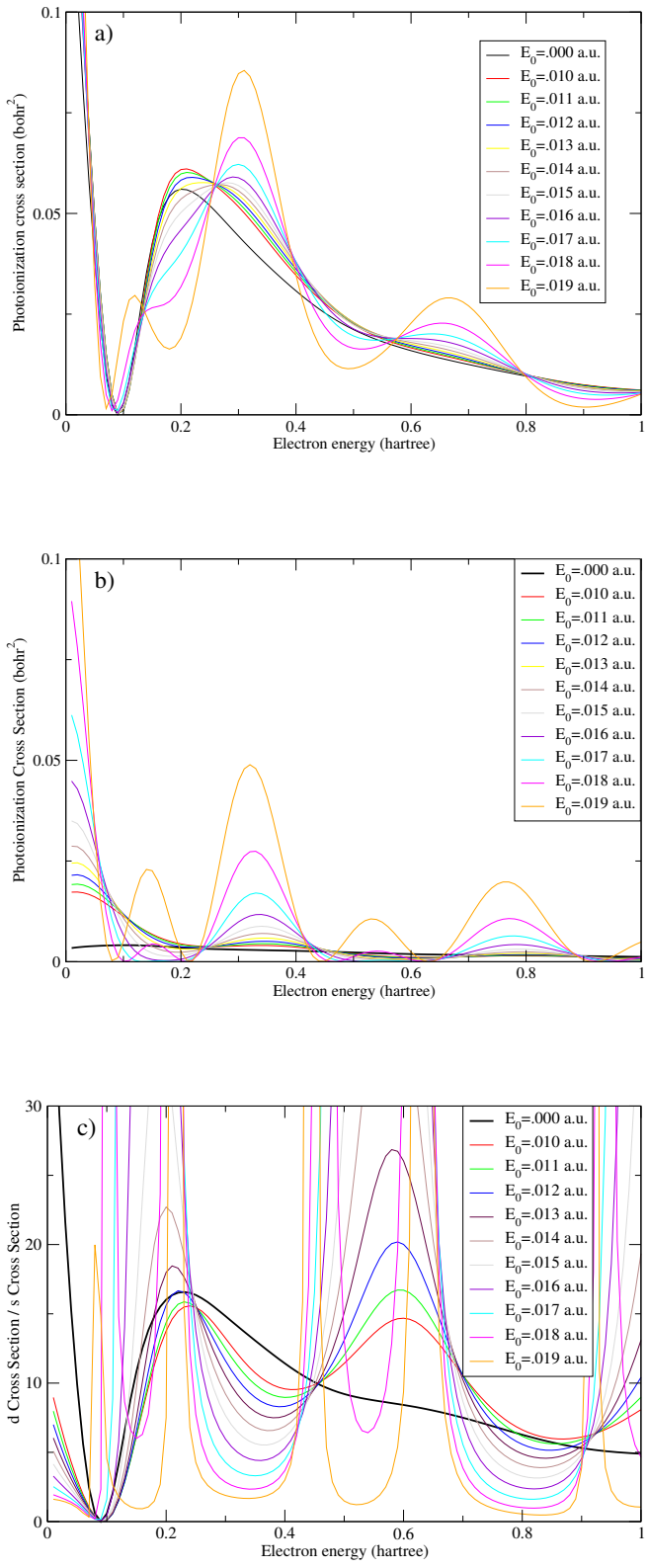

Figure 2.7: a) Cs^+ 5d single channel photoionization cross section vs energy at field strengths comparable to pulse peak b)Cs^+ 6s single channel photoionization cross section vs energy at field strengths comparable to pulse peak strengths. c) ratio of 5d to 6s photoionization cross sections vs energy at field strengths comparable to pulse peak.

roots of the interpolated intensities as a function of scattering energy. Because these ratios are calculated from harmonic peaks spaced by 2ω, they cannot resolve narrow features of the comparison spectra. As in the photoionization cross sections, there is a broad minimum at 0.1 H, followed by a maximum at 0.2H and associated with a π phase shift. At higher intensities, a second peak is seen at 0.5 H. This peak is harder to interpret. At low field strengths, the d/s ratio as calculated in the single channel photoionization develops a second peak at 0.6 H, slightly higher than the 0.5 H seen in the interpolated spectra. Such a disparity might arise due to nonadiabatic coupling, which is included in the time dependent calculation but not in the photoionization cross section. Alternatively, the high harmonic peaks in this energy region, which are beginning to approach the harmonic cutoff, may give a deceptive picture of the d/s ratio in this energy region.

Overall, the d/s comparison spectra show a much stronger resemblance to photoionization calculations made at lower field strengths (figure 2.6c), than at higher field strengths (figure 2.7c). This is consistent with the three step model, in which recollision happens when the field is near a zero. The comparison spectra do show an observable dependence on electric field strength, however. This could indicate that electric field does play an observable role in the recombination step of high harmonic generation. Such an effect could also result if the flux of the rescattering wavefunctions at particular energies had a different dependence on intensity for the s- as opposed to d- states.

2.1 Summary and Conclusions

This chapter has investigated the question of atomic shape resonances in an atom subjected to an intense laser field. The overarching questions to be answered are whether resonant features survive the introduction of the field, how these features are altered, and whether these features could be seen in an experiment.

Doubly adiabatic potential curves were found to give valuable insight for answer-

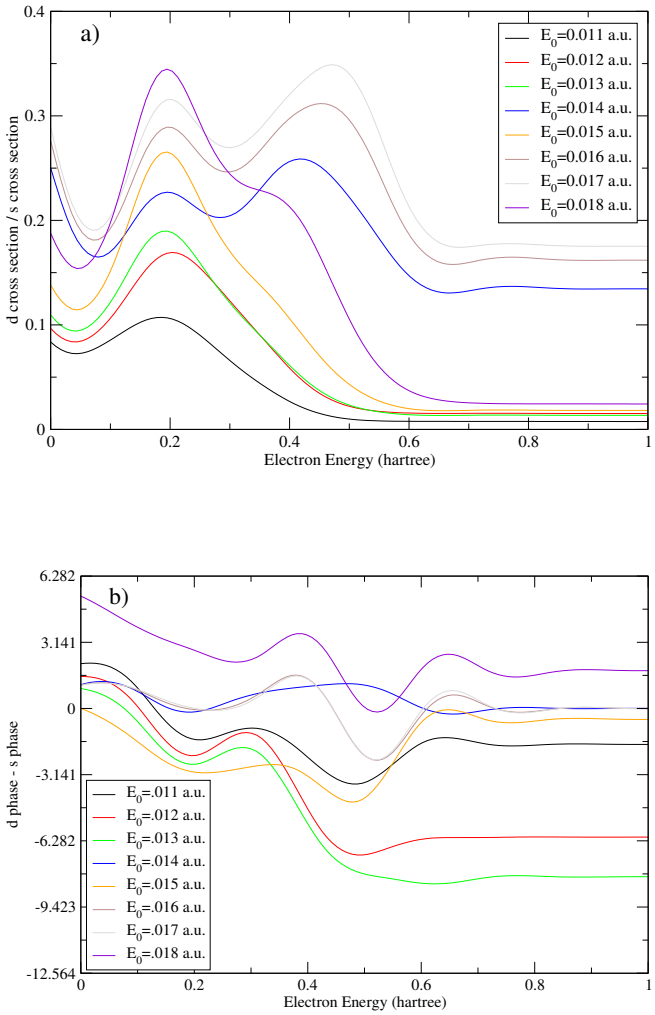

Figure 2.8: a) ratio of interpolated d harmonic spectrum to interpolated s harmonic cross section, normalized by ADK ionization rate b) difference in phase between d and s harmonic spectra.

ing these questions. Using these curves, it becomes easy to see whether features such as a potential barrier survive the presence of the field. In addition, although the full Hamiltonian includes nonadiabatic coupling between channels, single channel photoionization calculations were found to have a great deal of explanatory power for qualitative features of the high harmonic spectrum.

The high harmonic spectra were found to have information about the scattering wavefunction encoded in the harmonic peak heights, although this information is hidden by the complicated form of the scattering wavefunction. Much of this extraneous information can be removed by taking the ratio of the spectra for multiple electronic states of the same atom, since the rescattering wavefunction is largely independent of the initial orbital from which the electron tunnels. These comparison spectra were found to change with the applied field strength in a way which is qualitatively similar to the single-channel photoionization calculations, although the correspondence is not exact. The comparison spectra were most similar to the photoionization calculations when the electric field used in the photoionization calculations was considerably weaker than the peak field strength of the pulse, consistent with a recombination occurring near a minimum of the electric field. The shape resonance itself was found to be relatively insensitive to the field strength, although the potential barrier in Cs^+ is not particularly high. The peak of the resonance did not shift appreciably in photoionization calculations until $E_0 \approxeq 0.015$. In a high harmonic experiment, where recollision usually occurs near a minimum of the field, it is to be expected that shape resonance effects will still be visible at much higher peak field strengths.

Chapter 3

Molecular scattering and the Limits of the Plane Wave Approximation in the Measurement of Molecular Properties

As seen in the prior chapter, scattering phenomena such as shape resonances can have measurable effects on scattering observables such as the harmonic spectra measured in an experiment. This in turn has implications for the many current efforts to measure molecular properties by monitoring the scattering output channels in recollision experiments [32, 43, 41]. The best known such technique is molecular tomography [24], which uses high harmonic spectra from aligned molecules to reconstruct molecular wavefunctions.

Rescattering electrons offer clear advantages as probes of molecular structure. The intrinsic timescale of an ionization-acceleration-rescattering process is on the order of a single half-cycle of the driving laser field, typically a few fs. Because the liberated electron is accelerated by the driving laser field, simple formulas arising from classical physics are sufficient to map the energy of a rescattering event to the instants in a laser half-cycle when the electron is liberated and returns, allowing time resolution to be pushed to the the sub-fs level.

Because such techniques all rely on the same underlying physical process wherein a rescattering electron interacts with the parent ion, they are all inherently limited by the degree to which the rescattering process is understood. However, to date most efforts to measure molecular properties have treated the rescattering wavefunction as a free

electron plane wave, unperturbed by the electron interaction with the parent ion. Prior work relating to such reconstructions has dealt with bandwidth limitations arising from the HHG spectrum [39], orthogonality of the scattering- and bound-state wavefunctions [47, 42], and perturbative treatments of the ionic Coulomb potential [53]. This chapter investigates the departure from plane wave scattering which is caused by a nonzero molecular potential and the implications of that departure for molecular tomography. "Tomographic images" of bound states are calculated for a one dimensional square well, and for two molecules in three dimensions, N_2 and F_2. Much of the material presented in this chapter appeared first in [66].

3.1 Scattering States and Ramifications for Molecular Tomography

At its heart, the tomographic procedure attempts to measure the dipole matrix element

$$\vec{d_{\vec{k}}} = \int d^3\vec{x}\psi_{\vec{k}}(\vec{x})\vec{x}\psi_g(\vec{x}) \tag{3.1}$$

in momentum space between a continuum wavefunction $\psi_{\vec{k}}(\vec{x})$ which asymptotically goes as $e^{i\vec{k}\cdot\vec{x}}$ and a particular orbital $\psi_g(\vec{x})$ of some target molecule. In the limit where the molecular potential is zero, the plane wave approximation for the scattering states would be exact, and the wavefunction could be reconstructed according to

$$\vec{x}\psi_g(\vec{x}) = \int d^3\vec{k}e^{-i\vec{k}\cdot\vec{x}}\vec{d}_k \tag{3.2}$$

A nonzero molecular potential complicates this picture. In one dimension, the WKB approximation gives the continuum scattering state as

$$\psi_c \propto \frac{1}{\sqrt{k(x)}}e^{i\int^x k(x')dx'} \tag{3.3}$$

where $k(x) = \sqrt{2(E - V(x))}$. In the vicinity of the molecule, both the amplitude and the phase of the scattering state depart from the plane wave approximation.

An ideal tomographic experiment would measure $\vec{d}_{\vec{k}}$ between continuum states and an unperturbed molecular ion. In contrast, in rescattering experiments, recombination occurs in the presence of a strong and time-varying external laser field. The magnitude of the incoming wavefunction is affected by tunnel ionization from the highest occupied molecular orbital (HOMO) and the propagation of the electron between ionization and recombination. In addition, the high harmonic spectrum is sharply peaked at frequencies which are multiples of the driving laser frequency. For these reasons, it would be very appealing to measure $\vec{d}_{\vec{k}}$ using photoionization rather than high harmonic generation [47]. It is not clear how the phase of $\vec{d}_{\vec{k}}$ would be measured in such an experiment, but it is at least conceivable to do so by introducing some kind of beamsplitter with interfering pathways. However, since this chapter is concerned with the limitations to tomographic reconstruction under ideal circumstances, the photoionization amplitudes $\vec{d}_{\vec{k}}$ will be treated as though they could in principle be found. The issues discussed here with respect to tomographic reconstruction for a photoionization experiment apply also to HHG tomography, with the stipulation that the relevant scattering states should be calculated in the presence of an external laser field in order to provide an exact description.

Problems with the tomographic reconstruction procedure arise when the scattering states $\psi_{\vec{k}}(\vec{x})$ begin to deviate from the plane waves that were assumed in the initial theoretical formulations [24]. As can be seen in equation 3.3, this deviation becomes pronounced when the potential experienced by the electron is comparable to the scattering energy. In this case, the measured $\vec{d}_{\vec{k}}$ will depart from the Fourier transform of $\vec{x}\psi_g(\vec{x})$.

In equation 3.1, substitution of

$$\psi_{\vec{k}}(\vec{x}) = (2\pi)^{-3/2} \int d^3\vec{k} e^{i\vec{k'}\cdot\vec{x}} \tilde{\psi}_{\vec{k}}(\vec{k'}) \tag{3.4}$$

and evaluating the integral over $d^3\vec{x}$ yields

$$\vec{d}_{\vec{k}} = (2\pi)^{-3} \int d^3\vec{k'} \tilde{\psi}_{\vec{k}}(\vec{k'}) \widetilde{(\vec{x}\psi_g)}_{\vec{k'}} \tag{3.5}$$

where $\widetilde{(\vec{x}\psi_g)}(\vec{k'})$ represents the Fourier transform of $\vec{x}\psi_g(\vec{x})$, the quantity which tomographic procedures hope to measure, and $\tilde{\psi}_{\vec{k}}(\vec{k'})$ represents the Fourier transform of the scattering state $\psi_{\vec{k}}(x)$. In Equation 3.5, the scattering states define a Fourier-space mapping from the desired function $\widetilde{(\vec{x}\psi_g)}(\vec{k'})$ to the measured function $\vec{d}_{\vec{k}}$. In general, this mapping will not be diagonal, as the scattering states $\psi_{\vec{k}}(\vec{x})$ will have Fourier components at $\vec{k'} \neq \vec{k}$ due to distortions by the molecular potential. This mapping is not generally invertible without knowledge of the molecular scattering states.

A 1D square well provides a simple example whose study can document the extent to which the electronic potential energy affects the outcome of a tomographic reconstruction based on the plane wave approximation. A potential of the form

$$V(x) = \begin{cases} V & |x| \leq x_0 \\ 0 & |x| > x_0 \end{cases} \tag{3.6}$$

yields scattering states

$$\psi^{(\text{scat})}_{|k|}(x) = \begin{cases} Ae^{ikx} + Be^{-ikx} & x \leq -x_0 \\ Ce^{ik_2 x} + De^{-ik_2 x} & |x| \leq x_0 \\ Ee^{ikx} + Fe^{-ikx} & x > x_0 \end{cases} \tag{3.7}$$

where $k_2 = \sqrt{k^2 - 2V}$.

The two linearly independent solutions $\psi_{\pm|k|}(x)$ are now chosen such that their outgoing wave components go as $e^{\pm ikx}$ as $x \to \pm\infty$. For $\psi_{|k|}$, this corresponds to

$$A = \frac{4e^{2i(k+k_2)x_0} k k_2}{-(k-k_2)^2 + e^{4ik_2x_0}(k+k_2)^2}, \tag{3.8}$$

$$B = 0 \tag{3.9}$$

$$C = \frac{2e^{i(k+3k_2)x_0} k(k+k_2)}{-(k-k_2)^2 + e^{4ik_2x_0}(k+k_2)^2} \tag{3.10}$$

$$D = -\frac{2e^{i(k+k_2)x_0}k(k-k_2)}{-(k-k_2)^2 + e^{4ik_2x_0}(k+k_2)^2} \tag{3.11}$$

$$E = 1 \tag{3.12}$$

$$F = \frac{e^{2ikx_0}(e^{4ik_2x_0}-1)(k^2-k_2^2)}{-(k-k_2)^2 + e^{4ik_2x_0}(k+k_2)^2} \tag{3.13}$$

and for $\psi_{-|k|}$,

$$A = \frac{e^{2ikx_0}(e^{4ik_2x_0}-1)(k^2-k_2^2)}{-(k-k_2)^2 + e^{4ik_2x_0}(k+k_2)^2} \tag{3.14}$$

$$B = 1 \tag{3.15}$$

$$C = -\frac{2e^{i(k+k_2)x_0}k(k-k_2)}{-(k-k_2)^2 + e^{4ik_2x_0}(k+k_2)^2} \tag{3.16}$$

$$D = \frac{2e^{i(k+3k_2)x_0}k(k+k_2)}{-(k-k_2)^2 + e^{4ik_2x_0}(k+k_2)^2} \tag{3.17}$$

$$E = 0 \tag{3.18}$$

$$F = \frac{4e^{2i(k+k_2)x_0}kk_2}{-(k-k_2)^2 + e^{4ik_2x_0}(k+k_2)^2} \tag{3.19}$$

Note that although $k(x)$ takes on only two values in this problem, each scattering solution has nonzero Fourier components for $k' \neq k, k_2$.

The true dipole matrix elements may now be compared to the plane wave approximation. A two-node bound state wavefunction was chosen as a simple example which nonetheless possesses nontrivial spatial structure. Setting $x_0 = 2.5$ bohr, $V = -1.61$ hartree yields a two-node wavefunction with $E = -.5$ hartree. Figure 3.1a compares dipole matrix elements calculated between this bound state and continuum functions described by scattering eigenfunctions and plane waves. Whereas the plane wave dipole matrix elements are all purely imaginary, calculating the matrix elements using scattering states gives both real and imaginary components. If the d_k calculated using scattering states are now treated as "measured" dipoles and used to construct a tomographic image of the original bound state using equation 3.2, the resulting image will be complex valued. Figure 3.1b compares the original bound state with its tomographic image.

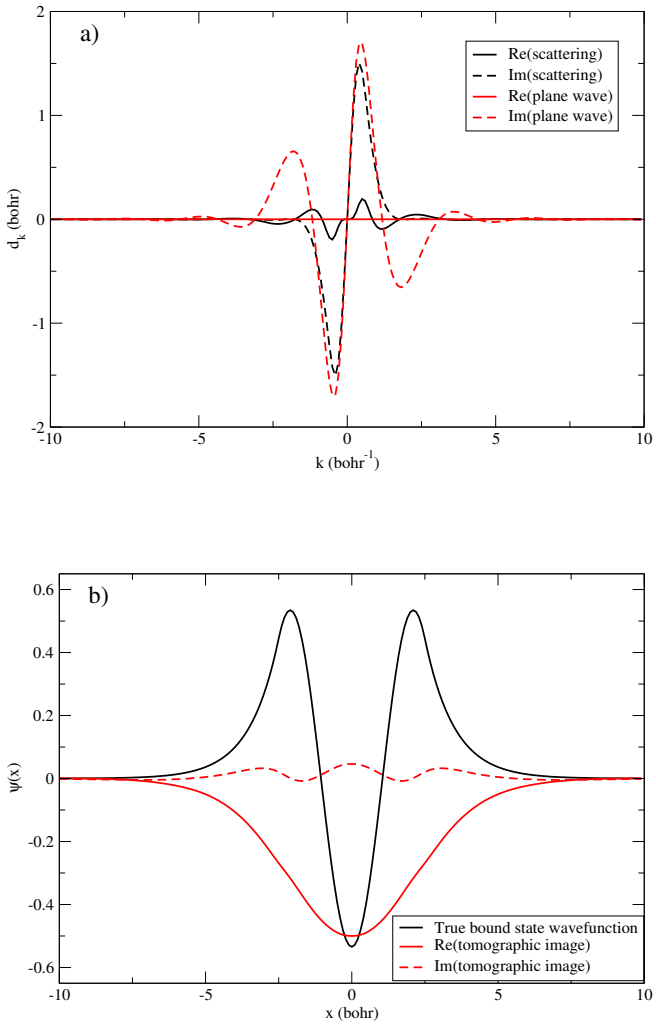

Figure 3.1: The tomographic reconstruction procedure applied to the 1D square well. (Top) Comparison of dipole matrix elements $d_k = \langle \psi_c(x) | \, x \, | \psi_g(x) \rangle$, calculated using plane waves and scattering states for $\psi_c(x)$. (Bottom) Because the scattering state matrix elements differ from those calculated using plane waves, the reconstructed image of the orbital will differ from the true bound state wavefunction.

The principles seen in the case of the 1D square well also limit tomographic reconstruction in true molecular systems, although molecular systems are much more computationally challenging due to the complicated potentials which describe the electron-ion interaction. We calculate the electron-ion scattering states using FERM3D [57], a code which is designed for the highly non-centrosymmetric potentials seen in these systems. This potential is described by $V_{mol} = V_s + V_{ex} + V_{pol}$, where V_s is the local electrostatic potential, V_{ex} is the exchange potential arising from antisymmetrization of the wavefunction and treated in the local density approximation, and V_{pol} is a polarization potential that describes the relaxation of the target under the influence of the incoming electron. Figure 3.2 compares the total photoionization cross section for N_2 calculated with FERM3D and the plane wave approximation to a prior calculation and experiment [6], while Figure 3.3 compares cross sections for F_2 to a previous calculation[27]. For both molecules, FERM3D gives cross sections with sizes comparable to prior calculations, with photoionization maxima shifted higher than in the comparison. In both molecules, the plane wave cross sections are too large by a factor of five.

The calculated dipole matrix elements may also be used to tomographically reconstruct the molecular orbitals. In a tomography experiment, the experimentally measurable quantity is the dipole matrix element between a bound state of the molecule and a scattering state whose incoming-wave portion asymptotically goes to $e^{i\vec{k}\cdot\vec{x}}$.

For incoming-wave boundary conditions, FERM3D calculates dipole matrix elements

$$d^q_{E;l,m} = \langle \psi^{(-)}_{E;l,m} |\, \hat{\epsilon}_q \cdot \vec{x}\, | \psi_g \rangle \tag{3.20}$$

where $\psi^{(-)}_{E;l,m}$ is an energy-normalized wavefunction which obeys incoming-wave boundary conditions [57]

$$\lim_{r\to\infty} \psi^{(-)}_{E;l,m} = \sum_{l',m'} Y_{lm}(\hat{r})(2i)^{-1}(f^+_l(r)\delta_{l,l'}\delta_{m,m'} - f^-_l(r)S^\dagger_{l,m;l',m'}). \tag{3.21}$$

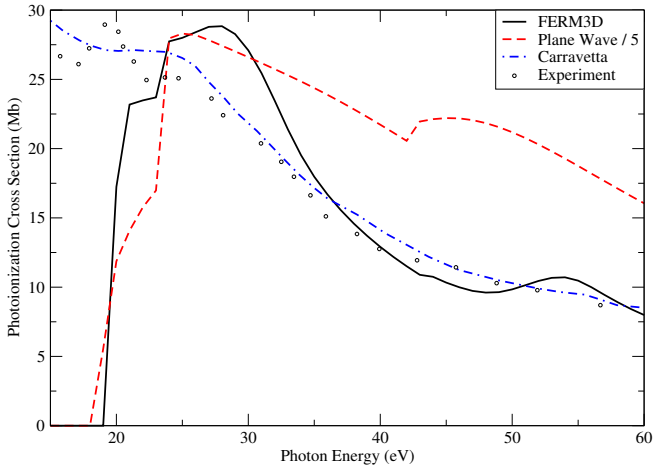

Figure 3.2: N_2 photoionization cross sections vs photon energy. Calculations made using FERM3D and the plane wave approximation are compared to experimental measurements taken from [6].

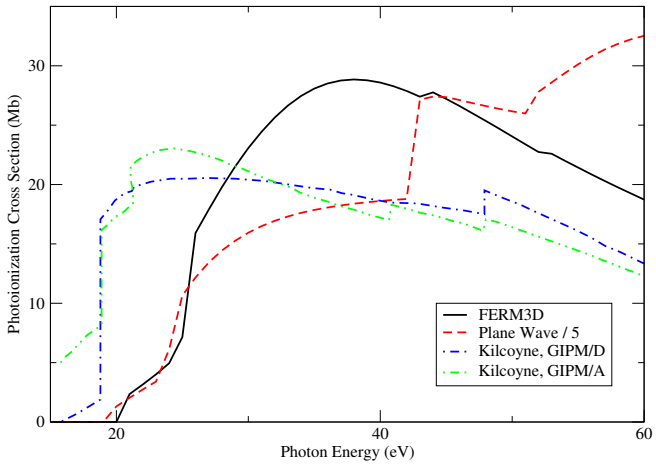

Figure 3.3: F_2 photoionization cross sections vs photon energy. Calculations made using FERM3D and the plane wave approximation are compared to theoretical calculations taken from [27].

where $f^{\pm}(r)$ has the asymptotic form

$$f^{\pm}(r) \rightarrow (\pi k)^{-1/2} r^{\pm i/k} e^{\pm ikr \pm i\eta}, \epsilon = k^2/2 \geq 0 \tag{3.22}$$

are radially outgoing/incoming Coulomb spherical waves, as defined in [4] and $\sigma_l = \arg[\Gamma(l+1-i/k)]$ is the Coulomb phase shift.

To find $d^q_{\vec{k}}$, it is now necessary to find the superposition $\psi_{\vec{k}} = A_{lm}(\vec{k})\psi_{E;lm}$ whose outgoing component matches the outgoing component of $e^{i\vec{k}\cdot\vec{x}}$. Expanding

$$e^{i\vec{k}\cdot\vec{x}} = 4\pi \sum_{l,m} i^l j_l(kr) Y_{l,m}(\hat{x}) Y^*_{lm}(\hat{k}) \tag{3.23}$$

where $j_l(kr) \rightarrow_{r\rightarrow\infty} (2i)^{-1}(e^{i(kr-l\pi/2)} - e^{-i(kr-l\pi/2)})$ are spherical Bessel functions, matching coefficients of $Y_{lm}(r)e^{ikr}$ yields

$$A_{lm}(\vec{k}) = 4\pi i^l e^{-i\sigma_l} Y^*_{lm}(\hat{k}) k^{1/2} \tag{3.24}$$

where the factor of $k^{1/2}$ converts the energy-normalized matrix elements calculated in FERM3D to momentum normalization.

$\vec{d_{\vec{k}}}$ is now given by

$$\vec{d^q_{\vec{k}}} = \sum_{l,m} \vec{d^q_{l,m}}(k^2/2) A_{l,m}(\vec{k}) \tag{3.25}$$

As in the 1D square well, the tomographic image of the orbital may now be computed by substituting the calculated $\vec{d_{\vec{k}}}$ for the experimentally measured quantity in the tomographic reconstruction procedure. As photoionization is not limited to the molecular HOMO, tomographic images may be calculated for all the orbitals of a molecule. Such tomographic images will in general be complex-valued, and will differ according to which polarization component is used for the tomographic procedure.

We present tomographic images of various orbitals of N_2 and F_2, calculated in the body-fixed frame using the x,y, and z polarization components. Each image is given with the real and imaginary components, and includes an orange bar (not always visible) extending between the two atoms of the molecule for the purposes of scale. For N_2,

tomographic reconstructions for the $1\pi_u$ (Fig. 3.4), $3\sigma_g$ (Fig. 3.5), $2\sigma_u$ (Fig. 3.6) and $2\sigma_g$ (Fig. 3.7) orbitals are shown. For F_2, reconstructions were calculated for the $1\pi_g$ (Fig. 3.8), $3\sigma_g$ (Fig. 3.9), $1\pi_u$ (Fig. 3.10), $2\sigma_u$ (Fig. 3.11), and $2\sigma_g$ (Fig. 3.12) orbitals.

For these example molecules, tomographic reconstruction tends to preserve the σ or π, gerade or ungerade character of the orbitals in question. However, the reconstructed orbitals may display additional radial nodes not found in the original orbitals. Features which correspond to features of the original orbitals may be distorted in shape and size, and display a spatially varying complex phase. Finally, tomographic images of the same orbital made using different polarization information may produce differing images of the same orbital. Many of these features are also seen in [42], which treats the scattering process from a multielectron perspective, but does not consider the distorting effects of a molecular potential.

3.2 Conclusions

The use of rescattering electrons as a probe of molecular properties offers many exciting avenues for future research. However, the rescattering process is itself more complicated than has been recognized in early reconstruction efforts, and is worthy of study in its own right.

For molecular tomography, the results presented in this paper suggest that at energy scales where such distortion is significant, tomographic reconstructions may be significantly distorted from the "true" orbitals these methods seek to find. Nevertheless, for the example molecules presented here, the tomographic reconstruction procedure was able to successfully reproduce the σ or π, gerade or ungerade nature of the orbitals in question. Reconstructions made using differently polarized dipole matrix elements gave different tomographic images of the same orbital, while reconstructions made from a particular polarization gave tomographic images with spatially varying complex phase. Both of these properties could be useful as an experimental check of reconstructed

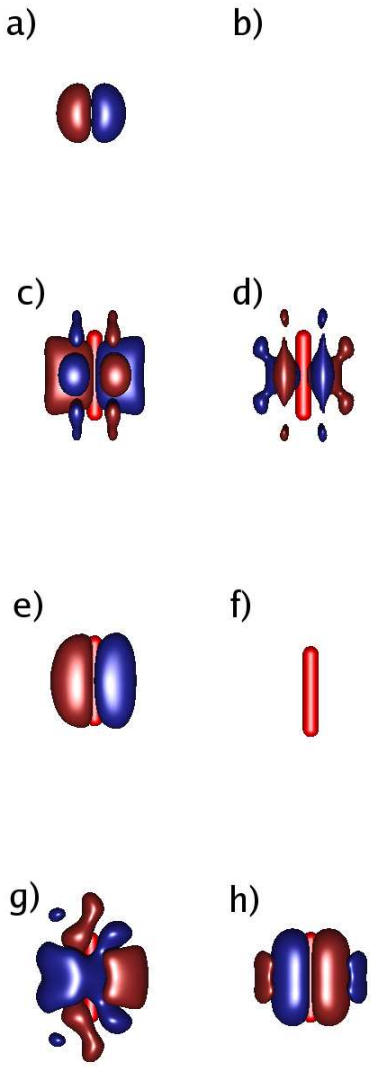

Figure 3.4: Comparison of the Hartree-Fock orbital and associated tomographic images for the N_2 $1\pi_u$ orbital. a) and b) give the real and (zero) imaginary components of the Hartree-Fock orbital. c) and d) give the real and imaginary components of the tomographic image made from the x-polarized dipole matrix element. e) and f) give the real and imaginary components of the tomographic image made from the y-polarized dipole matrix element. g) and h) give the real and imaginary components of the tomographic image made from the z-polarized dipole matrix element.

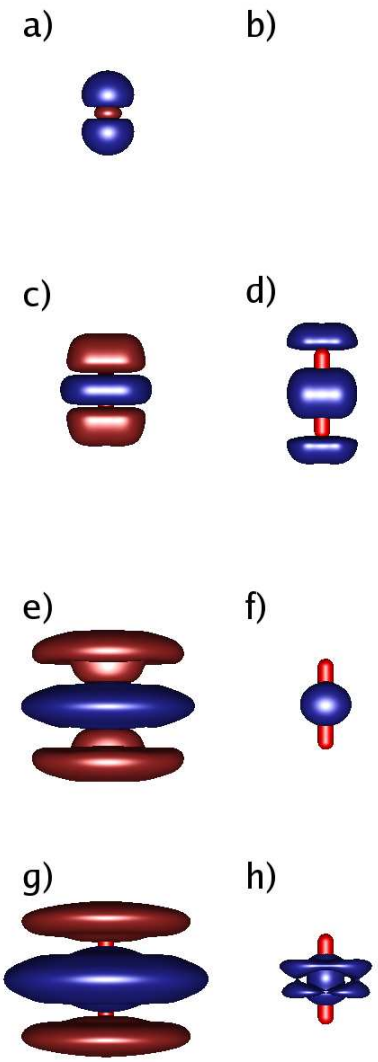

Figure 3.5: Comparison of the Hartree-Fock orbital and associated tomographic images for the N_2 $3\sigma_g$ orbital. a) and b) give the real and (zero) imaginary components of the Hartree-Fock orbital. c) and d) give the real and imaginary components of the tomographic image made from the x-polarized dipole matrix element. e) and f) give the real and imaginary components of the tomographic image made from the y-polarized dipole matrix element. g) and h) give the real and imaginary components of the tomographic image made from the z-polarized dipole matrix element.

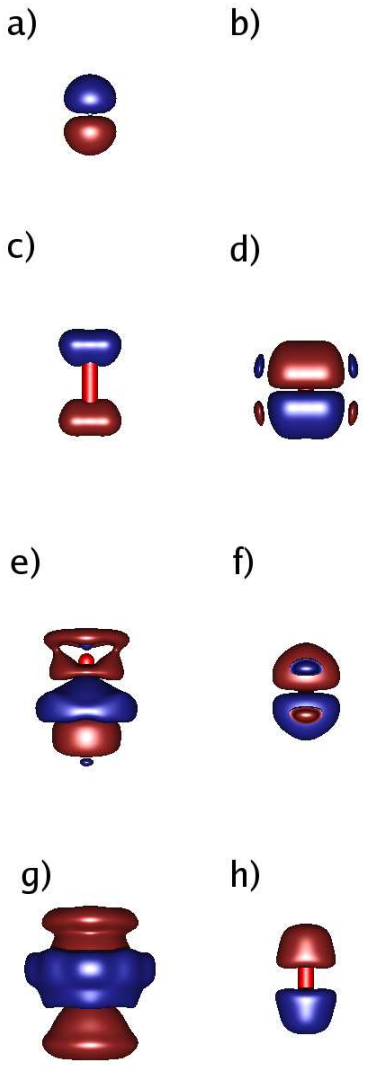

Figure 3.6: Comparison of the Hartree-Fock orbital and associated tomographic images for the N_2 $2\sigma_u$ orbital. a) and b) give the real and (zero) imaginary components of the Hartree-Fock orbital. c) and d) give the real and imaginary components of the tomographic image made from the x-polarized dipole matrix element. e) and f) give the real and imaginary components of the tomographic image made from the y-polarized dipole matrix element. g) and h) give the real and imaginary components of the tomographic image made from the z-polarized dipole matrix element.

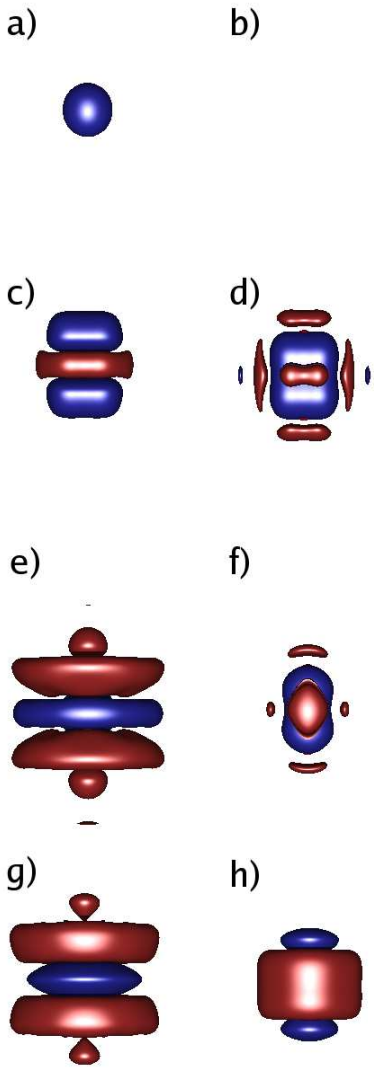

Figure 3.7: Comparison of the Hartree-Fock orbital and associated tomographic images for the N_2 $2\sigma_g$ orbital. a) and b) give the real and (zero) imaginary components of the Hartree-Fock orbital. c) and d) give the real and imaginary components of the tomographic image made from the x-polarized dipole matrix element. e) and f) give the real and imaginary components of the tomographic image made from the y-polarized dipole matrix element. g) and h) give the real and imaginary components of the tomographic image made from the z-polarized dipole matrix element.

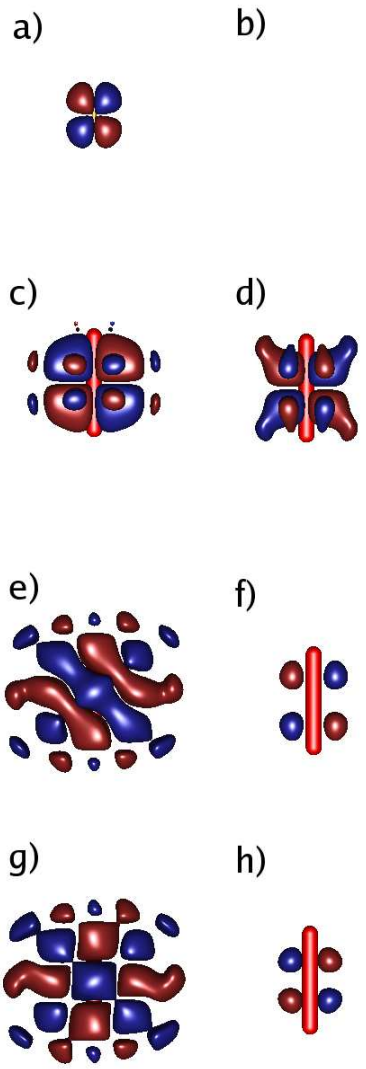

Figure 3.8: Comparison of the Hartree-Fock orbital and associated tomographic images for the F_2 $1\pi_g$ orbital. a) and b) give the real and (zero) imaginary components of the Hartree-Fock orbital. c) and d) give the real and imaginary components of the tomographic image made from the x-polarized dipole matrix element. e) and f) give the real and imaginary components of the tomographic image made from the y-polarized dipole matrix element. g) and h) give the real and imaginary components of the tomographic image made from the z-polarized dipole matrix element.

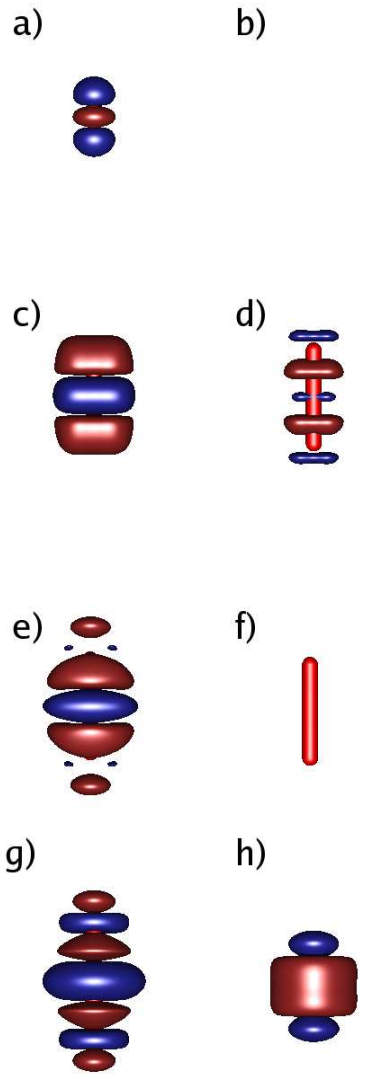

Figure 3.9: Comparison of the Hartree-Fock orbital and associated tomographic images for the F_2 $3\sigma_g$ orbital. a) and b) give the real and (zero) imaginary components of the Hartree-Fock orbital. c) and d) give the real and imaginary components of the tomographic image made from the x-polarized dipole matrix element. e) and f) give the real and imaginary components of the tomographic image made from the y-polarized dipole matrix element. g) and h) give the real and imaginary components of the tomographic image made from the z-polarized dipole matrix element.

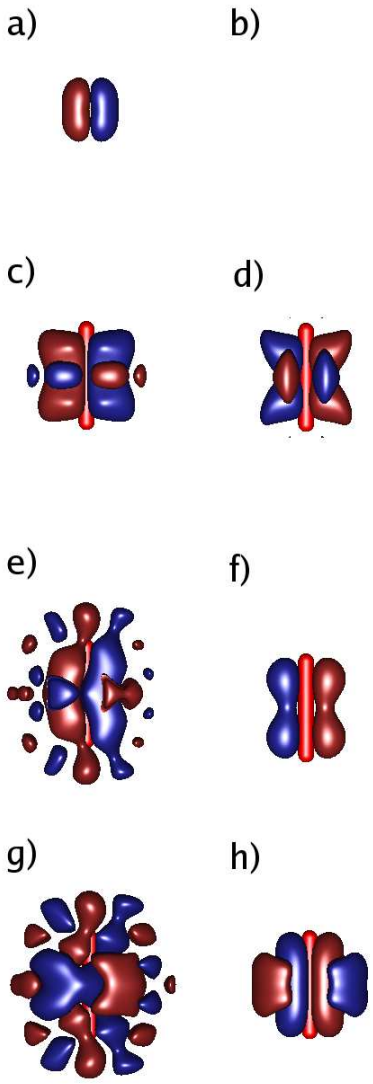

Figure 3.10: Comparison of the Hartree-Fock orbital and associated tomographic images for the F_2 $1\pi_u$ orbital. a) and b) give the real and (zero) imaginary components of the Hartree-Fock orbital. c) and d) give the real and imaginary components of the tomographic image made from the x-polarized dipole matrix element. e) and f) give the real and imaginary components of the tomographic image made from the y-polarized dipole matrix element. g) and h) give the real and imaginary components of the tomographic image made from the z-polarized dipole matrix element.

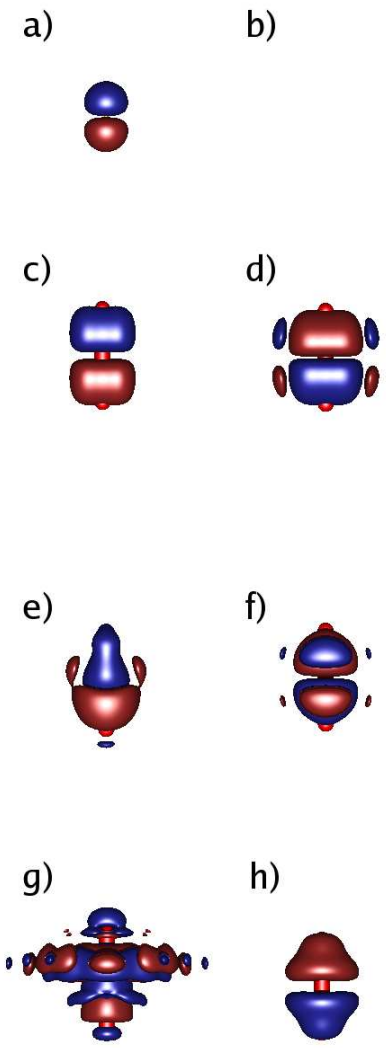

Figure 3.11: Comparison of the Hartree-Fock orbital and associated tomographic images for the F_2 $2\sigma_u$ orbital. a) and b) give the real and (zero) imaginary components of the Hartree-Fock orbital. c) and d) give the real and imaginary components of the tomographic image made from the x-polarized dipole matrix element. e) and f) give the real and imaginary components of the tomographic image made from the y-polarized dipole matrix element. g) and h) give the real and imaginary components of the tomographic image made from the z-polarized dipole matrix element.

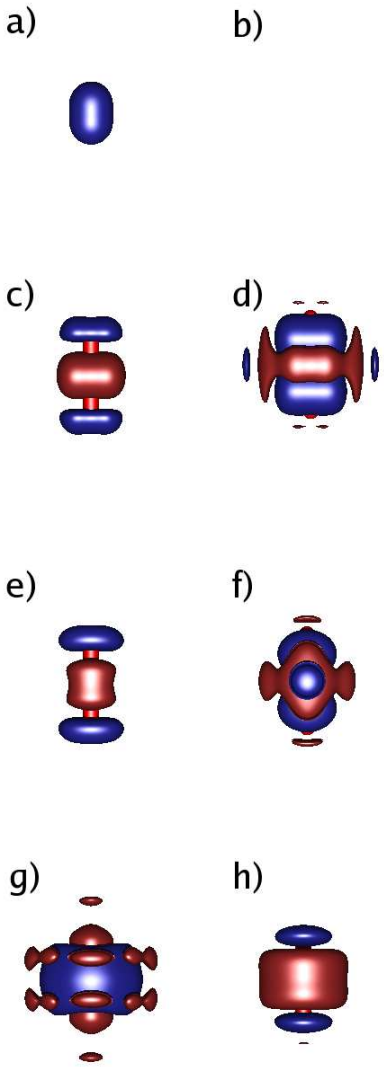

Figure 3.12: Comparison of the Hartree-Fock orbital and associated tomographic images for the F_2 $2\sigma_g$ orbital. a) and b) give the real and (zero) imaginary components of the Hartree-Fock orbital. c) and d) give the real and imaginary components of the tomographic image made from the x-polarized dipole matrix element. e) and f) give the real and imaginary components of the tomographic image made from the y-polarized dipole matrix element. g) and h) give the real and imaginary components of the tomographic image made from the z-polarized dipole matrix element.

wavefunctions: ideal reconstructions would have a spatially uniform complex phase and reconstructions made with different polarization information should agree with one another. Additionally, experiments could use higher scattering energies to minimize the scattering state distortions due to interactions with the molecular potential.

The sensitivity of the scattering states to the molecular potential also offers the prospect for new types of experiments. Such experiments could monitor the movement of charge within the parent ion at ultrafast timescales. For example, a two-center interference experiment of the type discussed in [32] might observe the movement of charge in a diatomic molecule by observing interference maxima/minima occurring at different energies for the short and long rescattering trajectories.

3.3 Appendix: Gauges and Dispersion Relations

Within the overall framework of the plane wave approximation, several heuristic methods have been suggested to improve the accuracy of tomographic reconstructions [32]. For the 1D square well, we considered the effects of phenomenological "dispersion relations" and reconstructions made in the momentum, rather than velocity gauge.

A dispersion relation attempts to correct for an electron's shorter wavelength by substituting $e^{i\vec{q}\cdot\vec{x}}$ for $e^{i\vec{k}\cdot\vec{x}}$ in Equation 3.2, where $|\vec{q}| = \sqrt{2(k^2/2 - \epsilon V)}$, where V is the potential felt by the electron in the interaction region, and $\epsilon \in [0, 1]$.

Tomography may also be performed in gauges other than the length gauge given in equation 3.2. If both continuum and bound wavefunctions are eigenstates of the Hamiltonian, the dipole matrix element is identical in the length

$$d_k^{(l)} = \langle \psi_g | \, x \, | \psi_k \rangle \tag{3.26}$$

and velocity

$$d_k^{(p)} = \frac{\langle \psi_g | \, ip \, | \psi_k \rangle}{E_g - E_k} \tag{3.27}$$

gauges. From the momentum gauge form of the dipole matrix element, and employing

the plane wave approximation for $|\psi_k\rangle$, it is possible to generate a second tomographic reconstruction

$$\psi^{(p)}(x) = \int dq e^{iq(k)x} d_k^{(p)} \frac{E_g - k^2/2}{-q(k)}. \tag{3.28}$$

As a plane wave is not an eigenfunction of the scattering Hamiltonian, this reconstruction will in general give a different image of the target orbital than a reconstruction made using the length gauge.

We tested both the length- and momentum-gauge tomographic reconstructions using dispersion relations $q(\epsilon) = \sqrt{2(k^2/2 - \epsilon V)}$, using the overlap of the true wavefunction and its (normalized) tomographic image as a figure of merit. The test employed the same $V = -1.61$, $x_0 = 2.5$ potential and $E = -.5$ target wavefunction used to generate Figure 3.1.

Figure 3.13a gives the magnitude of the overlap between the two tomographic images and the ground state and between each other as a function of the dispersion parameter ϵ. For this choice of potential and target orbital, the tomographic reconstructions gave a very poor overlap with the target orbital for $\epsilon \in [0, 1]$, reaching a maximum magnitude of 0.60 at $\epsilon = 0.26$ in the momentum gauge. In the dipole gauge, the maximum overlap was achieved at $\epsilon = 1.0$, also giving an overlap of magnitude 0.60. Figure 3.13b compares the maximally overlapping reconstructions to the true ground state wavefunction.

A perfect reconstruction would give the same image regardless of the gauge the tomographic procedure was performed in. However, agreement between images made in separate gauges does not guarantee the accuracy of the reconstruction. Although both gauges gave nearly identical tomographic images at $\epsilon = 0$, the resulting images gave among the worst overlaps with the target orbital.

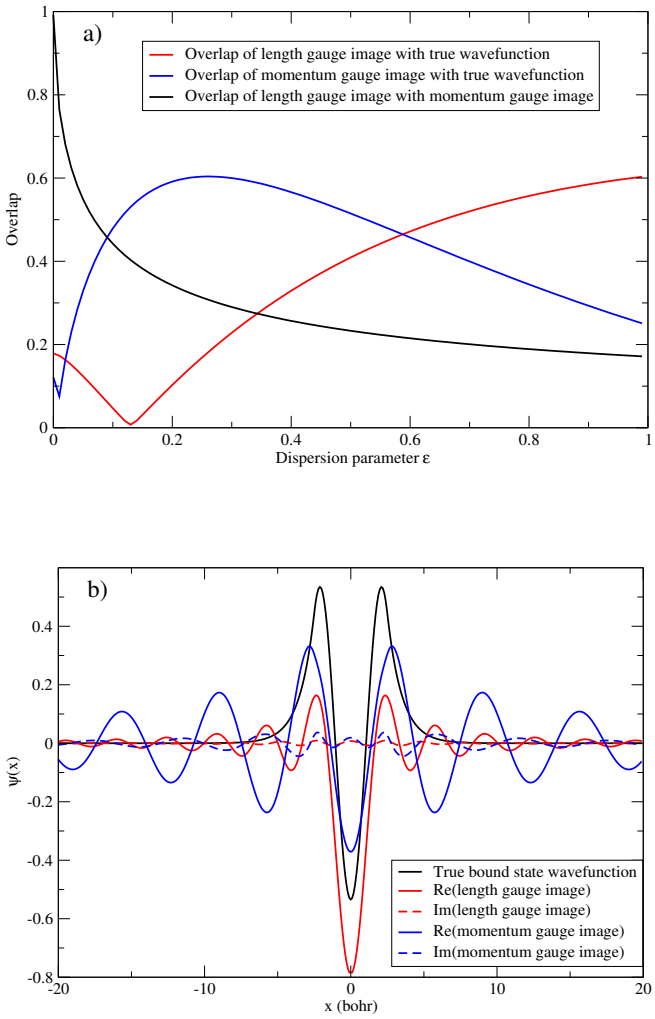

Figure 3.13: a) Magnitude of the overlap between (normalized) tomographic images of a bound wavefunction and the true wavefunction, and between different tomographic images, calculated using $q(\epsilon) = \sqrt{2(k^2/2 - \epsilon V)}$, $\epsilon \in [0, 1]$. b) Comparison of the maximally overlapping tomographic images to the true wavefunction. In the momentum gauge, maximal overlap was obtained for $\epsilon = .26$, while in the length gauge, maximal overlap was obtained for $\epsilon = 1$. Both images have been normalized and rotated to give a purely real overlap with the true wavefunction.

Chapter 4

High Harmonic Generation in SF_6: Raman-excited Vibrational Quantum Beats

4.1 Introduction

In the prior chapters, and indeed in most treatments of high harmonic generation, HHG is treated as a purely electronic process. A single active electron tunnels free of a parent molecule and eventually scatters from it, but the molecule itself is treated in essentially the same way as a lone atom, as no more than a complicated potential influencing the active electron. In reality, molecules differ from atoms in an essential way because they possess non electronic internal degrees of freedom, which can themselves be affected by the high harmonic process.

The possibility that such internal degrees of freedom could play a detectable role in HHG is intriguing, because the intrinsic timescale in HHG – the time necessary to ionize, propagate and rescatter – is only half a laser cycle. This is faster than many chemically interesting processes, holding out the possibility that HHG could serve as a probe of molecular motion. Alternatively, tailoring the state of a molecule prior to HHG could serve to give additional control over the generated light.

These issues were brought to the fore by an experiment at JILA [63]. In the experiment, a high harmonic generating laser pulse was preceded by a weaker pulse whose effect was to stimulate Raman-active vibrations in SF_6 molecules. Varying the delay between the two pulses had the effect of modulating the intensity of the HHG light

generated by the second pulse. Moreover, the modulation occurred at frequencies equal to those of the Raman-active normal modes stimulated by the first pulse. Although SF_6 has 3 non-Raman-active vibrational modes, none of their frequencies were detected in the modulated signal.

This chapter presents a fully quantum mechanical model of high harmonic generation in molecules. This model provides a framework to interpret the observed modulation of high harmonic intensities observed in the JILA experiment, and is easily extended to systems with more complicated dynamics. Secondly, it presents a version of the three step model which has been improved for the purpose of treating HHG in molecules with relevant internal degrees of freedom. Finally, the modulations predicted by this improved model are compared with the modulations observed in the JILA experiment. This chapter recapitulates and extends work which originally appeared in [65].

4.2 The Vibrational Wavefunction of the Molecule

An important difference between atomic and molecular systems is that molecules have nontrivial structure in the form of vibrational degrees of freedom. For an M atom molecule, this corresponds to $N = 3M - 6$ ($N = 3M - 5$ for linear molecules) internal degrees of freedom, which can be expressed in normal mode coordinates. The vibrational wavefunction of the molecule can then be expanded as the product of simple harmonic oscillator basis functions in each of the normal modes of the molecule:

$$|\psi_{\text{vib}}\rangle = \sum_{n_1,n_2,\ldots n_N=0}^{\infty} A_{n_1,n_2,\ldots,n_N} |n_1, n_2, \ldots n_N\rangle \tag{4.1}$$

where

$$\mathbf{a^{(i)\dagger} a^{(i)}} |\mathbf{n_1} \ldots \mathbf{n_N}\rangle = \mathbf{n_i} |\mathbf{n_1} \ldots \mathbf{n_N}\rangle \tag{4.2}$$

where $|n_1 n_2 \ldots n_N\rangle$ is the outer product of simple harmonic oscillator state $|n_1\rangle$ in the first normal mode, $|n_2\rangle$ in the second normal mode, and so on.

For the purposes of this chapter, all operators will be expanded to first order in raising $\mathbf{a}^{\dagger(\mathbf{i})}$ and lowering $\mathbf{a}^{(\mathbf{i})}$ operators in each normal mode i. At this level of approximation, the evolution of the vibrational wavefunction becomes separable, and the overall coefficient $A_{n_1 n_2 \ldots n_N}(t)$ can be factored into the product of individual coefficients $a_{n_i}(t)$ and an overall function of time $f(t)$

$$A_{n_1 n_2 \ldots n_N}(t) = a_{n_1}(t) a_{n_2}(t) \ldots a_{n_N}(t) f(t). \tag{4.3}$$

(Note that the coefficients $a_{n_i}(t)$ should not be confused with lowering operators $\mathbf{a}^{(\mathbf{i})}$.)

In the interests of simplicity and clarity, the remainder of this chapter will use a 1-D picture, describing the evolution of the vibrational wavefunction for a single normal mode. The concepts from the 1-D model extend readily to the nonseparated problem in the event that operators involving two or more raising or lowering operators become important. [1]

4.3 Vibrational Interference

Although high harmonic generation is primarily an electronic process, the vibrational state of the molecule can affect the harmonic intensity. This occurs because at several points in the high harmonic process, the vibrational wavefunction has amplitudes either to stay unchanged or to "hop" up or down from simple harmonic oscillator state $|n\rangle$ to states $|n \pm 1\rangle$, much in the same way that a photon in a beamsplitter has amplitudes to take two or more paths. As in a beamsplitter experiment, two or more indistinguishable pathways interfere with one another and modulate the output signal detectably. The multiple pathways at play in the high harmonic process are diagrammed in Figure 4.1.

Raman Excitation The first opportunity to change vibrational states occurs when the vibrationally cold molecules are subject to the weak, off-resonant initial pulse.

[1] The lack of modulation at combination frequencies like $2\omega_1$, $\omega_1 + \omega_2$,$\omega_1 - \omega_2$, etc. suggests but does not prove that such higher-order terms are not important in discussing the JILA experiment.

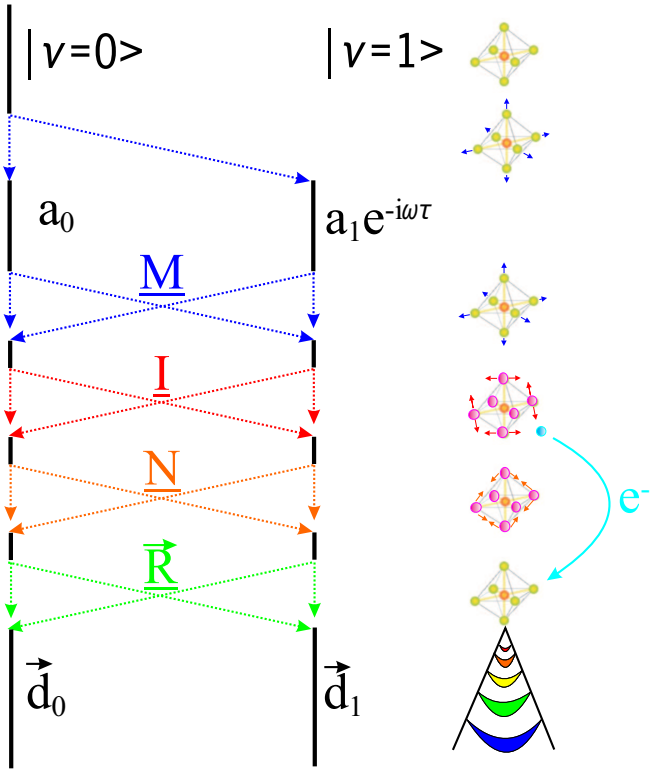

Figure 4.1: The vibrational interference model [65] in one dimension. The molecule ends the first (Raman) pulse in a superposition of the $\nu = 0$ and $\nu = 1$ vibrational states. After a time delay, the two vibrational states are mixed by stimulated Raman scattering (transfer matrix $\underline{\mathrm{M}}$), "hopping" during ionization ($\underline{\mathrm{I}}$) and recombination ($\underline{\mathrm{R}}$), as well as evolution of the ionic wavefunction while the electron is away ($\underline{\mathrm{N}}$). Interference between adjacent vibrational states modulates the high harmonic signal.

This causes the molecule to undergo stimulated Raman scattering. Beginning the first pulse in the $|0\rangle$ vibrational state, it is driven into a coherent superposition of the zeroth and first vibrational state

$$|\psi_{\text{vib}}\rangle = a_0(0)\,|0\rangle + a_1(0)\,|1\rangle \tag{4.4}$$

by the end of the pulse. (For the pulse length and intensity used in the JILA experiment, calculations show no appreciable population of the $|2\rangle$ or higher states after the Raman pulse. Accordingly, the $|2\rangle$ and higher states have been dropped from this analysis.) Because only one normal mode is used in this analysis, the N quantum number has been dropped, so that $a_0 = a_{1_0}(0)$ and $a_1 = a_{1_1}(0)$. $t = 0$ is chosen at some time after the end of the first pulse, when the stimulated Raman scattering is over.

The vibrational state coefficients follow equations of motion given by

$$\begin{aligned} i\dot{a}_{n_i}(t) = \omega_i \left(n_i + \frac{1}{2}\right) a_{n_i}(t) - \frac{1}{2}\sum_{A,B} E_A(t)E_B(t)\times \\ \left[\alpha_{AB}a_{n_i} + \partial_i\alpha_{AB}(\sqrt{n_i+1}\,a_{n_i+1} + \sqrt{n_i}\,a_{n_i-1})\right]. \end{aligned} \tag{4.5}$$

Here ω_i is the normal mode frequency, indices A and B run over $\{x, y, z\}$, $E_A(t)$ is the component of the electric field in the (body-frame) A direction at time t, Q_i is the normalized displacement associated with normal mode i and $\alpha_{AB}(Q_1, Q_2, ...)$ is the polarizability tensor of the molecule. These equations of motion have off-diagonal elements only if $\partial_i\alpha_{AB} \equiv (2m\omega_i)^{-1/2}\,\partial\alpha_{AB}/\partial Q_i|_{Q_i=0} \neq 0$, which is the condition for a mode to be Raman active. The polarizability tensor and its derivatives are found by performing an unrestricted Hartree-Fock calculation [16] using the aug-cc-pVTZ basis set. [11]

Between the two pulses, the $|0\rangle$ and $|1\rangle$ states evolve as eigenstates of the simple harmonic oscillator Hamiltonian. The states are then mixed once again by stimulated Raman scattering during the high harmonic generating pulse. These effects are approximated by a unitary 2×2 transfer matrix $\underline{M}$, where M_{ij} is the amplitude to be in state $|i\rangle$ at the instant of ionization after beginning the second pulse in state $|j\rangle$.

Ionization and Recombination The molecule's vibrational wavefunction evolves further during each of the three steps –ionization, propagation, and recombination– of the three step model. The molecule's vibrational state hops up or down a level during ionization, evolves while the propagating electron is away from the molecule, and hops once again when the electron recombines with the parent ion.

These hopping amplitudes arise because ionization and recombination, commonly thought of as purely electronic processes, are both strongly modulated by molecular distortions. This is the simplest way in which the internal degrees of freedom in molecules allows for behavior that has no analogue in atomic systems. Nonzero derivatives of ionization and recombination amplitudes translate directly into amplitudes for the molecule to change its vibrational state during these processes. Taylor-expanding the ionization operator about the equilibrium configuration of the neutral molecule,

$$\hat{I} = \hat{I}|_{\text{eq}} + \frac{\partial \hat{I}}{\partial Q} Q + \mathbb{O}(Q^2), \tag{4.6}$$

using the identity $Q = (\mathbf{a} + \mathbf{a}^\dagger)/\sqrt{\mathbf{2m}\omega}$ and substituting $I_0 = \hat{i}|_{\text{eq}}$, $I_1 = (2m\omega)^{-1/2} \frac{\partial \hat{I}}{\partial Q}$, the ionization operator can be rewritten

$$\hat{I} = I_0 + I_1(\mathbf{a} + \mathbf{a}^\dagger). \tag{4.7}$$

Identical logic gives the recombination dipole vector operator

$$\hat{\vec{R}} = \vec{R}_0 + \vec{R}_1(\mathbf{a} + \mathbf{a}^\dagger) \tag{4.8}$$

Vibrational Dynamics of the Parent Ion Between the times of ionization and recombination, the evolution of the internal state of SF_6^+ is quite complicated. This is because SF_6 has three degenerate orbitals at the point of maximum symmetry. Thus, at any nuclear configuration **near** this maximum symmetry point, these three SF_6^+ orbitals are very nearly degenerate, and are mixed with one another strongly by molecular distortions. Orbital degeneracies can be broken and orbital energies can cross even with relatively small distortions. Because of this, it is necessary to treat

this interplay between electronic and vibrational states when describing the dynamics of SF_6^+ in the vicinity of the maximum symmetry point.

In its maximum symmetry configuration, SF_6^+ belongs to the O_h point group, with three degenerate T_{1g} orbitals which transform like axial vectors $\hat{x}$, $\hat{y}$ and $\hat{z}$. When the molecule is distorted away from the maximum symmetry point via either an E_g or a T_{2g} distortion, the triple degeneracy breaks up into three nondegenerate electronic orbitals. The fully symmetric A_{1g} or "breathing" mode preserves the triple degeneracy.

The full vibronic (vibrational-electronic) Jahn-Teller coupling matrix for a triply degenerate system is given by[15, 38, 5]

$$H_T = \begin{pmatrix} g_1 - g_\theta + \sqrt{3}g_\epsilon & g_\zeta & g_\eta \\ g_\zeta & g_1 - g_\theta - \sqrt{3}g_\epsilon & g_\xi \\ g_\eta & g_\xi & g_1 + 2g_\theta \end{pmatrix} \tag{4.9}$$

This matrix represents the coupling between the states with $\hat{x}$, $\hat{y}$, and $\hat{z}$ symmetry, caused by vibrational operators, so that g_ζ represents the off-diagonal coupling between the states with $\hat{x}$ and $\hat{y}$ symmetry, g_η the off-diagonal coupling between the states with $\hat{x}$ and $\hat{z}$ symmetry, and g_ξ represents the off-diagonal coupling between the states with $\hat{y}$ and $\hat{z}$ symmetry.

Defining the E_g normal mode coordinates Q_θ and Q_ϵ, which transform like $2z^2 - x^2 - y^2$ and $x^2 - y^2$ respectively, and the T_{2g} normal mode coordinates Q_ξ, Q_η and Q_ζ respectively as the coordinates that transform like yz,xz, and xy, the functions g_i are

given by [15]

$$g_1 = \frac{1}{2}k_E(Q_\theta^2 + Q_\epsilon^2) + \frac{1}{2}k_T(Q_\xi^2 + Q_\eta^2 + Q_\zeta^2) \tag{4.10}$$

$$g_\theta = \frac{1}{\sqrt{3}}V_{E_g}Q_\theta + N_E(Q_\epsilon^2 - Q_\theta^2) + N_1(2Q_\zeta^2 - Q_\xi^2 - Q_\eta^2) \tag{4.11}$$

$$g_\epsilon = \frac{1}{\sqrt{3}}V_{E_g}Q_\epsilon + 2N_EQ_\theta Q_\epsilon + \sqrt{3}N_1(Q_\xi^2 - Q_\eta^2) \tag{4.12}$$

$$g_\xi = V_{T_{2g}}Q_\xi + N_TQ_\eta Q_\zeta + N_2Q_\xi(\sqrt{3}Q_\epsilon - Q_\theta) \tag{4.13}$$

$$g_\eta = V_{T_{2g}}Q_\eta + N_TQ_\zeta Q_\xi + N_2Q_\eta(-\sqrt{3}Q_\epsilon - Q_\theta) \tag{4.14}$$

$$g_\zeta = V_{T_{2g}}Q_\zeta + N_TQ_\xi Q_\eta + 2N_2Q_\zeta Q_\theta \tag{4.15}$$

These constants were found by performing a CASSCF state-averaged calculation for the three lowest energy states of SF_6^+ for various displacements of the molecule away from the maximum symmetry configuration. These energies are shown in Figure 4.2. The CASSCF calculations were made using a basis of Hartree-Fock orbitals calculated for neutral SF_6. These three adiabatic energies were then fitted to the eigenvalues of the diabatic Jahn-Teller coupling matrix. This process yielded $V_{T_{2g}}$=.001209 H/bohr, V_{E_g}=.1406 H/bohr, N_1=-.0362 H/bohr^2, $K_{T_{2g}}$=.7288 H/bohr^2, K_{E_g}=1.8486 H/bohr^2. For the A_{1g} mode, which does not enter into the vibronic Hamiltonian, an adiabatic potential $E = V_{A_{1g}}Q_{A_{1g}} + 1/2K_{A_{1g}}Q_{A_{1g}}^2$, with $V_{A_{1g}}$=.0645 H/bohr, $K_{A_{1g}}$=2.98 H/bohr^2 gives the potential energy surface for all three electronic states.

Here there is a significant distinction between distortions of type E_g, which break the triple degeneracy but have no linear off-diagonal terms, and distortions of type T_{2g}, which do contribute to off-diagonal coupling. For small distortions, an adiabatic electronic state of an E_g distorted molecule will have the same symmetry – $\hat{x}$, $\hat{y}$, $\hat{z}$ – as the diabatic electronic states. The adiabatic electronic states of a T_{2g}-distorted molecule, on the other hand, are linear combinations of the diabatic orbitals. An important simplification is that $V_{T_{2g}}$, controlling off-diagonal coupling between different electronic states, is small in SF_6^+ and can be neglected for the short time between ionization and recombination.

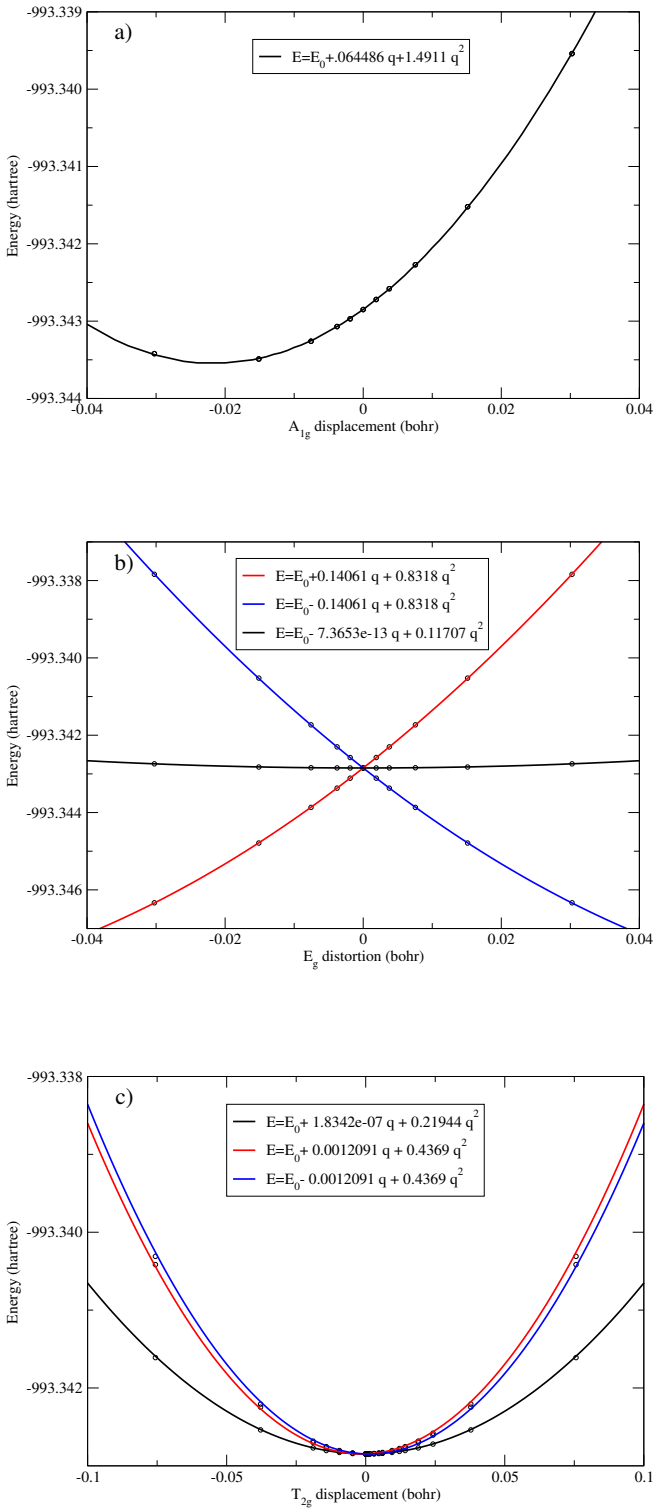

Figure 4.2: a)Spherically symmetric A_{1g} (breathing mode) distortions change electronic state energies, but preserve the triple degeneracy. Nontotally symmetric E_g (b) and T_{2g} (c) distortions break the triple degeneracy of SF_6^+ at the maximum symmetry point. Adiabatic energies are fit to the eigenvalues of the vibronic coupling matrix (equation 4.9) to solve for the vibronic coupling constants.

The evolution of the ionic wavefunction is calculated in the vibrational basis of the neutral molecule, but using potential energy surfaces calculated for the ion. Potential energy curves are found to quadratic order in Q using quantum chemistry calculations, then expressed in terms of raising and lowering operators by substituting $Q = (2m\omega)^{-1/2}(\mathbf{a} + \mathbf{a}^\dagger)$, $Q^2 = (2m\omega)^{-1}(\mathbf{a} + \mathbf{a}^\dagger)(\mathbf{a} + \mathbf{a}^\dagger)$. All terms up to linear in raising and lowering operators are then used to integrate the time-dependent Schrödinger equation to find a transfer matrix $\underline{N}$ describing the evolution of the ionic wavefunction between ionization and recombination.

Modulation of Harmonic Intensity In the two-state model used here, the $i-$th vibrational wavefunction of the neutral molecule after recombination has occurred is $|\psi_{\text{vib}}\rangle = d_0 |0\rangle + d_1 |1\rangle$, where

$$\begin{pmatrix} \vec{d}_0 & \vec{d}_1 \end{pmatrix} = \begin{pmatrix} a_0(0) & a_1(0)e^{-i\omega\tau} \end{pmatrix} \underline{M}^T \underline{I}^T \underline{N}^T \underline{\vec{R}}^T. \tag{4.16}$$

Here, e.g. $\underline{M}^T$ denotes the transpose of matrix $\underline{M}$.

The number of photons emitted in a given harmonic is proportional to $\vec{d}_0 \cdot \vec{d}_0^* + \vec{d}_1 \cdot \vec{d}_1^*$. The high harmonic intensity is a sum over all Raman active modes i:

$$P(\tau) = P_0 + \Sigma_i P_1^{(i)} \cos(\omega_i \tau + \delta_i). \tag{4.17}$$

The static P_0 primarily results from terms of the form $a_0(0)^* a_0(0)$, while P_1 results from terms of the form $a_0(0)a_1(0)^* e^{i\omega\tau}$ and $a_1(0)a_0(0)^* e^{-i\omega\tau}$. Defining $\underline{W} = \underline{M}^\dagger \underline{I}^\dagger \underline{N}^\dagger \underline{\vec{R}}^\dagger \cdot \underline{\vec{R}NIM}$, $P_0 = a_0(0)^* W_{00} a_0(0)$ and $P_1 \cos(\omega t + \delta) = \frac{1}{2}(a_1^* e^{i\omega\tau} W_{10} a_0(0) + \text{c.c.})$. Since I_1 and R_1 are small relative to I_0 and R_0, only their first-order terms are kept.

4.4 Describing the Continuum Electron

As seen in previous chapters, describing the evolution of the wavefunction for the active electron is itself a challenging problem. When the electron first tunnels free of the parent molecule, its wavefunction is determined by both the molecular potential and

the electric field of the laser. Once free, it propagates in the time-varying field of the laser while feeling a weak force due to Coulomb attraction to the parent ion. Finally it recollides with the parent ion, and is once again strongly distorted by the molecular potential.

A full solution of the time dependent Schrödinger equation for this process would be computationally demanding for complicated molecules such as SF_6. In addition, much of the information in the continuum wavefunction is not relevant to the HHG problem: only a small part of the wavefunction overlaps with the unoccupied orbital into which the rescattering electron recombines.

One frequently used treatment which avoids the complications of the full time-dependent Schrödinger equation [7, 34] is based on a classical or semiclassical propagation of the continuum electron, ignoring the ionic Coulomb potential. The returning electron wavefunction is then approximated as a plane wave throughout the recombination process. This approach has been successful in describing the high harmonic cutoff, the chirp of the emitted high harmonic light and other quantities of interest in atomic systems [33, 26]. However, as was shown in an earlier chapter, the plane wave approximation is not adequate to describe the returning electron because of the tremendous distortion caused by the electron's interaction with the ionic potential and by exchange effects with the other electrons in the molecule. For the time-reversed problem of photoionization, it is known that the plane wave approximation is prone to error for photoelectron energies smaller than the deepest k-shell binding energy. Energies attained in high harmonic generation experiments usually fall below this range.

This section gives an improved semiclassical model of the free electron propagation, which can be connected to short-range calculations of the tunneling and rescattering wavefunctions using stationary phase techniques. Any method could be used to calculate these short-range wavefunctions. In this treatment, the tunneling wavefunction is modeled semiclassically using ideas based on the initial value representa-

tion [37, 40]. The recolliding electron continuum wavefunction is described in terms of electron-molecule scattering states as used in chapter 3, calculated in the absence of an external electric field.

In this way, the molecular potential affects the electron wavefunction at the two times when the electron is near the molecule. When the electron is far from the molecule, the comparatively simple evolution of its wavefunction is described using the shortest-time, dominant contribution to the Gutzwiller propagator [21]. Finally, stationary phase arguments serve to identify the isolated trajectories that encapsulate the effect of the electron propagation in the field on high harmonic generation, greatly reducing the computational burden of propagating the continuum electron wavefunction.

4.4.1 Tunneling Ionization

During the ionization step, the tunneling electron wavefunction is described in a simple 1-D WKB tunneling picture, in which electrons are allowed to tunnel only in directions parallel to the laser's applied electric field. This approach is motivated by the semiclassical "Initial Value Representation" [37, 40], where a source wavefunction acquires an imaginary phase (and hence an exponential rise or fall) along a trajectory that passes through a classically forbidden region. The unperturbed molecular HOMO here serves as the source wavefunction, so that the tunneling wavefunction is approximated by the unperturbed HOMO in the classically allowed region near the molecule, connecting to a WKB exponential which is set equal to the HOMO at the inner turning point and decays exponentially until it reaches the outer turning point. SF_6 has three degenerate HOMOs: one of these is illustrated in Figure 4.3.

The classically forbidden region, illustrated in Figure 4.4, is defined by two turning points, a and b, between which $V(x) - E > 0$. The slope of $V(x)$ is C_1 at inner turning point a and C_2 at outer turning point b. The tunneling wavefunction $\psi_t(\vec{r}, t)$ is now found by applying WKB connection formulas. The appendix derives the ratio of the

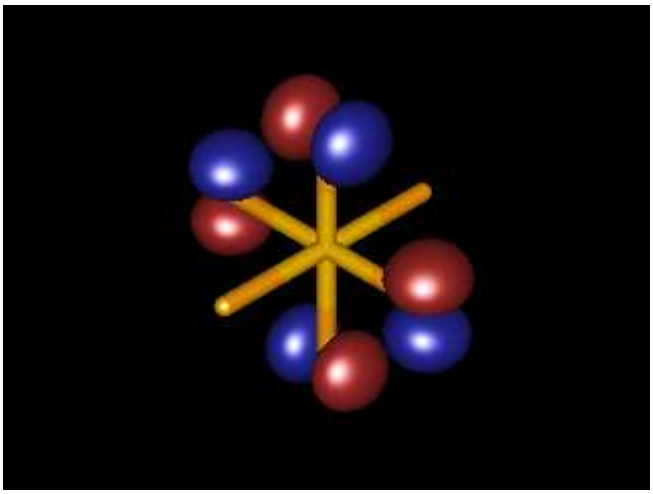

Figure 4.3: One of three degenerate orbitals of SF_6. Red denotes positive lobes; blue denotes negative lobes.

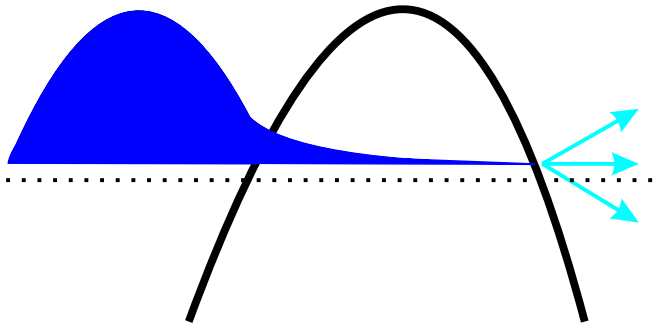

Figure 4.4: The tunneling wavefunction is approximated as an unperturbed molecular HOMO inside the classically allowed region, connecting to a declining WKB exponential in the classically forbidden region. Stationary phase trajectories leave from the outer turning point, beginning with zero velocity at time of ionization.

tunneling wavefunction at the outer turning point to the tunneling wavefunction at the inner turning point

$$\frac{\psi(x=b)}{\psi(x=a)} = \frac{1}{2}e^{-\Gamma}|\frac{C_1}{C_2}|^{1/6}\frac{\mathrm{Bi}(0)}{\mathrm{Ai}(0)} \tag{4.18}$$

In this approximation, the tunneling wavefunction behaves like an Airy Bi function near the outer turning point, **i.e.** it has no linear complex phase term. This property will be revisited in the section dealing with stationary phase analysis.

4.4.2 Semiclassical Propagation

When the active electron has tunneled free of the molecule, the evolution of its wavefunction is controlled by the oscillating electric field of the laser, plus a residual Coulomb attraction to the molecular ion. This relatively simple evolution continues until the electron returns to the molecule, when the complicated molecular potential again becomes significant. During this excursion, until it re-enters the non-Coulomb part of the potential, the continuum wavefunction can be approximated using Gutzwiller's

semiclassical propagator[21]:

$$K(\vec{r},t;\vec{r}_0,t_0) = \sum_{\text{Classical Trajectories}} (2\pi i)^{-3/2}\sqrt{C(\vec{r},t;\vec{r}_0,t_0)}\times \exp(iS(\vec{r},t;\vec{r}_0,t_0) - i\phi) \tag{4.19}$$

Here $S(\vec{r},t;\vec{r}_0,t_0)$ is the action integral $S = \int L(q,\dot{q},t)dt$ calculated for a classical trajectory starting at $(\vec{r}_0,t_0)$ and ending at $(\vec{r},t)$, while $C(\vec{r},t;\vec{r}_0,t_0) = |\frac{-\partial^2 S}{\partial r_{0,A}}\partial r_B|$, where r_A is the A-component of the vector $\vec{r}$. ϕ is a phase factor equal to $\frac{\pi}{2}$ times the number of conjugate points crossed by the trajectory[21].

This propagator acts on the tunneling wavefunction ψ_t to give a semiclassical continuum wavefunction

$$\psi_c(\vec{r},t) = \int d^3\vec{r}_0 \int dt_0 K(\vec{r},t;\vec{r}_0,t_0)\psi_t(\vec{r}_0,t_0). \tag{4.20}$$

until the molecular potential asserts itself during the rescattering.

During the terminal portion of the scattering process, when the scattering wavefunction has a large dipole matrix element with the molecular HOMO to which it recombines, the electronic wavefunction is expanded into a truncated but in principle complete basis of field-free electron-molecule scattering orbitals, calculated using techniques described in references [58, 59, 57]. Beyond the range of the molecular potential, i.e. for $r > r_0$, the (l,m)-th independent scattering state is expressed as a partial wave expansion in terms of incoming and outgoing Coulomb radial functions $f^{\pm}_{El}(r)$ and the scattering S-matrix as

$$\psi_{E,lm}(\vec{r}) = \frac{1}{i\sqrt{2}} f^{-}_{El}(r)Y_{lm}(\theta,\phi) - \frac{1}{i\sqrt{2}}\sum_{l'm'} f^{+}_{El'}(r)Y_{l'm'}(\theta,\phi)S_{l'm';lm}(E), r \geq r_0. \tag{4.21}$$

The laser electric field is typically far smaller when the electron returns to the ion. Neglecting its effect on the electron during its recollision with the ion, the time-dependent wavefunction becomes

$$\psi_{\text{scat}}(\vec{r},t) = \int dE \sum_{lm} A_{lm}(E)\psi_{E,lm}(\vec{r})e^{-iEt} \tag{4.22}$$

and the expansion coefficients $A_{l,m}(E)$ are given by

$$A_{lm}(E) = e^{iEt} \int d^3\vec{r}\psi^*_{E,lm}(\vec{r})\psi_c(\vec{r},t) \tag{4.23}$$

for some chosen time t when ψ_c is projected onto the scattering states.

The dipole recombination amplitudes

$$d_{l,m}(E) = \langle\psi_{E,lm}|\,\hat{\epsilon}\cdot\vec{r}\,|\psi_{\mathrm{HOMO}}\rangle \tag{4.24}$$

are calculated between the distorted scattering states and the molecular HOMO to which the electron recombines.

Equations [4.20] and [4.23] now define the expansion coefficients $A_{lm}(E)$ for some chosen projection time t, in terms of two three-dimensional integrals over initial and final positions, one integral over the time of ionization, and a summation over all possible classical trajectories. Stationary phase arguments dramatically simplify the calculation of these expansion coefficients.

4.4.3 Stationary phase calculation of scattering coefficients

The Gutzwiller propagator $K(\vec{r},t;\vec{r}_0,t_0)$ defined in equation [4.19] involves a summation over the classical paths having $(\vec{r}_0,t_0)$ and $(\vec{r},t)$ as their endpoints. Invoking the usual assumption that these paths are isolated, such classical paths have the property of extremizing the action integral $S(\vec{r},t;\vec{r}_0,t_0) = \int L(q,\dot{q},t)dt$. If the initial or final points of the paths are varied, a new extreme-action path connects the new endpoints, and a new extremal action corresponds to the new trajectory. From Goldstein et al [20] section 8.6, the change in the action integrals between the old classical path connecting the old endpoints and the new path connecting the new endpoints is called the Δ variation of the action. The Δ variation of the action is given by

$$\Delta S(\vec{r},t;\vec{r}_0,t_0) = (p_A\delta q_A - \hat{H}(t)\delta t)|^{\mathrm{final}}_{\mathrm{initial}} \tag{4.25}$$

Because $iS(\vec{r},t;\vec{r}_0,t_0)$ appears in the exponent of the Gutzwiller propagator, slight changes of $\vec{r}$ and $\vec{r}_0$ cause the phases of the integrals in equations 4.20 and 4.23 to vary rapidly, resulting in canceling contributions to the expansion coefficients. This cancellation occurs unless the Δ variation of the action is counteracted by the change of phase of the tunneling or scattering wavefunctions. A trajectory where the Δ variation of the action is counterbalanced by the phase of the tunneling wavefunction at $(\vec{r}_0,t_0)$ and by the phase of the scattering wavefunction at $(\vec{r},t)$ is a "stationary phase trajectory." The initial and final points $(\vec{r}_0,t_0)$ and $(\vec{r},t)$ identify the points in the 7D integral where the integrand oscillates slowly, giving a non-canceling contribution to the expansion coefficients $A_{lm}(E)$.

To find such trajectories, expand the phase-oscillating parts of the 7D integral

$$\begin{aligned} A_{lm}(E) = \int d^3\vec{r} \int d^3\vec{r}_0 \int dt_0 e^{iEt} \sqrt{C(\vec{r},t;\vec{r}_0,t_0)} \\ \exp(iS(\vec{r},t;\vec{r}_0,t_0) - i\phi)\psi^*_{E,lm}(\vec{r},t)\psi_t(\vec{r}_0,t_0). \end{aligned} \tag{4.26}$$

about starting point $(\vec{r}_{0c},t_{0c})$ and ending point $(\vec{r}_c,t)$

The Δ variation gives the expansion of the action integral

$$\begin{aligned} S(\vec{r}_c+\delta\vec{r},t;\vec{r}_{0c}+\delta\vec{r}_0,t_{0c}+\delta t_0) = S(\vec{r}_c,t;\vec{r}_{0c},t_{0c}) + \\ p_A\delta r_A + \frac{1}{2}\frac{\partial^2 S}{\partial r_A \partial r_B}\delta r_A \delta r_B + p_{0A}\delta r_{0A} + \\ \frac{1}{2}\frac{\partial^2 S}{\partial r_{0A}\partial r_{0B}}\delta r_{0A}\delta r_{0B} + \hat{H}\delta t_0 + \frac{1}{2}\frac{\partial^2 R}{\partial t_0^2}(\delta t_0)^2. \end{aligned} \tag{4.27}$$

Finally, ignoring the angular derivatives of the spherical harmonics, the asymptotic phase evolution of the scattering states is given through the asymptotic phase evolution of the Coulomb wave functions $f^{\pm}_{El}(r)$

$$\begin{aligned} \psi^*_{E,lm}(\vec{r}_c+\delta\vec{r}) = \frac{(2\pi i)^{-3/2}}{-i\sqrt{2}} f^{-*}_{El}(r_c) Y^*_{lm}(\theta_c,\phi_c)\exp(ik(r_c)\delta r) - \\ \sum_{l',m'} \frac{1}{-i\sqrt{2}} f^{+}_{El'} Y^*_{l'm'}(\theta_c,\phi_c) S_{l'm';lm}(E)\exp(-ik(r_c)\delta r) \end{aligned} \tag{4.28}$$

where $k_l(r) = \sqrt{(}2(E-V_l(r)))$. The tunneling wavefunction looks like a declining WKB exponential in the forbidden region; it has no oscillatory phase part.

The condition for a nonoscillating integrand is now that the first-order terms in $\delta\vec{r}_0$,$\delta\vec{r}$ and δt_0 must disappear. Setting the coefficients of δt_0 to zero gives

$$\frac{\vec{p}_0^2}{2m} + V(\vec{r}_0, t_0) = E_{\mathrm{HOMO}}. \tag{4.29}$$

Setting the coefficients of $\delta\vec{r}_0$ to zero in Eq. 4.23 gives

$$\vec{p}_0 = 0 \tag{4.30}$$

and setting the coefficients of $\delta\vec{r}$ to zero in Eq. 4.23 gives

$$p_r = \mp k(r) \tag{4.31}$$

for the radial integral, where $\mp$ corresponds to the incoming and outgoing wave parts of the scattering states. Restricting consideration to trajectories that are incoming at the time of projection, this last condition becomes

$$p_r = -k(r) = -\sqrt{2(E - V(r))}. \tag{4.32}$$

Neglect of the angular derivatives of the spherical harmonics gives that the trajectory must return with zero angular momentum.

Thus, a stationary phase trajectory is launched with zero momentum from the classical turning point and returns to the molecule with zero angular momentum, and kinetic energy equal to the energy of the scattering state. This is a familiar result from, **eg**, [7, 33], with the distinction that the present work considers the effect of the electron-ion Coulomb interaction during the continuum propagation of the electron. Also, the wavefunction is projected onto scattering states shortly before recollision, rather than treating the electron in a Volkov approximation throughout the recollision with the molecular ion. Because the electron-molecule scattering states are calculated with no external electric field present, there is a slight dependence on the time at which the wavefunction is projected onto scattering states; here the projection is made when ωt

for the laser cycle is equal to 3.9, i.e. when the short trajectories with energies equal to the energy of the 39th harmonic have nearly returned to the molecule.

Because the linear phase variation of the integrand vanishes in the vicinity of a stationary phase trajectory, the expansion coefficients $A_{lm}(E)$ are now found via Gaussian integrals:

$$\begin{aligned} A_{lm}(E) = (2\pi i)^{-3/2}\frac{i}{\sqrt{2}} f_{El}^{-*}(r_c) Y_{lm}^{*}(\theta_c,\phi_c)\times \\ \exp(iS(\vec{r}_c,t;\vec{r}_{0c},t_{0c}) - i\phi)\psi_t(\vec{r}_{0c})e^{-iE_{\mathrm{HOMO}}t_{0c}}\times \\ ((I) = \int d(\delta t_0)\exp(\frac{i}{2}\frac{\partial^2 S}{\partial t_0^2}(\delta t_0)^2))\times \\ ((II) = \int d^3(\delta\vec{r}_0)\exp(\frac{i}{2}\frac{\partial^2 S}{\partial r_{0A}\partial r_{0B}}\delta r_{0a}\delta r_{0B}))\times \\ ((III) = \int d^3(\delta\vec{r})\exp(\frac{i}{2}\frac{\partial^2 S}{\partial r_A \partial r_B}\delta r_A \delta r_B)) \end{aligned} \tag{4.33}$$

where the integrals labeled (I),(II) and (III) are evaluated as

$$(I) = \sqrt{2\pi i}|\frac{\partial^2 S}{\partial t_0^2}|^{-1/2} \tag{4.34}$$

$$(II) = (2\pi i)^{3/2}|\frac{\partial^2 S}{\partial r_{0A}\partial r_{0B}}|^{-1/2} \tag{4.35}$$

$$(III) = (2\pi i)^{3/2}|\frac{\partial^2 S}{\partial r_A \partial r_B}|^{-1/2} \tag{4.36}$$

yielding expansion coefficients

$$\begin{aligned} A_{lm}(E) = (2\pi i)^2\sqrt{|\frac{\partial r_A}{\partial p_{0B}}|}\times \\ (\frac{\partial^2 S}{\partial t_0^2})^{-1/2}\frac{i}{\sqrt{2}}\times \\ f_{El}^{-*}(r_c)Y_{lm}^{*}(\theta_c,\phi_c)\exp(iS(\vec{r}_c,t;\vec{r}_{0c},t_{0c}) - i\phi)\times \\ \psi_t(\vec{r}_{0c})e^{-iE_{\mathrm{HOMO}}t_{0c}} \end{aligned} \tag{4.37}$$

Once these expansion coefficients have been calculated, the dipole matrix element between the distorted scattering wave and the molecular HOMO is simply

$$\vec{D}(E) = \sum_{lm} A_{lm}(E)\vec{d}_{lm}(E). \tag{4.38}$$

4.5 Comparison with Experiment

The model of vibrational interference connects with this treatment of the high harmonic process when $\hat{I}\hat{\vec{R}}$ is set to $\vec{D}(E)$. This is broken up by setting $\hat{I} = \psi_t(\vec{r}_0, t_0)$ and $\hat{\vec{R}} = \vec{D}(E)/\hat{I}$. Both of these quantities are calculated for a molecule at the equilibrium geometry, and for a molecule displaced by 0.1 bohr in the normal mode coordinate. This involves recalculating the scattering states and recombination dipoles for each distorted molecular geometry.

The modulation of the 39th harmonic was chosen for purposes of comparison with experiment, since this harmonic was considered in detail in [63]. The 39th harmonic falls close to the measured cutoff, and can only be produced by a half-cycle coming close to the maximum of the gaussian envelope of the laser pulse.

The JILA experiment used a gas jet as a source of SF_6, giving no preferred molecular orientation. Both ionization and recombination amplitudes are highly dependent on orientation. A rotational average was calculated for both the static and oscillatory parts of the harmonic intensity. Only those polarizations perpendicular to the propagating laser beam for a given molecular orientation were included in these averages.

The non-totally symmetric E_g and T_{2g} modes of the molecule are stimulated by different amounts for different orientations of the molecule relative to the laser field. Ionization, recombination, and their derivatives are also highly orientation dependent. Because of this, although the E_g and T_{2g} modes modulate the harmonic intensity strongly for particular orientations of the molecule, the phase offset δ in $P_1 \cos(\omega\tau + \delta)$ from equation 4.17 changes with orientation, canceling some of the observed oscillation when the angular average is performed. Figure 4.5 shows the spherically averaged peak-to-peak modulation calculated when δ is allowed to vary for different molecular orientations and when δ is artificially set to 0 for all orientations. These two averages are compared to the two experimental runs for which the modulations for all three modes could be

distinguished from the background.

Although the agreement with experiment is not perfect, it is nevertheless significant that the simple model of vibrational interference presented here agrees with experiment to the correct order of magnitude. This is particularly notable in light of conventional Raman spectroscopy, in which the A_{1g} peak is 20 times more prominent than the others. It is difficult to precisely gauge the agreement of theory and experiment, due to the paucity of experimental data. Peak-to-peak modulations may vary by several percent from one experimental run to another [1] with SF_6, and at the time of writing, only two experimental runs could distinguish all three Raman frequencies from experimental noise. The modulation at 525 cm^{-1}, corresponding to the T_{2g} mode, appears most prominently in the experimental data, yet gives the smallest modulation in this treatment. The prominence of the T_{2g} mode modulation may suggest that the off-diagonal Jahn-Teller coupling $V_{T_{2g}}$ is larger than given by these calculations. Alternatively, it may be necessary to model the experiment in more detail – spatially varying laser intensity, uncontrolled carrier envelope phase, multiple laser half cycles, etc – than included in the present work.

4.6 Conclusions

The problem of high harmonic generation in molecules may be conceptually separated into two parts: the evolution of the continuum electron, and the evolution of the internal (vibrational) wavefunction of the parent ion. This paper describes the evolution of the continuum electron in a model which combines a semiclassical treatment of the propagation with a fully quantum mechanical description of the electron-molecule scattering. This flexible and robust model has a simple conceptual link to existing semiclassical models, yet allows for a sophisticated treatment of the complicated electron-molecule scattering. The internal dynamics of the parent ion are tracked throughout the high harmonic process. Together, these two innovations serve to give an unprecedented

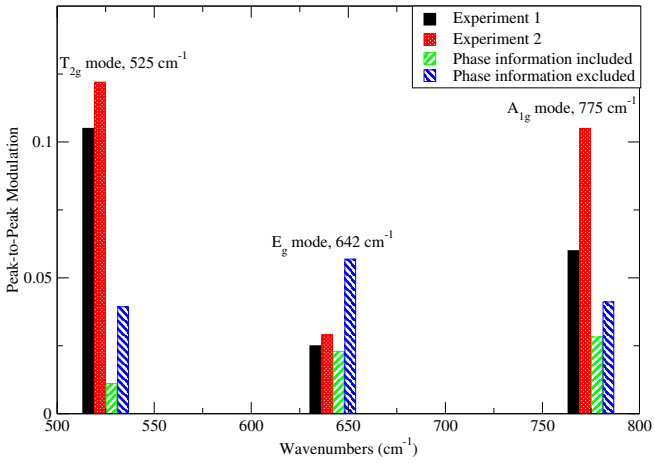

Figure 4.5: Peak-to-peak modulation of the high harmonic signal vs. wavenumber, comparing theory to the two experimental runs for which data is available. For the bars labeled "phase information included", the angular average was performed allowing δ in equation 4.17 to vary as a function of angle. For the bars labeled "phase information excluded," δ was set to zero for all angles. Modulations corresponding to the same frequency have been placed side-to-side for purpose of comparison. (Figure taken from [65])

view of high harmonic generation in a large, complicated molecule with many internal degrees of freedom, giving results which agree in order of magnitude to experiment.

The possibility that high harmonic generation may serve as an ultrafast interferometric probe of a molecular wavefunction is extremely promising. Such a wavefunction need not be prepared by an initial Raman pulse, as was done in the JILA experiment. Instead, a preparatory pulse could photoionize a molecule, excite it to a higher electronic state, or trigger the beginning of some other chemical process. In this way, wavepacket evolution during chemical processes could be observed as it happens.

4.7 Appendix: Tunneling Ionization

In this approximation, the wavefunction in the forbidden region is found using the WKB connection formulas. Illustrated in Figure 4.4, the classically forbidden region is defined by two turning points, a and b, between which $V(x) - E > 0$. The slope of $V(x)$ is C_1 at inner turning point a and C_2 at outer turning point b.

Near turning point a, $k^2(x) \equiv 2m(E-V(x)) \approx C_1(a-x)$ and the time independent Schrödinger equation is

$$\psi'' + k^2(x)\psi = 0, \tag{4.39}$$

which has solutions near $x = a$ of

$$\psi(x) = \mathrm{Ai}(\frac{C_1(x-a)}{C_1^{2/3}})b_1 + \mathrm{Bi}(\frac{C_1(x-a)}{C_1^{2/3}})b_2 \tag{4.40}$$

where Ai and Bi are Airy functions, asymptotically behaving like

$$\mathrm{Ai}(z) \Rightarrow_{z\to\infty} \quad (2\pi)^{-1/2} z^{-1/4} \exp[\tfrac{-2}{3} z^{3/2}] \tag{4.41}$$

$$\mathrm{Ai}(z) \Rightarrow_{z\to-\infty} \quad \pi^{-1/2}(-z)^{-1/4} \sin(\tfrac{2}{3}(-z)^{3/2} + \pi/4) \tag{4.42}$$

$$\mathrm{Bi}(z) \Rightarrow_{z\to\infty} \quad \pi^{-1/2} z^{-1/4} \exp(\tfrac{2}{3} z^{3/2}) \tag{4.43}$$

$$\mathrm{Bi}(z) \Rightarrow_{z\to-\infty} \quad \pi^{-1/2}(-z)^{-1/4} \cos(\tfrac{2}{3}(-z)^{3/2} + \pi/4) \tag{4.44}$$

where $z = C_1^{1/3}(x-a)$

Similarly, near $x = b$

$$\psi(x) = \mathrm{Ai}(C_2^{1/3}(b-x))d_1 + \mathrm{Bi}(C_2^{1/3}(b-x))d_2 \tag{4.45}$$

Under the barrier but away from the turning points, the WKB wavefunction is given by

$$\begin{aligned}\psi(x) = \pi^{-1/2}|k(x)|^{-1/2}\exp(\int_a^x |k(x')|dx')\sin(\phi) - \\ \frac{1}{2}|k(x)|^{-1/2}\exp(-\int_a^x |k(x')|dx')\cos(\phi)\end{aligned} \tag{4.46}$$

for some value of ϕ.

Setting $\int_a^b |k(x'|dx' \equiv \Gamma$, note that

$$\int_a^x |k(x')|dx' = \Gamma - \int_x^b |k(x'|dx' \tag{4.47}$$

and for x close to b

$$\int_b^x k(x')dx' = \frac{2}{3}C_2^{1/2}(x-b)^{3/2} \tag{4.48}$$

Connecting the asymptotic forms of the Airy functions to the WKB solution in the forbidden region gives the solution for $x \approx b$ as

$$\begin{aligned}\psi(x) =_{x\approx b} 2C_2^{-1/6}\sin(\phi)e^{\Gamma}\mathrm{Ai}(C_2^{1/3}(b-x)) - \\ \frac{1}{2}C_2^{-1/6}\cos(\phi)e^{-\Gamma}\mathrm{Bi}(C_2^{1/3}(b-x)),\end{aligned} \tag{4.49}$$

giving a scattering phaseshift δ of

$$\delta = \tan^{-1}(4e^{2\tau}\tan(\phi)) \tag{4.50}$$

yielding a resonance at $\phi \approx 0$, $\delta \approx \frac{pi}{2}$

Similar logic gives the wavefunction for $x \approx a$

$$\begin{aligned}\psi(x) =_{x\approx a} C_1^{-1/6}\sin(\phi)\mathrm{Bi}(C_1^{1/3}(x-a)) - \\ C_1^{1/6}\cos(\phi)\mathrm{Ai}(C_1^{1/3}(x-a))\end{aligned} \tag{4.51}$$

Finally, at resonance, $\phi = 0$ and the ratio of the tunneling wavefunction at the outer turning point to the tunneling wavefunction at the inner turning point is

$$\frac{\psi(x=b)}{\psi(x=a)} = \frac{1}{2}e^{-\Gamma}(|\frac{C_1}{C_2}|)^{1/6}\frac{\mathrm{Bi}(0)}{\mathrm{Ai}(0)} \tag{4.52}$$

Chapter 5

Laser-cluster interactions in the VUV energy range

Much of this thesis has dealt with the case of an isolated particle, exposed to a laser field which is treated classically. A single electron is liberated by the field, evolves in the continuum, and interacts once again with the parent ion. In many ways, the interaction of an atomic cluster with a vacuum ultraviolet (VUV) laser pulse does not fit this scenario.

Intense lasers have only recently become available at these photon energies, and the work done in this chapter was motivated by experiments [60] done at the free electron laser (FEL) at the Tesla Test Facility (TTF) in Hamburg, Germany. The capabilities of this facility are documented in Ref. [17]. In this work, van der Waals clusters of xenon atoms were exposed to 12.7 eV VUV photons, an energy range which had not previously been explored.

What they found at this new energy range was very surprising. At a laser intensity of 7×10^{13} W/cm^2, isolated xenon atoms were found to produce only singly charged ions [61, 48], corresponding to a single photon absorbed. However, when large clusters were exposed to pulses of this strength, each atom was found to absorb up to 400 eV, corresponding to 30 photons! In addition, charge states of up to 8+ were detected.

At first glance, the reason for surprise might not be apparent. Previous experiments with noble gas clusters of krypton,argon or xenon atoms performed with infrared lasers (photon energies 1 eV) [23] with peak intensities on the order of 10^{16} W/cm^2

and pulse lengths on the order of 100 fs had shown very efficient absorption of laser energy. The atoms in the cluster ionize to form nanoplasmas, accompanied by high charge states, strong x-ray emission and keV electrons[9, 51]. Experimental studies performed by Lezius **et al** [35] with Ar and Xe clusters found that the nanoplasmas undergo very energetic fragmentation, with ions of kinetic energies as large as 1 MeV ejected from the clusters.

In most models of the laser cluster interaction, designed to deal with infrared driving lasers, the dominant heating mechanism is collisional heating[8, 10]. In such a model, electrons tunnel free of their parent ions and are accelerated by the laser's electric field. However, because clusters have a very high local density of atoms, many electrons will scatter from atomic centers. It is therefore possible for an electron to be accelerated one way by the laser's electric field and scatter backwards from an atomic center at just the right time to be accelerated in the opposite direction by the laser's electric field, which has switched directions in the meantime.

A back of the envelope calculation reveals that this can be a very efficient mechanism for heating in the case that the ponderomotive potential of the driving laser is very large. For an applied electric field $E = E_0 \cos(\omega t)$, the kinetic energy of an electron in one dimension may be given as

$$KE = \frac{1}{2}(p - A)^2 = \frac{1}{2}(p^2 + A^2 - 2p \cdot A) \tag{5.1}$$

where the vector potential $A = -\frac{E_0}{\omega}\sin(\omega t)$ and the expectation value of p is $< p >= \frac{E_0}{\omega}\sin(\omega t)$. If each backscattering changes the momentum from p to $-p$, the average energy gain per collision is then $2 < p > A = 2\frac{E_0^2}{\omega^2}\sin^2(\omega t)$, which in turn averages to $\frac{E_0^2}{\omega^2} = 4U_p$[1] .

In the case where the cluster is subject to intense infrared lasers, with strong

[1] More calculations must be done to deal with the (much more likely) case of small angle elastic scattering. However, as the change in energy comes from the $p \cdot A$ term, the answer will be proportional to U_p, just as in the example.

electric fields and small laser frequencies, U_p can be very large and such a collisional heating mechanism can deliver great amounts of energy to the cluster plasma. However, VUV photons have very high frequency, while available sources cannot produce laser intensities as high as those which can be achieved with infrared lasers. In the Hamburg experiment, the free electron laser was able to produce intensities of 7×10^{13} W/cm^2, for a ponderomotive potential of only 62 meV, nearly three orders of magnitude smaller than the energy absorbed per atom!

Previous work [49] had indicated that inverse bremsstrahlung could serve as an effective heating mechanism. In this picture, electrons freed from their parent ions by an initial photoionization would form a small cluster plasma. They would be able to scatter from a xenon ion and absorb a photon from the laser field in the process (called inverse bremsstrahlung scattering). Santra **et al** made the further approximation that inverse bremsstrahlung cross sections should be calculated using realistic Herman-Skillman potentials rather than the pointlike Coulomb potentials used in prior treatments. Using such a potential, an electron passing near an atomic center would feel an effective charge Z_{eff} much greater than the total charge of the ion, since the inner-shell electrons would screen the nucleus less effectively. Because inverse bremsstrahlung cross sections go as Z^2, this could potentially have very large impacts on the rate at which the cluster plasma could absorb photons.

In [49], Santra and Greene had found that using Herman-Skillman atomic potentials increased the number of photons absorbed per atom from about 1 (using Coulomb potentials) to nearly 30. However, that study calculated inverse bremsstrahlung rates using perturbation theory for both the electron-photon and the electron-ion interaction, and did not consider such effects as collisional ionization or recombination, or the finite size of the clusters.

This chapter presents a model of the laser-cluster interaction in the VUV regime which includes the effects of non-Coulombic potentials as well as the evolution of the

cluster as it absorbs energy from the laser. The electron-ion interaction is treated nonperturbatively using variational R-matrix methods. The electron-photon interaction is treated using first-order perturbation theory. Although no electron correlation is used, this treatment is expected to give more realistic photoionization and inverse bremsstrahlung cross sections than those used in Santra **et al**. The model treats photoionization, collisional ionization and recombination, inverse bremsstrahlung heating, evaporation of electrons from the cluster, and expansion of the cluster due to hydrodynamic pressure of hot electrons and Coulomb repulsion. This work appeared first in [64].

5.1 Photoionization

One distinction between the Hamburg experiment and previous experiments done with IR lasers is that a single 12.7 eV photon has sufficient energy to ionize the highest bound electron of xenon, which has an ionization potential of only 12.1 eV. Thus, although the oscillating electric field is too weak to field ionize the xenon atoms, there is still an efficient mechanism to create an initial cluster plasma.

The cross section for the transition from the bound state $|\phi_i\rangle$ to the continuum state $|\phi_f\rangle$ is given by [19]

$$\sigma_{fi}(E) = 4\pi^2\alpha\omega|\vec{\pi}\cdot\vec{r}_{fi}|^2 \,, \tag{5.2}$$

where α is the fine-structure constant, ω is the photon energy, $\vec{\pi}$ is the polarization vector for the radiation, and $\vec{r}_{fi} = \langle\phi_f|\,\vec{r}\,|\phi_i\rangle$ is the dipole matrix element coupling the initial and final states of the electron. E is the kinetic energy of the photoelectron, whose wave function in Eq. (5.2) is energy-normalized.

For linearly polarized light, chosen to be polarized in the $\hat{z}$ direction, the relevant matrix element is

$$\langle\phi_f|\,z\,|\phi_i\rangle = I_R(l_i,l_f)\int d\Omega Y^*_{l_f m_f}(\Omega)\cos\theta Y_{l_i m_i}(\Omega) \,. \tag{5.3}$$

Here,

$$I_R(l_i, l_f) = \int_0^\infty dr U_f(r) r U_i(r) \ , \tag{5.4}$$

where $U(r) = rR(r)$ denotes the rescaled radial wave function.

At a photon energy of 12.7 eV, only the 5p electrons of xenon can be ionized by the laser field. Thus, the photoionization cross section may be calculated using only electrons from this shell. Using an independent electron model to deal with the q electrons in this shell, the total atomic photoionization cross section can be found by averaging over the initial and summing over the final one electron states to give

$$\begin{aligned} \sigma_{\rm PI} &= q\frac{4}{3}\pi^2\frac{\alpha\omega}{2l_i+1} \\ &\quad \times \left\{ l_i I_R^2(l_i, l_i-1) + (l_i+1) I_R^2(l_i, l_i+1) \right\} \end{aligned} \tag{5.5}$$

where $l_i = 1$ is the angular quantum number of the p shell. In calculating this result, the identities [46, 12]

$$\int d\Omega Y^*_{l_1 m_1}(\Omega) \cos(\theta) Y_{l_2 m_2}(\Omega) = \sqrt{(2l_1+1)(2l_2+1)}(-1)^{-m_1} \begin{pmatrix} l_1 & 1 & l_2 \\ -m_1 & 0 & m_2 \end{pmatrix} \begin{pmatrix} l_1 & 1 & l_2 \\ 0 & 0 & 0 \end{pmatrix} \ , \tag{5.6}$$

$$\sum_{m_1, m_2} \begin{pmatrix} l_1 & l_2 & l_3 \\ m_1 & m_2 & m_3 \end{pmatrix} \begin{pmatrix} l_1 & l_2 & l_3' \\ m_1 & m_2 & m_3' \end{pmatrix} = \frac{\delta(l_3, l_3')\delta(m_3, m_3')}{2l_3+1} \ , \tag{5.7}$$

and

$$(2l_1+1)(2l_2+1) \begin{pmatrix} l_1 & 1 & l_2 \\ 0 & 0 & 0 \end{pmatrix}^2 = \begin{cases} l_1+1 & \text{if } l_2 = l_1+1 \\ l_1 & \text{if } l_2 = l_1-1 \\ 0 & \text{otherwise} \end{cases} \tag{5.8}$$

were used. $\begin{pmatrix} l_1 & l_2 & l_3 \\ m_1 & m_2 & m_3 \end{pmatrix}$ represents the Wigner 3-j symbol, related to the Clebsch-Gordan coefficient by

$$\begin{pmatrix} l_1 & l_2 & l \\ m_1 & m_2 & m \end{pmatrix} = \frac{(-1)^{l_1 - l_2 - m}}{\sqrt{2l+1}} < l_1 m_1 l_2 m_2 | l_1 l_2 l - m > \ .$$

The radial integrals $I_R(l_i, l_f)$ [Eq. (5.4)] were calculated in the acceleration representation for wave functions generated by a variational eigenchannel R-matrix calculation [4] using a Herman-Skillman atomic potential [22].

Because of the efficient photoionization, the atoms in the cluster ionize quickly to form a dense nanoscale plasma at an early stage in the laser pulse. This plasma has the effect of screening the atomic potential felt by both bound and continuum electrons. This lowers the ionization potential and changes both the initial- and final-state electron wave functions. Because of this, cross sections for photoionization become larger as the screening length in the plasma become shorter. With sufficient screening, it becomes possible for ions to undergo additional photoionization.

To account for this process, the screened radial matrix elements were calculated using the same R-matrix methods as for isolated Xe atoms. However, before the initial- and final-state wave functions were calculated, the Herman-Skillman potential was multiplied by a Debye screening factor $\exp(-r/\lambda_D)$. (The electron Debye length is defined as $\lambda_D = \sqrt{T/(4\pi n_e)}$ [29], where the electron temperature T in this expression is given in units of energy. n_e is the electron density.) The resulting matrix elements and ionization potentials were then spline-interpolated in order to calculate the photoionization cross section for a particular screening length. For most calculations, this screening length was restricted to be no less than 4.64 bohr, the Wigner-Seitz radius of xenon at liquid density. Shorter screening lengths are discussed in a later section.

5.2 Inverse Bremsstrahlung Heating

A second effect of having a high density of free electrons in the cluster plasma is that these electrons can undergo both stimulated and inverse bremsstrahlung processes, creating a second mechanism by which energy can be absorbed in the cluster. Such processes are the quantum mechanical analogue of the collisional heating mechanism discussed earlier. Stimulated bremsstrahlung refers to photoemission into the laser

mode by an electron colliding with an ion in the plasma, while inverse bremsstrahlung refers to the opposite process of an electron absorbing a photon in such a collision. Because each bremsstrahlung event results in 12.7 eV deposited into or removed from the plasma, such processes serve a large role in heating the plasma.

Collisions of electrons with cluster ions are treated as independent events, allowing heating rates to be found by calculating cross sections for a single electron-ion collision. The cross section per unit energy for a free-free transition from initial state $|\phi_{E',l',m'}\rangle$ to final state $|\phi_{E,l,m}\rangle$ can be shown using Fermi's golden rule, to equal

$$\sigma_{E,l,m\leftarrow E',l',m'} = \frac{4\pi^2\alpha}{\omega^3}\left|\langle\phi_{E,l,m}|\,\frac{\partial V}{\partial z}\,|\phi_{E',l',m'}\rangle\right|^2 . \tag{5.9}$$

$E = E' - \omega$ in the case of photon emission, $E' + \omega$ in the case of photon absorption. Equation (5.9) describes the interaction of linearly polarized radiation in the acceleration representation. V is the plasma-screened atomic potential experienced by the scattered electron.

As with photoionization cross sections, radial wave functions were calculated using a nonperturbative eigenchannel R-matrix approach. Matrix elements between the energy-normalized wave functions were calculated in the acceleration gauge, where the where the $1/r^2$ long-range dependence of $\partial V/\partial z$ ensures that the radial integral will converge, although the continuum electron wave functions are not spatially normalizable.

Bremsstrahlung processes act as a powerful heating process even though microscopic reversibility ensures that cross sections for absorption and emission cross sections have the same magnitude. This occurs because lower energy states are more highly populated than higher energy states in a thermal distribution. This study assumed that the electron gas reequilibrates rapidly after each bremsstrahlung event due to frequent electron-electron collisions. Heating rates are then calculated assuming that the electron

probability distribution $\rho(E)$ is at all times given by a Maxwell-Boltzmann distribution

$$\rho(E) = 2\sqrt{\frac{E}{\pi T^3}} e^{-E/T} \ . \tag{5.10}$$

Using this distribution, it is possible to derive an expression for the change in electron temperature with respect to time due to inverse bremsstrahlung processes.

The cross section defined in Eq. (5.9) describes a free-free transition between orbital angular momentum eigenstates. We therefore introduce $\rho(E, l, m)$, which is the probability per unit energy to find an electron in the state $|\phi_{E,l,m}\rangle$. Clearly, $\rho(E) = \sum_{l,m} \rho(E, l, m)$. If the wave function is normalized within a large sphere of radius R (not to be confused with the cluster radius), then the largest l that contributes to this sum at a given kinetic energy E is $l_{max} = R\sqrt{2E}$ [2]. Since, in thermal equilibrium, $\rho(E, l, m)$ can depend only on E, we see that

$$\rho(E, l, m) = \frac{\rho(E)}{2R^2 E} \tag{5.11}$$

in the limit of large R ($l_{max} \gg 1$).

We are interested in radiation-induced heating, i.e. in the change of the electron temperature due to photon absorption and emission. To this end, we will derive from

$$\frac{\partial T}{\partial t} = \frac{2}{3} \int_0^\infty dE E \sum_{l,m} \frac{\partial \rho(E, l, m)}{\partial t} \tag{5.12}$$

a rate equation for the electron temperature, expressed in terms of the cross sections for stimulated and inverse bremsstrahlung (Eq. (5.9)). As a final step in writing down the equation for the time evolution of $\rho(E, l, m)$, we must take into consideration that $\rho(E, l, m)$ refers to (spherical) box normalization, while the cross section per unit energy in Eq. (5.9) is based on energy-normalized wave functions. For the sake of consistency, it is necessary to change the initial state in the free-free radiative transition in Eq. (5.9) from energy normalization to box normalization. This has the effect of multiplying the cross section by $\pi\sqrt{2E}/R$.

Hence, if there are N_a atomic scatterers within the normalization volume and a laser beam of intensity I, the rate of change of $\rho(E,l,m)$ is given by

$$\frac{\partial\rho(E,l,m)}{\partial t} = N_a \frac{I}{\omega}\frac{\sqrt{2}\pi}{R}\times$$
$$\sum_{l',m'}\Big\{\sigma_{E,l,m\leftarrow E-\omega,l',m'}\sqrt{E-\omega}\rho(E-\omega,l',m') + \sigma_{E,l,m\leftarrow E+\omega,l',m'}\sqrt{E+\omega}\rho(E+\omega,l',m')$$
$$- \sigma_{E+\omega,l',m'\leftarrow E,l,m}\sqrt{E}\rho(E,l,m) - \sigma_{E-\omega,l',m'\leftarrow E,l,m}\sqrt{E}\rho(E,l,m)\Big\} \ .$$

The first row in the curly brackets in Eq. (5.13) describes the population of $|\phi_{E,l,m}\rangle$ via photoabsorption (photoemission) from states with energy $E-\omega$ $(E+\omega)$; the second row describes the depopulation of $|\phi_{E,l,m}\rangle$ due to photoabsorption and photoemission from this state. Equation (5.13) implies a nondegenerate electron gas.

An electron state with energy E will then communicate with states of energy $E-\omega$, which are on average more densely populated than itself. Since the absorption- and emission cross sections are equal, this tends to populate the state of energy E and depopulate the states of energy $E-\omega$, resulting in a net heating. The state will also communicate with states of energy $E+\omega$, which are less densely populated than itself, thereby again tending to populate the higher-energy states while depopulating the lower-energy state.

Combining Eqs. (5.10), (5.11), (5.12), and (5.13), we are led in a natural way to the following definition of the inverse bremsstrahlung cross section (per unit energy):

$$\sigma_{E+\omega\leftarrow E} = \sum_{l,m}\sum_{l',m'}\sigma_{E+\omega,l,m\leftarrow E,l',m'} \ . \tag{5.13}$$

Using Eqs. (5.6), (5.7), (5.8), and (5.9), this can be written as

$$\begin{aligned}\sigma_{E+\omega\leftarrow E} &= \frac{4}{3}\pi^2\frac{\alpha}{\omega^3} \\ &\quad\times\sum_l\left\{lJ_R^2(l,l-1)+(l+1)J_R^2(l,l+1)\right\} \ ,\end{aligned} \tag{5.14}$$

where

$$J_R(l,l') = \int_0^\infty dr U_{E+\omega,l}(r)\frac{dV}{dr}U_{E,l'}(r) \ . \tag{5.15}$$

The rate of change of the electron temperature due to inverse bremsstrahlung is then

$$\begin{aligned}\frac{\partial T}{\partial t} &= \frac{2}{9} n_a I \left(\frac{2\pi}{T}\right)^{3/2} \left[1 - e^{-\omega/T}\right] \\ &\quad \times \int_0^\infty dE e^{-E/T} \sigma_{E+\omega \leftarrow E} \ . \end{aligned} \tag{5.16}$$

The parameter n_a stands for the number of atoms per unit volume. In general, the ions in the plasma are not all in the same charge state. Denoting the fraction of Xe^{i+} by $f^{(i)}$, $\sigma_{E+\omega \leftarrow E}$ in Eq. (5.16) is replaced with $\sum_i f^{(i)} \sigma^{(i)}_{E+\omega \leftarrow E}$, where $\sigma^{(i)}_{E+\omega \leftarrow E}$ is the inverse bremsstrahlung cross section in the field of Xe^{i+}.

Figures 5.1 and 5.2 illustrate the dramatic effects of the ionic potential on the inverse bremsstrahlung cross section. In Fig. 5.1, as the scattering electron collides with the ion at higher and higher initial energies, it probes regions of the ionic potential at which the ion nucleus is screened increasingly poorly by inner-shell electrons. As a result, the inverse bremsstrahlung cross section rises to many hundreds of times that of the naked Coulomb potential.

Adding plasma screening to this picture has the effect of supplementing the screening effects of inner-shell electrons with the screening effects of plasma electrons. As a result, the scattering electron feels the effects of the ionic nucleus more strongly than in the pure Coulomb case, but less strongly than in the case of the unscreened ionic potential. This is seen in a steady decrease of the inverse bremsstrahlung cross section as the screening range decreases.

5.3 Collisional Ionization and Recombination

Although photoionization and inverse bremsstrahlung are the only processes by which the cluster can absorb photons from the laser beam, they are not by themselves enough to explain the cluster's evolution. As the pulse progresses, large numbers of free electrons fill the cluster. These electrons can liberate other electrons via collisional ionization if they have sufficient energy, or they can undergo three-body recombination

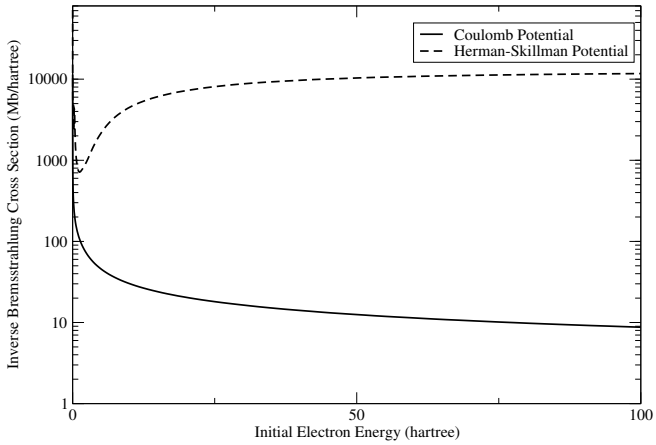

Figure 5.1: Inverse bremsstrahlung cross sections [Eqs. 5.13 and 5.14] for an electron with incident energy E to absorb a 12.7-eV photon are given for an electron in the field of a purely Coulombic 1+ potential and for an electron in the field of a Xe Herman-Skillman atomic potential. The effects of atomic structure on inverse bremsstrahlung rates are quite pronounced. Figure taken from [64].

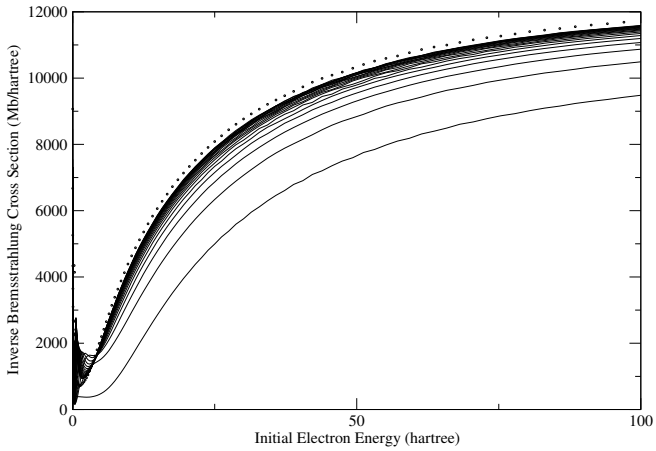

Figure 5.2: The inverse bremsstrahlung cross section as a function of energy is shown for an electron in the field of a Debye-screened Xe Herman-Skillman potential, with the Debye screening length λ_D ranging from 1 a.u. to 20 a.u. As λ_D grows, the cross section approaches the limit of no plasma screening, shown in this graph by the dotted line. As the Debye length of the cluster plasma shrinks, the charged ion is shielded more effectively from the scattering electron, and the inverse bremsstrahlung cross section is decreased. Figure taken from [64].

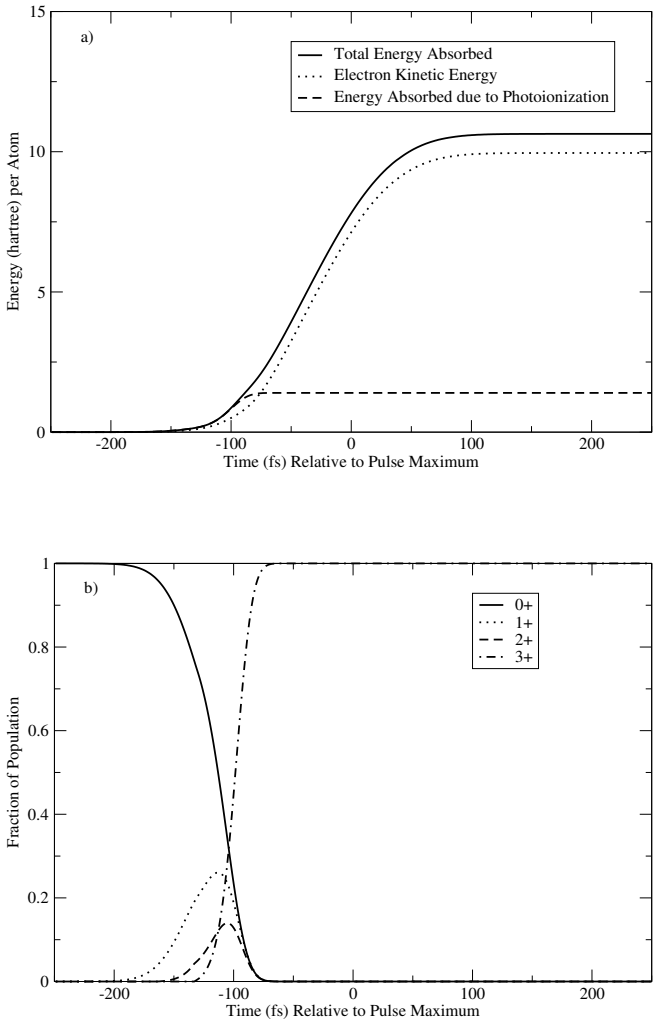

Figure 5.3: Evolution of a 1500 atom cluster exposed to a 100 fs, 7×10^{13} W/cm^2 pulse, employing only photoionization and inverse bremsstrahlung heating. a) Energy absorbed vs. time. b) Ionic population vs. time. Xe^{2+} and Xe^{3+} are produced efficiently via photoionization. Figure taken from [64].

with an ion, thereby heating the plasma.

These processes do not directly involve laser photons, but they nevertheless play an important role in the heating of the cluster. Because inverse bremsstrahlung goes as the square of the ionic charge, even small populations of highly charged ions can have great impacts on the rate at which the cluster is heated. In addition, the ability for a cold plasma to gain energy through recombination and a hot plasma to lose it through ionization allows the cluster ions to act as an energy reservoir for the plasma electrons throughout the pulse[2] .

Including the effects of ionization and recombination, the rate equation for the number per unit volume n_i of charge species i is given by

$$\begin{aligned} \frac{\partial n_i}{\partial t} &= \frac{I}{\omega}(\sigma_{\mathrm{PI}}^{i-1}\, n_{i-1} - \sigma_{PI}^{i}\, n_i) \\ &\quad + S_{i-1} n_{i-1} n_e - S_i n_i n_e \\ &\quad + R_{i+1} n_{i+1} n_e^2 - R_i n_i n_e^2 \,, \end{aligned} \tag{5.17}$$

where n_e is the number of electrons per unit volume. The photoionization cross sections σ_{PI}^{i} were calculated in Section 5.1. The ionization and recombination coefficients S_i and R_i for the reaction $\mathrm{Xe}^{i+} + \mathrm{e}^- \rightarrow \mathrm{Xe}^{(i+1)+} + 2\mathrm{e}^-$ are calculated later in this section.

The evolution of the cluster is found by integrating these equations numerically, along with equations for the energy in the free electron gas and the radius of the cluster. As a general rule, this set of equations is quite stiff. We performed this integration using the Rosenbrock method [44].

There are two requirements for a satisfactory treatment of collisional ionization and recombination in the cluster. First, both processes must occur at appropriate rates. Second, the rates for ionization and recombination must be consistent with one another, in the sense of driving the cluster toward chemical equilibrium at all times. The

[2] During the pulse, energy is typically deposited into the cluster too quickly for the charge state distribution to equilibrate. Thus, although the charge state distribution may act as an energy reservoir for the plasma electrons, it is typically far from being in thermodynamic equilibrium.

second requirement is particularly significant because the usual treatment of collisional ionization (also used in this study) uses the semiempirical Lotz formula [36] for ionization from the j^{th} subshell,

$$\begin{aligned} S_i^j &= 6.7 \times 10^{-7} \frac{a_j q_i^j}{T^{3/2}} \left(\frac{1}{P_j/T} \int_{P_j/T}^{\infty} \frac{e^{-x}}{x} dx \right. \\ &\quad \left. - \frac{b_j \exp(c_j)}{P_j/T + c_j} \int_{P_j/T+c_j}^{\infty} \frac{e^{-y}}{y} dy \right) \frac{\text{cm}^3}{\text{s}} , \end{aligned} \tag{5.18}$$

to find ionization coefficients. In the Lotz formula, a_j, b_j, c_j are semiempirical constants, q_i^j the number of equivalent electrons Xe^{i+} contains in the j^{th} subshell, P_j the ionization potential in eV, and T the temperature in eV. For charge states of $0, \ldots, 5+$, semiempirical constants corresponding to the 5p sublevel are chosen. For charge states of 6+ and 7+, which have no 5p electrons in the ground state, constants are chosen which correspond to the 5s sublevel. Because this formula is only a semiempirical approximation, it is important to use recombination coefficients which are consistent with the ionization coefficients to prevent the model from settling into an incorrect equilibrium charge distribution.

The ratio between ionization and recombination coefficients can be obtained using the concept of equilibrium constants. In a plasma at equilibrium, the rate of collisions ionizing Xe^{i+} to form $\text{Xe}^{(i+1)+} + e^-$ must be equal to the rate at which $\text{Xe}^{(i+1)+} + e^-$ recombines to form Xe^{i+}. However, the relative populations of reactants and byproducts at equilibrium is a thermodynamic property of the system which does not depend on intimate knowledge of ionization and recombination rates. Recombination coefficients consistent with the correct relative populations at equilibrium can then be applied to modeling the cluster plasma, which is not in general in a state of chemical equilibrium.

These two rates are given respectively by

$$S_i n_i n_e = \text{rate of ionizing collisions} \tag{5.19}$$

and

$$R_{i+1} n_{i+1} n_e^2 = \text{rate of recombining collisions} . \tag{5.20}$$

Hence, the ratio S/R is given by

$$\frac{S_i}{R_{i+1}} = \frac{n_{i+1}^{eq} n_e^{eq}}{n_i^{eq}} . \tag{5.21}$$

The fraction $(n_{i+1}^{eq} n_e^{eq})/n_i^{eq}$ is known as the equilibrium constant for the reaction, and can be calculated thermodynamically.

In any reaction $A \rightarrow B+C$ at equilibrium, the chemical potentials for the forwards and backwards reactions must be balanced $\mu_A = \mu_B + \mu_C$. The chemical potential of each species is given by a partial derivative of the Helmholtz free energy,

$$\mu_i = \frac{\partial F}{\partial N_i}_{T,V} . \tag{5.22}$$

The Helmholtz free energy is given by $F = -T \ln Z_{tot}$, where Z_{tot} is the partition function for the system as a whole.

Factoring the total partition function into the product of individual particle partition functions (which implies independent particles),

$$\begin{aligned} Z_{tot}(N_A, N_B, N_C, V, T) =& Z_A(N_A, V, T) Z_B(N_B, V, T) Z_C(N_C, V, T) \\ =& \frac{z_A(V,T)^{N_A}}{N_A!} \frac{z_B(V,T)^{N_B}}{N_B!} \frac{z_C(V,T)^{N_C}}{N_C!} , \end{aligned} \tag{5.23}$$

and assuming $N_i >> 1$ yields

$$\mu_i = -T \frac{\partial \ln(Z_i(V,T))}{\partial N_i} = -T \ln(\frac{z_i}{N_i}) . \tag{5.24}$$

Imposing balanced chemical potentials yields

$$\frac{N_B N_C}{N_A} = \frac{z_B(V,T) z_C(V,T)}{z_A(V,T)} \tag{5.25}$$

or equivalently

$$K_{\text{eq}}(T) = \frac{n_B n_C}{n_A} = \frac{\frac{z_B(V,T)}{V} \frac{z_C(V,T)}{V}}{\frac{z_A(V,T)}{V}} , \tag{5.26}$$

where the equilibrium constant $K_{\rm eq}$ is a function of temperature only.

If the ionization potential of Xe^{i+} is given by P_i, then the partition functions are given by

$$\begin{aligned} z_i &= \int_0^\infty dE e^{-E/T} \rho_i(E) \, , \\ z_{i+1} &= e^{-P_i/T} \int_0^\infty dE e^{-E/T} \rho_{i+1}(E) \, , \\ z_e &= \int_0^\infty dE e^{-E/T} \rho_e(E) \, . \end{aligned} \tag{5.27}$$

Through most of the lifetime of the pulse, tight plasma screening destroys the Rydberg states and most of the internal degrees of freedom of the various ions, leaving the density of states $\rho(E)$ dominated by the center of mass term and by a combinatorial term

$$D(i) = \binom{m}{n} \tag{5.28}$$

accounting for the number of ways n electrons can be distributed in m orbitals. For charge states up to 6+, we use $m = 6, n = 6-i$. For 7+ and 8+, we use $m = 2$,$n = 8-i$. If we exploit this by setting $\rho_i(E)/D(i) = \rho_{i+1}(E)/D(i+1)$, the common integral in z_i and z_{i+1} falls out of the equilibrium constant, yielding

$$K_{\rm eq}^{(Xe^{i+} \rightarrow Xe^{(i+1)+} + e^-)} = e^{-P_i/T} \frac{T^{\frac{3}{2}} D(i+1)}{\sqrt{2}\pi^{\frac{3}{2}} D(i)} \tag{5.29}$$

Equation (5.29) can now be combined with Eqs. (5.19) and (5.21) to yield recombination rate coefficients which have appropriate magnitude and which, in combination with the ionization coefficients, drive the system toward the correct equilibrium distribution at all times.

A gas of charged particles has different thermodynamic properties from an ideal gas due to Coulomb interactions between the constituent particles. Zel'dovich and Raizer [67] calculate the adjustment to $K_{\rm eq}$ due to a Debye-Hückel potential. The equilibrium constant including Coulomb effects can be written

$$K_{\rm eq}^{(Xe^{i+} \rightarrow Xe^{(i+1)+} + e^-)} = e^{-(P_i + \Delta P_i)/T} \frac{T^{\frac{3}{2}} D(i+1)}{\sqrt{2}\pi^{\frac{3}{2}} D(i)} \, , \tag{5.30}$$

where the change in ionization potential due to Coulomb effects is $\Delta P_i = -(Q_i+1)/\lambda_D$, the Coulomb potential between the ion core and an electron held at distance λ_D.

In our approach, by explicitly calculating bound state energies for Debye-screened Hartree-Slater potentials, we calculate this adjustment to the ionization potential directly. Our adjustment behaves similarly to the Zel'dovich and Raizer correction, but is larger for longer screening lengths and smaller at shorter screening lengths.

One advantage to the equilibrium constant approach is that it conceptually separates information about thermodynamic balance from the rate at which the system seeks that balance. As a result, any formula for ionization or recombination coefficients could be substituted for the Lotz formula, with the accuracies of the overall rate and of the equilibrium constant used the only criteria for validity of the formula.

Including the effects of collisional ionization and recombination has a pronounced effect on the evolution of the cluster. In Fig. 5.3, the evolution of the cluster is calculated employing only photoionization and inverse bremsstrahlung. In contrast, Fig. 5.7 shows the evolution of the same cluster employing photoionization, inverse bremsstrahlung, collisional ionization and recombination, and evaporation of energetic electrons from the cluster. Allowing ionization and recombination has the effect of producing charge states up to Xe^{8+} in substantial quantities, and of nearly doubling the energy per atom absorbed by the cluster.

5.4 Cluster Dynamics during the Laser Pulse

As the cluster absorbs energy from the laser field, some of the electrons become so energetic that they are no longer bound to the cluster. In addition, hydrostatic forces from the hot electrons and Coulomb repulsion in the now positively charged cluster cause the cluster to expand and cool. These in turn affect the microscopic processes inside the cluster, since all such processes depend on the concentrations of charge species within the cluster. Collisional ionization and recombination are also sensitively dependent on

the temperature of the electron gas relative to the electron binding energy.

The assumption that the electron gas reequilibrates rapidly compared to the rate of photoabsorption can be tested by calculating both rates at all times during the pulse. The characteristic time scale for energy relaxation in a plasma is controlled by the time taken for an electron at the plasma temperature to undergo a large-angle deflection as th result of scatterings with other electrons in the plasma. Eliezer, chapter 9.3 [13] gives this characteristic time as (using atomic units, and putting T in units of energy)

$$\tau = \frac{3\sqrt{6}}{8} \frac{T^{3/2}}{\pi n_e \ln \Lambda}. \tag{5.31}$$

This thermalization was compared with the characteristic time for interaction with the laser beam, defined as the inverse of the total rate of stimulated plus inverse bremsstrahlung processes per electron in the plasma. The resulting ratio, shown in Figure 5.4 is highest when the photon flux is low, and falls to a minimum of about 10 when the laser pulse reaches its maximum. Thus, the plasma electrons reequilibrate much faster than they interact with the laser at all times during the cluster evolution.

The cluster's expansion during the pulse was tracked using a simple model [10] which tracks only the radius of the cluster, the evaporation of electrons away from the cluster, and the loss of heat from the electron gas resulting from both processes. Gross movement of electrons or spatial inhomogeneity of charge species within the cluster were not considered, although a prior study [52] had suggested that such processes may account for the formation of the highly charged ions detected at the Hamburg experiment.

Since all processes considered in this model are at most linear with respect to ion concentration and are integrated over a cluster of finite volume, such quantities as the total rate of energy absorption or the total rates of Xe^{n+} ionizing to form $Xe^{(n+1)+}$ and recombining to form $Xe^{(n-1)+}$ are proportional to the number of ions of the given charge state found in the cluster, but do not change in the event that the charge state

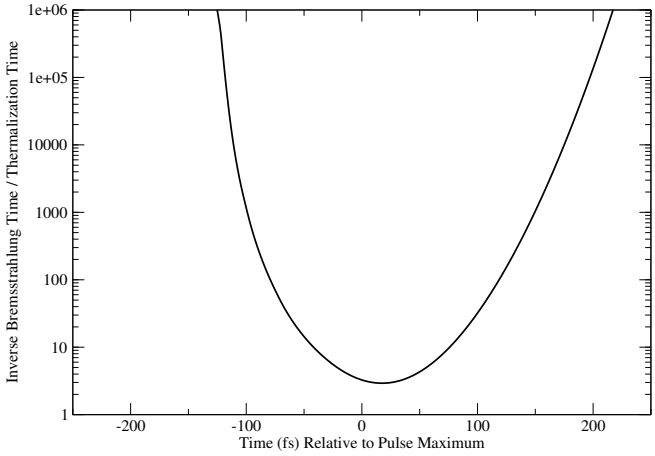

Figure 5.4: Comparison of thermalization time with time to undergo stimulated or inverse bremsstrahlung for an electron in the cluster plasma, calculated for a 1500 atom cluster exposed to a 7×10^{13} W/cm^2, 100 fs pulse, using the Wigner-Seitz cutoff model for screening. The electrons thermalize much faster than they interact with the laser at all times during the laser pulse. Figure taken from [64].

distribution is inhomogeneous. Thus, at the level of approximation used, the model would give identical results if it allowed for spatial inhomogeneity of the various charge species.

Spatial inhomogeneity of electrons, which was not considered in this study, is potentially very significant. Volumes with higher electron densities should see higher rates of inverse bremsstrahlung, collisional ionization and recombination. Subsequent studies [69, 70] performed using a statistical Boltzmann approach [68] found inhomogeneous distributions of both ions and electrons, with a neutral core filled with highly charged ions and a high density of electrons. Surrounding this core is a shell of less highly charged xenon ions. This shell has a net positive charge due to a lower density of electrons. Surrounding the cluster is a cloud of electrons which have enough energy to escape the cluster. The combination of high electron density and highly charged ions at the center of the cluster would likely increase the total energy absorbed by the cluster compared to the current model.

The equation for the radius of the cluster is given by

$$\frac{\partial^2 r}{\partial t^2} = 3\frac{P_e + P_{\mathrm{Coul}}}{n_{\mathrm{Xe}} m_{\mathrm{Xe}}}\frac{1}{r}\,, \tag{5.32}$$

where $P_e = n_e T_e$ is the electron pressure and $P_{\mathrm{Coul}} = Q^2/(8\pi r^4)$ is the Coulomb pressure resulting from the charge built up as electrons evaporate away from the cluster.

This model of the laser-cluster dynamics also distinguishes between inner and outer ionization. Inner ionization, which takes place due to photoionization and collisional ionization, is the process by which electrons become liberated from their parent ion and join the cluster plasma, where they can undergo inverse bremsstrahlung heating or collisional ionization or recombination. Outer ionization is the process by which electrons with sufficient energy escape the cluster and cease to interact with it.

The rate of evaporation from a Maxwell distribution of electrons can be calculated knowing the size of the cluster, the mean free path of electrons in the cluster, and the

temperature of the electron plasma. The rate at which electrons escape from the cluster is then given by

$$W_{fs} = \int_{v_{esc}}^{\infty} dv \frac{\pi}{4} \frac{\lambda_e}{r} (12r^2 - \lambda_e^2) v f(v) \tag{5.33}$$

where $v_{esc} = \sqrt{2(Q+1)/r}$ is the velocity required for an electron to escape from a cluster of charge Q,

$$f(v) = 4\pi n_e (2\pi T)^{-3/2} v^2 e^{-\frac{v^2}{2T}}$$

is the Maxwell distribution, and λ_e is the mean free path in the cluster plasma, given by

$$\lambda_e = \frac{T^2}{4\pi n_e (Z+1) \ln \Lambda}$$

for a plasma with average ion charge Z. The Coulomb logarithm, $\ln \Lambda$, is set equal to the logarithm of the screening length in our calculation of the mean free path. λ_e is constrained to be no greater than $2r$, the diameter of the sphere.

As electrons evaporate from the cluster, the remaining cluster becomes ever more highly charged, and a correspondingly lower fraction of the Maxwell distribution has enough energy to escape from the cluster, thereby choking off the evaporation rate.

It is likely that nearly all high-energy electrons detected in the experiment escape during this original period of evaporation. As the cluster expands, the temperature of the electron plasma falls very quickly as electron thermal energy is converted into ion kinetic energy, while the energy required to escape the cluster falls only as 1/r.

A recent experiment [30] has for the first time measured the energy spectrum for electrons emitted from rare gas clusters exposed to intense VUV light. They give ejection spectra for 70 atom xenon clusters exposed to a 4.4×10^{12} W/cm^2 pulse of VUV light at the same photon energy as the original Hamburg experiment, finding an electron distribution which decreases approximately exponentially according to $I = I_0 \exp(-E_{\rm kin}/E_0)$, with $E_0 = 8.9$ eV.

The energy spectrum of ejected electrons was calculated by stepping through a

laser pulse using small timesteps. At each timestep, the electron density, mean free path, cluster radius, and plasma temperature were calculated. These parameters were then used to calculate the rate at which electrons with energy $E = E_{\rm esc} + E_{\rm kin}$ escaped from the cluster using Eq. (5.33). Integrated through the timescale of a pulse until the evaporation has stopped, this yields an ejected electron spectrum for a single cluster exposed to the pulse. Since the clusters are located randomly with respect to the center of the laser pulse, a further spatial integration over the radial dimension of the pulse, assuming a Gaussian laser profile $I(r) \propto e^{-r^2/\sigma^2}$ from 0 to 3 σ was necessary. The length of the interaction region in the Hamburg experiment was comparable to the Rayleigh range for the laser; accordingly, the laser intensity along the direction of propagation was assumed to be constant. After performing the spatial integration, on average .22 electrons per xenon atom were found to have evaporated from the cluster in this way. The spectrum of ejection energies for these electrons shown in Fig. 5.5, although not exponential, is nevertheless quite similar to the electron spectrum found in Ref. [30].

The largest discrepancy between this calculated spectrum and the spectrum from [30] occurs at low ejection energy. In addition, the current model of the cluster expansion predicts that the majority of electrons will comprise electron plasmas which remain bound to the cluster ions and become quite cold during the process of expansion. These electrons – the great bulk of the population – would reach the detector at low energies and after long delay times, further boosting the spectrum at low energies. However, Laarmann *et al* note that for $E_{\rm kin} < 2.5$ eV, coinciding with the region of largest discrepancy, the spectrum cannot be evaluated due to large levels of noise in the background spectra.

Since electrons faster than about 1 eV are ejected from the cluster during the pulse rather than during the slower process of cluster expansion, the ejected electron spectrum has the potential to serve as a window into the nature of the laser–cluster interaction. Accordingly, Fig. 5.6 gives the spectra for 1500 atom clusters exposed to a

100 fs, 7×10^{13} W/cm^2 pulse, and for 2500 atom clusters exposed to a 50 fs, 2.5×10^{13} W/cm^2 pulse.

The calculated spectrum was different for different models of plasma screening. After spatial averaging, 1500 atom clusters exposed to a 100 fs, 7×10^{13} W/cm^2 pulse were found to eject 0.22 electrons per atom during this early evaporation period using the Wigner-Seitz cutoff model for the screening length (see section 5.5 for a discussion of plasma screening). Using the Attard model, 0.07 electrons per atom are evaporated during this period. For 2500 atom clusters exposed to a 50 fs, 2.5×10^{13} W/cm^2 pulse, the corresponding numbers are 0.13 electrons per atom for the Wigner-Seitz cutoff model and 0.02 electrons per atom for the Attard model. In contrast to this, the Hamburg experiment measured an average charge per ion of 2.98. Hence, the electrons which comprise these ejected electron spectra correspond to only a few percent of all free electrons at the time when the expanding clusters reach the detector.

5.5 Nonideal Plasma Screening

As shown in Fig. 5.8, when plasma screening of the Xe ions becomes strong enough to allow photoionization of Xe^+ into Xe^{2+}, large numbers of extremely low-energy electrons are added to the plasma. As a result, the ratio of electron kinetic energy to electrostatic potential energy falls dramatically, the Debye length of the plasma falls abruptly below the Wigner-Seitz radius of xenon, and the plasma enters a regime of strong correlation. In this regime, a number of the assumptions of Debye-Hückel screening model break down, and the Debye length loses its meaning as a screening distance [18]. If the plasma cools sufficiently, screening lengths can become complex, and result in oscillatory electron–ion correlation functions [31, 3].

Another possibly important effect of the strongly coupled plasma was identified in a recent study [25], which has identified electron dynamics in a strongly coupled plasma as having a very large impact upon rates of many-body recombination and hence upon

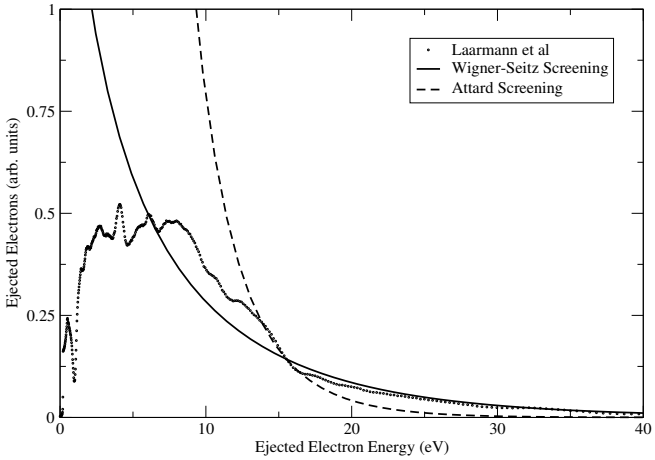

Figure 5.5: Ejected electron spectrum. Comparison between data from [30] and spatially-averaged spectra calculated using 70 atom clusters exposed to a 4.4×10^{12} W/cm^2, 100 fs pulse for two different models of plasma screening. The Wigner Seitz cutoff model uses the ordinary Debye length as the screening radius, but the screening radius is not allowed to fall below xenon's Wigner-Seitz radius at liquid density, 4.64 bohr. The Attard model of screening calculates the screening radius according to equation (5.34), discussed in Section 5.5. The spectrum calculated using xenon's Wigner-Seitz radius as a minimum screening distance displays a strong similarity to the experimental curve. The intensity of the experimental spectra is arbitrary; magnitudes were chosen by setting each curve equal at the beginning of the exponential tail in the experiment. Figure taken from [64].

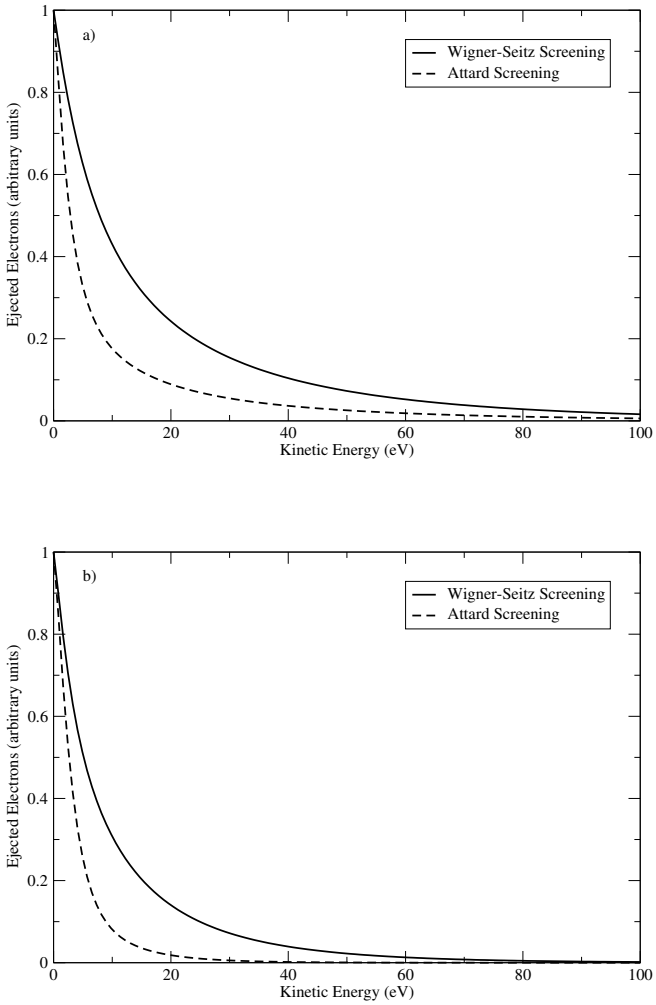

Figure 5.6: Ejected electron spectra, calculated for the two sets of parameters and the two models of screening. The Wigner Seitz cutoff model uses the ordinary Debye length as the screening radius, but the screening radius is not allowed to fall below xenon's Wigner-Seitz radius at liquid density, 4.64 bohr. The Attard model of screening calculates the screening radius according to equation (5.34), discussed in section 5.5. a) Nature parameters: 1500 atom clusters exposed to a 100 fs, 7×10^{13} W/cm^2 pulse. b) Thesis parameters: 2500 atom clusters exposed to a 50 fs, 2.5×10^{13} W/cm^2 pulse. Since electrons faster than about 1 eV are ejected from the cluster during the pulse the ejection spectra could serve as a window into the dynamics of the laser-cluster interaction. Figure taken from [64].

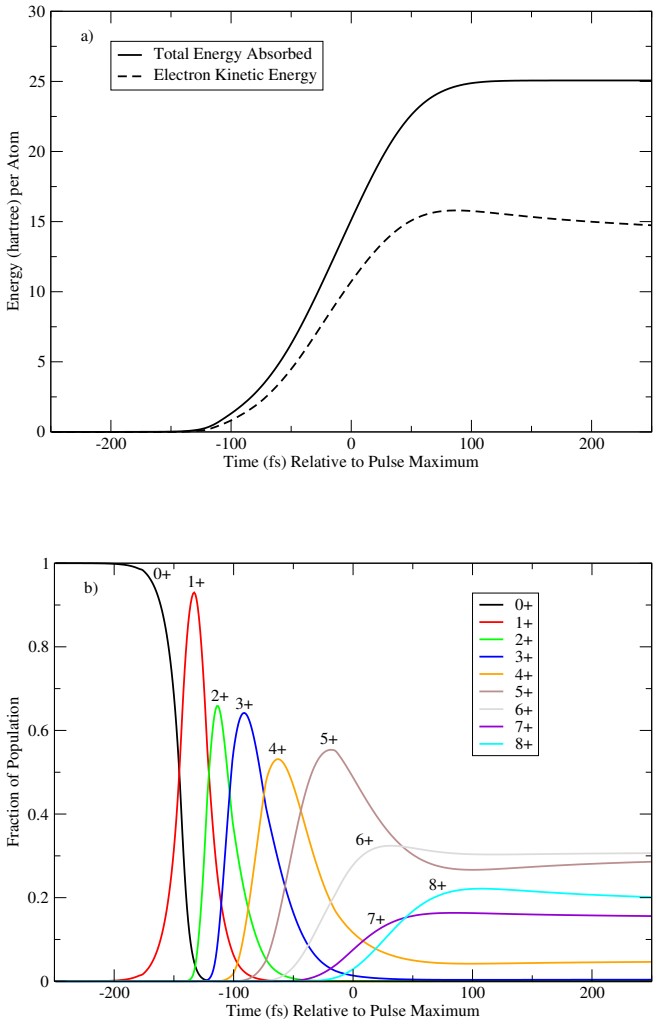

Figure 5.7: The effects of collisional ionization and recombination are to allow the formation of charge states beyond Xe^{3+} Pictured is the time evolution of a single 1500 atom cluster exposed to a 100 fs, 7×10^{13} W/cm^2 pulse. These states enhance the rate of inverse bremsstrahlung heating. As the plasma expands and cools, the chemical equilibrium shifts toward lower charge states on a timescale much longer than the laser pulse, until decreasing plasma density causes recombination and ionization rates to go to zero. a) Energy absorbed vs. time b) Ionic population vs. time during laser pulse. Figure taken from [64].

energy absorption by the cluster as the recombined ions undergo multiple episodes of photoionization.

Most calculations performed in this chapter were performed using xenon's Wigner-Seitz radius at liquid density as a minimum value below which the screening was not allowed to fall. Clearly, with the precise nature of screening unknown in the strongly correlated regime, the method of calculating atomic properties based on a Debye-screened atomic potential acquires a corresponding uncertainty. Accordingly, as an attempt to estimate this uncertainty, the evolution of the cluster was calculated using different models for the screening length.

The simplest approximation applied xenon's Wigner-Seitz radius at liquid density as a minimum value below which the screening length was not allowed to fall. A second model, proposed by Attard [3], deals with ions having a nonzero radius. Strictly speaking, the Debye-Hückel model for plasma screening is invalid except in the limit of ions which have zero size. Attard has shown that in the case where ions have a nonzero hard-sphere radius d, the screening length $\lambda = 1/\kappa$ differs from the classical Debye-Hückel length $\lambda_D = 1/\kappa_D$ according to

$$\kappa = \frac{\kappa_D}{\sqrt{1 - (\kappa_D d)^2/2 + (\kappa_D d)^3/6}} \, . \tag{5.34}$$

This effect becomes important in the domain where $\lambda_D \leq d$.

Qualitatively, the effect of considering screening lengths in this model which are shorter than the Wigner-Seitz radius is twofold. First, the tighter screening slightly decreases inverse bremsstrahlung heating. Secondly, it allows photoionization of Xe^{3+} and higher charge states. Directly substituting the Attard screening length for the Debye length with Wigner-Seitz cutoff therefore gives some insight as to how sensitive the results in this chapter are to different models of the ionic potential under very strong screening. As can be seen in Fig. 5.9 the Attard screening model has a relatively small impact on the prediction for the energy absorbed by the cluster. More prominent

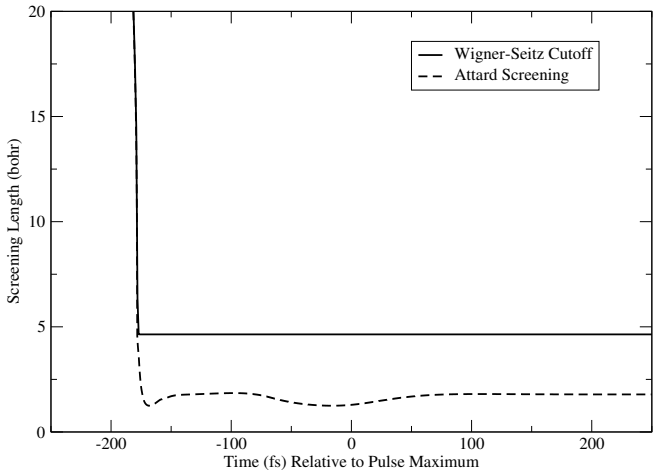

Figure 5.8: The interaction of plasma screening with atomic potentials is unknown as the screening length becomes very short. Here the screening length vs time is given for two simulations of a 1500 atom cluster exposed to a 100 fs, 7×10^{13} W/cm^2 pulse, using two models for screening. In the first model, the screening length is not allowed to fall below xenon's Wigner-Seitz radius at liquid density. The second model for screening uses a formula given by Attard. Figure taken from [64].

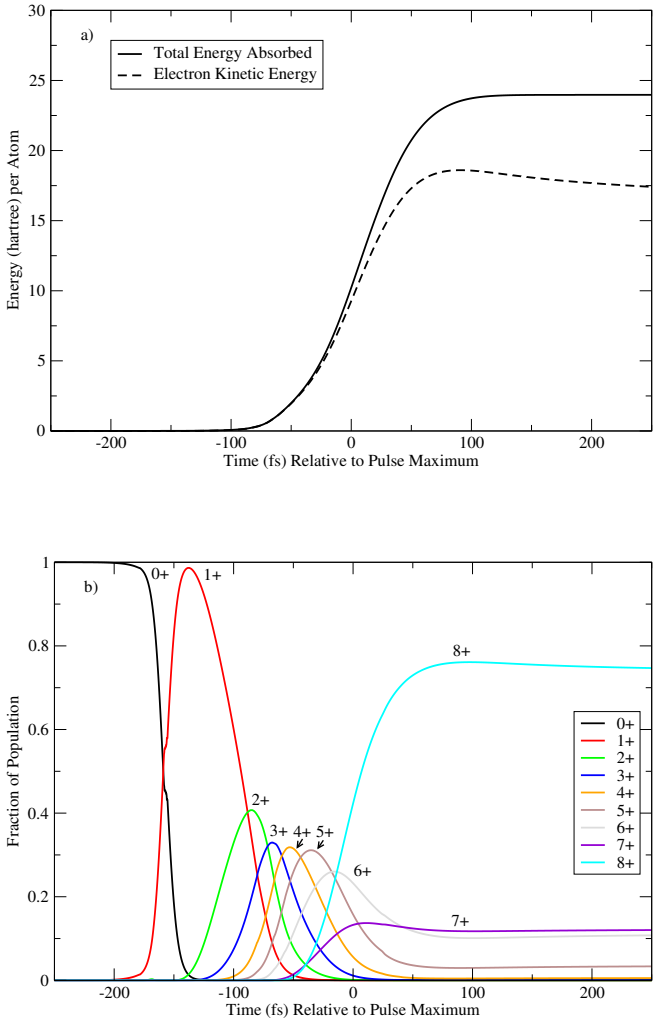

Figure 5.9: Near the center of the pulse, calculating the evolution of the cluster using Attard screening yields screening lengths shorter than the Wigner-Seitz cutoff, allowing easier formation of high charge states than when the evolution is calculated for Wigner-Seitz screening, shown in Figure 5.7. For a 1500 atom cluster exposed to a 7×10^{13} W/cm^2, 100 fs pulse: a) Energy absorbed vs time for the Attard screening model, b) Charge species population vs time for the Attard screening model. Figure taken from [64].

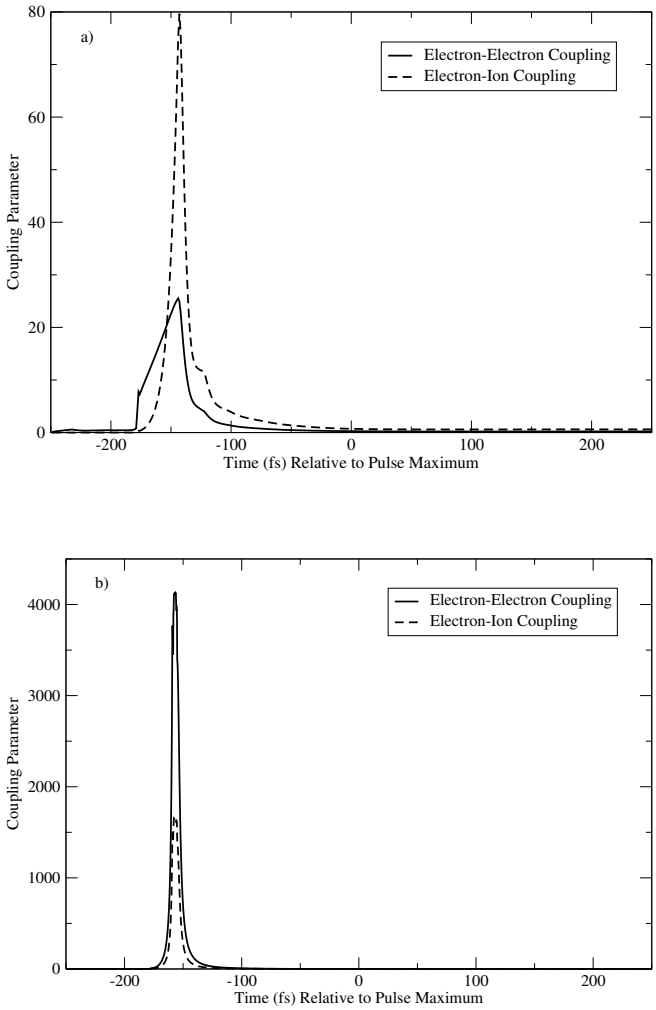

Figure 5.10: Plasma coupling parameter vs. time for the two models of plasma screening. The coupling parameters are defined by $\Gamma_{ee} = \frac{1}{aT}$ and $\Gamma_{ei} = Z\Gamma_{ee}^{3/2}$ where the average distance between electrons a is given by $a = (\frac{3}{4\pi n_e})^{1/3}$ and Z is the average charge of the ions. The plasma becomes very strongly coupled early in the pulse, but the strength of the coupling decreases as the plasma absorbs more energy in the course of the cluster heating. a) Coupling parameters vs. time using Wigner-Seitz cutoff. b) Coupling parameters vs. time for the Attard screening model. Figure taken from [64].

is the formation of higher charge states, which is abetted by the reduced ionization potentials resulting from the tighter screening in the Attard model. Figure 5.10 shows the plasma coupling parameter, a measure for the nonideality of a plasma, for the two models, demonstrating that the Attard screening model gives rise to a more strongly coupled plasma than the pure Debye model. In addition, the two models give different populations for the various charge states at the end of the pulse; however, the combined effects of the cluster expansion and spatial averaging over the beam profile act to destroy much of this information.

As a further test of our model's sensitivity to plasma screening lengths, the evolution of the cluster was calculated in the limit of weak screening. To do this, the screening length in the cluster was fixed at 100 bohr for the entire duration of the laser pulse. In this limit, ionization potentials are unchanged from their values in the absence of screening, and photoionization beyond Xe^+ is impossible. In this model, formation of states with charge 2 or higher must come entirely from collisional ionization. The results of this constraint can be seen in Figure 5.13. Neglecting the effects of plasma screening in this way inhibits the formation of high charge states in the cluster, yielding virtually no Xe^{7+} or Xe^{8+}. After the initial photoionization of neutral xenon, the plasma undergoes a period of slow heating while the laser intensity builds. Near the maximum of the pulse, the plasma becomes energetic enough to ionize the higher charge states with their unscreened ionization potentials, and the rate of inverse bremsstrahlung heating increases rapidly. The total energy absorbed falls from 25 hartree per atom in the case of the Wigner-Seitz cutoff model to 11.5 hartree in the limit of no screening.

5.6 Hydrogenic Model of Inverse Bremsstrahlung

Most previous approaches to the problem of laser-cluster interactions have considered the ionic potential seen by the electron as a pure Coulomb potential. This is not an unreasonable approximation: as the charge of the ion increases, the difference between

inverse bremsstrahlung cross sections calculated using Herman Skillman potentials and cross sections calculated using Coulomb potentials is much smaller than in the case of the bare ion. This can be seen in figure 5.11, which contrasts inverse bremsstrahlung cross sections calculated using Coulomb and Herman-Skillman potentials for ions of charge 5.

As can be seen in figure 5.7b, when the laser reaches maximum intensity, most of the cluster has been ionized to such high charge states. Thus, models of the inverse bremsstrahlung process which use Coulombic potentials should be able to see comparable levels of heating to those using cross sections derived using Herman-Skillman potentials.

To investigate this proposition, the laser-cluster interaction for a 1500 atom cluster exposed to a 100 fs, 7×10^{13} W/cm^2 was simulated using the model presented in this chapter, but with a physical picture chosen to emulate that of Siedschlag and Rost [52]. The simulation used inverse bremsstrahlung cross sections calculated with Debye-screened Coulomb potentials. Ionization potentials and photoionization cross sections were unchanged from the other simulations. The unaltered Debye length was used as the screening length. Collisional ionization and recombination were not considered.

The results of this simulation are presented in figure 5.12. Levels of energy absorption were found which were very comparable to those in the model using Herman-Skillman potentials, but the behavior of ionic populations with time was very different. Xe^{7+} and Xe^{8+}, which make up almost half of the population of the cluster at the end of the pulse in the Herman-Skillman model, were present in negligible quantities.

Both differences between the two physical pictures are attributable to the effects of collisional ionization and recombination. Recombination slows the growth of high charge state populations by allowing some photoionized ions to recombine into a lower charge state, while collisional ionization allows the population of charge states which cannot be created via sequential photoionization.

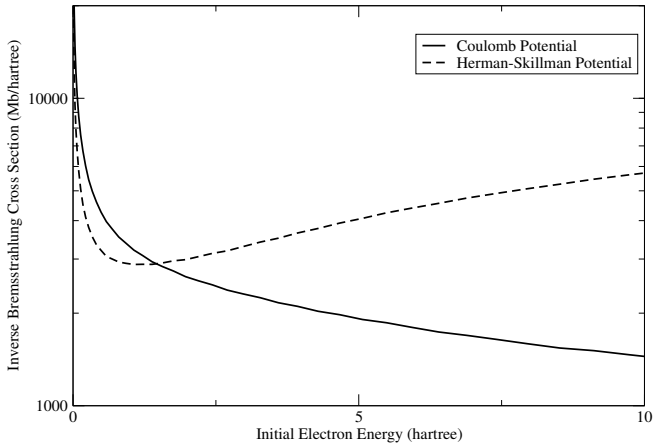

Figure 5.11: Inverse bremsstrahlung cross sections [Eqs. 5.13 and 5.14] calculated for an electron in the field of a purely Coulombic 5+ potential and for an electron in the field of a Xe Herman-Skillman atomic potential of the same charge. In comparison with figure 5.1, it can be seen that at higher charge states, the impact of atomic structure on inverse bremsstrahlung cross sections is decreased. Figure taken from [64].

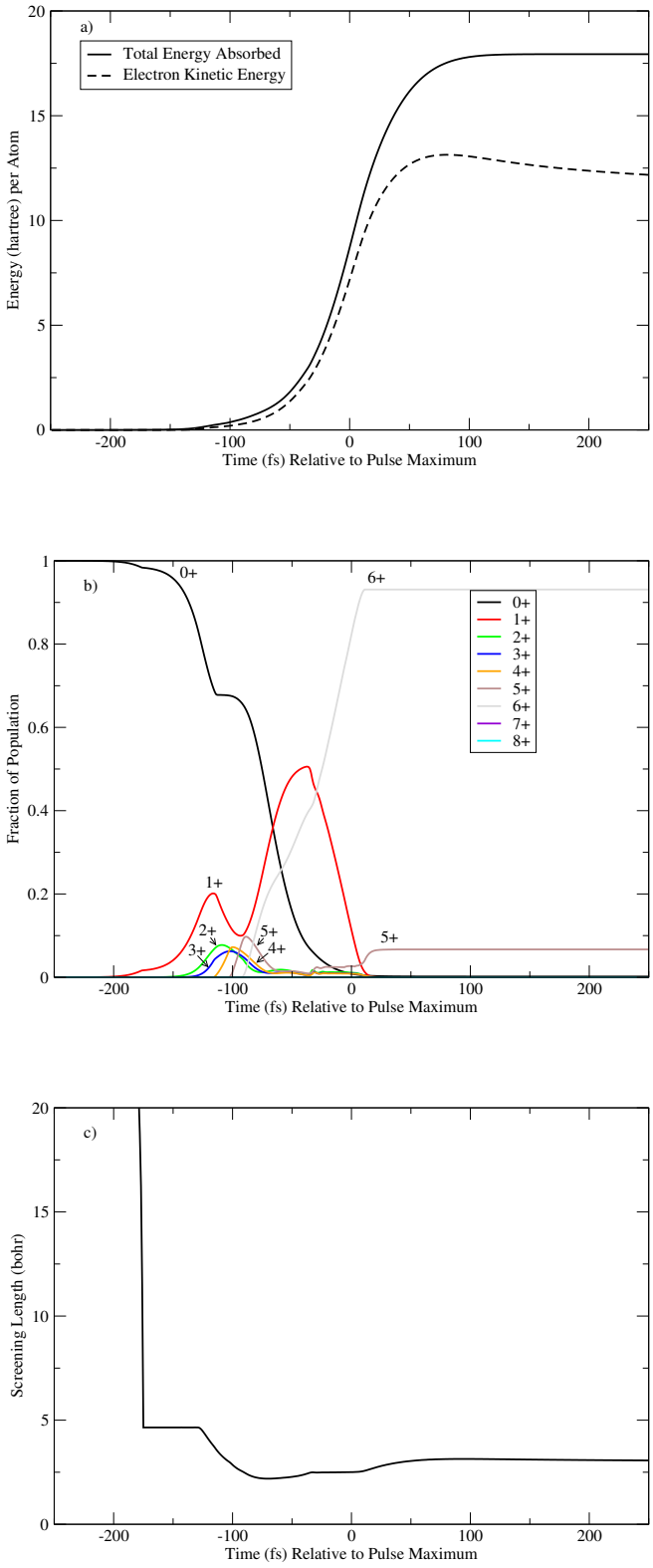

Figure 5.12: Simulation of the laser-cluster interaction using a physical model taken from [52]. In this model, inverse bremsstrahlung cross sections are calculated using hydrogenic potentials and all high charge states are produced via sequential photoionization. Collisional ionization and recombination are not considered. a)Energy absorbed vs time. b) Charge state population vs time. c) Debye length vs time. Figure taken from [64].

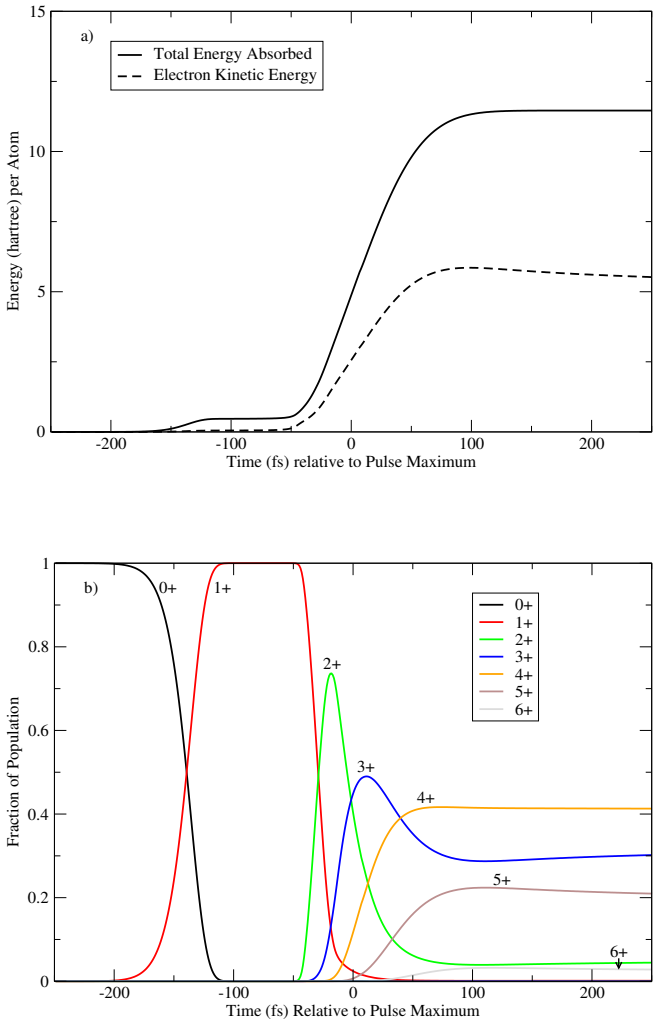

Figure 5.13: Evolution of the cluster calculated in the limit of long screening length, $\lambda_D = 20$ bohr for a 1500 atom cluster exposed to a 100 fs, 7×10^{13} W/cm^2 pulse. Weak screening prevents ionization potential lowering due to plasma effects, and precludes photoionization past Xe^+. The effect of neglecting plasma screening effects is to reduce formation of high charge states and to reduce the total energy absorbed by the cluster. The pulse and cluster parameters are identical to those used in Figures 5.3, 5.7 and 5.9. a) Energy absorbed vs. time b) Ionic population vs. time during laser pulse. Figure taken from [64].

5.7 Summary and Conclusions

When a xenon cluster is irradiated by intense VUV light, there are four phases in its evolution. In the first phase, electrons are liberated from the xenon atoms and form a plasma. As the number of free electrons grows, the screening length of the plasma shrinks.

Once the screening length of the plasma reaches 10.6 bohr, Xe^{1+} can undergo photoionization into Xe^{2+}. This results in the addition of large numbers of low-energy electrons to the plasma, cooling it and decreasing the screening length still further. The ratio of kinetic energy to potential energy falls dramatically, and the plasma temporarily becomes strongly coupled. Ionization potentials for higher charge states fall with increased screening, facilitating their creation.

In the third phase, the plasma undergoes rapid inverse bremsstrahlung heating. High charge states are formed through collisional ionization and recombination, and the cluster becomes charged as energetic electrons evaporate away from its surface. The charge state distribution shifts rapidly toward higher charges, with the average ionic charge reaching 5.5 at the pulse peak. This distribution changes only slowly on the timescale of the pulse.

Finally, the cluster expands due to the pressure of the electron gas and the cluster's own charge. As the cluster expands, the electron plasma cools and becomes more diffuse. Screening lengths increase, and charge state equilibrium shifts toward lower charge states.

Of these four phases, the model presented here describes the first and third phases well; the second more crudely. The dynamics of the expanding cluster are a challenging problem in their own right, and demand a treatment more sophisticated than the current simple homogeneous expansion model.

For strongly coupled plasmas, it is unclear whether this treatment of plasma

screening adequately describes the potential seen by scattering or photoionizing electrons. As the Debye length falls below the Wigner-Seitz radius, the interaction of screening effects due to inner-shell electrons and effects due to screening by continuum plasma electrons should be considered. It is known that the screening length diverges from the Debye length in this limit, but the precise nature of the electron–ion potential is unknown.

There is some difficulty in comparing these results to the Hamburg experiment, due to experimental uncertainty in laser intensity, temporal profile, spatial profile, and cluster size. Whereas in the Nature paper the Hamburg group described the laser pulse as 100 fs, 7×10^{13} W/cm^2 incident on 1500 atom xenon clusters, Wabnitz's thesis [62] subsequently describes these pulses as 50 fs, 2.5×10^{13} W/cm^2 pulses incident on 2500 atom clusters. In addition, the temporal profile of the laser pulses is not Gaussian, and varies in an unpredictable way from pulse to pulse due to the nature of the SASE amplification process, which starts from shot noise.

This model also has difficulty explaining the properties of the clusters long after the laser-cluster interaction is over. As the clusters expand and cool, they continue to undergo collisional ionization and recombination. The distribution of charge states measured at the experimental detectors bears no simple relationship to the distribution calculated at the end of the pulse. The homogeneous model of the cluster expansion implicitly requires that all charge states in the same cluster have the same average kinetic energy; this obviously conflicts with the quadratic dependence of energy vs charge state detected in the Hamburg experiment. Also, it is likely that high charge states escape the cluster more quickly than low charge states, spending less time in regions of high electron density and having less opportunity to recombine. Thus, a more sophisticated model of the cluster expansion is necessary in order to predict final charge state and ionic energy distributions with confidence for comparison with experiment.

At the center of a gaussian laser pulse using parameters taken from the Nature

paper and a Wigner-Seitz debye length cutoff, each cluster absorbs on average 682 eV per atom. At a distance of 3 sigma from the center of such a gaussian pulse, each cluster absorbs only .4 eV per atom. Spatial averaging over the gaussian pulse profile from 0 to 3 sigma gives an average of 195 eV per atom absorbed. Using the less intense parameters from Wabnitz's thesis gives 219 eV per atom at the center, 0.2 eV per atom at 3 sigma, and 65 eV per atom on spatial averaging.

Using a time of flight detector which could detect only charged ions, Wabnitz *et al.* reported an average ion energy of 400 eV, subsequently revised to 650 eV.

Clearly, a spatial average such as the one performed here could be altered by averaging over a different beam profile or by changing the limits of the radial average and including more clusters which are exposed to only a tiny fraction of the beam's peak intensity. It is also clear that most of the atoms in the clusters which are exposed to very small fractions of the peak intensity will never be ionized and thus would not register in a time-of-flight ion detector such as was used in the Hamburg experiment. Thus, in the absence of better information about the beam's spatial and temporal profile and a more comprehensive model of the cluster expansion after the conclusion of the laser pulse, it is impossible to make precise comparisons between this model and the Hamburg results.

Nevertheless, this model of the laser-cluster interaction explains some surprising features of the laser-cluster interaction in the VUV regime quite well. Primary among these is the surprising efficiency by which the clusters absorb photons. Second, the high charge states observed in the Hamburg experiment here emerge quite naturally. Third, the same model is able to calculate the early electron ejection spectrum measured in [30] and achieved great similarity to experiment, despite a cluster size and pulse intensity which differ significantly from those of the original Hamburg experiment. Such spectra can depend strongly on the model of plasma screening or the precise parameters of the experiment, and can therefore serve as a possible window into the nature of the

laser-cluster dynamics during the time period of the pulse.

Chapter 6

Summary, Conclusions and Outlook

This thesis has investigated the ways in which atomic and molecular physics are affected by the presence of an intense laser field. Chapter 2 examined how the familiar concept of a shape resonance is altered by the intense and time-varying field of the driving laser, while chapter 3 investigated how molecular scattering states affect experimental observables such as the high harmonic spectrum, as well as the implications for attempts to reconstruct molecular properties from such information. Chapter 4 investigated how the internal degrees of freedom in a molecule can measurably affect high harmonic experiments. Chapter 5 examined the physically different scenario of a laser-cluster interaction, in which atomic properties are altered by interaction with a cluster plasma rather the driving laser.

As is not surprising for such a young field, the work presented in this thesis can hardly be said to encompass everything which could be done. The most obvious omission from this thesis is a satisfactory treatment of molecular ionization in a strong field. Effects such as polarization of the molecular core or ionization from multiple orbitals have barely been considered here, and in nowhere near the depth they deserve.

In the longer run, more elaborate treatments of the molecular wavefunction offer great potential as ways to look at molecular dynamics on an ultrafast timescale. A simple variation of the quantum interference experiment described in chapter 4 would be to use the first laser pulse to start some chemically interesting process such as a change

of molecular conformation and then to use the second pulse as an interferometric probe of the vibrational wavefunction dynamics. Another particularly attractive possibility would be to investigate vibronic dynamics in the vicinity of a conical intersection by ionizing a symmetric molecule near the symmetry point and examining how the vibrational wavefunction affected the electronic dynamics in the ion. Such experiments could close the loop: atomic and molecular ideas, once understood in the exotic regime of intense laser physics, could in turn provide a new window to look at chemical dynamics on previously unreachable timescales.

To return to the train metaphor from the introduction, a bright glare shining in through the windows does not fundamentally alter the interactions between the passengers, but it may serve to illuminate those interactions better than a static seating arrangement could. The fact that you avoid the boor to your front and gravitate toward your friends in the back could be an accident in any particular seating chart, but would be rapidly apparent after the cabin has rearranged itself a few times. Likewise, the goal of dealing with atoms and molecules in intense laser fields is not merely to do atomic and molecular physics in an exotic regime, but also as a means of learning about normal molecules in normal environments.

Bibliography

[1] N. Wagner, private communication.

[2] In practice, matrix elements involving large values of l were found to converge very quickly to zero. Because of this, the total transition rate from states of energy E to states of energy E', and hence the heating, is unaffected by the existence of a cutoff.

[3] Phil Attard. Phys. Rev. E, 48:3604, 1993.

[4] M. Aymar, C. H. Greene, and E. Luc-Koenig. Rev. Mod. Phys., 68:1015, 1996.

[5] I.B. Bersuker. The Jahn-Teller effect and vibronic interactions in modern chemistry. Plenum Press, 1984.

[6] V. Carravetta, Y. Luo, and H. Agren. Chem. Phys., 174:141, 1993.

[7] P. B. Corkum. Phys. Rev. Lett., 71:1994, 1993.

[8] C. Deiss, N. Rohringer, J. Burgdoerfer, E. Lamour, C. Prigent, and D. Vernhet. Journal de Physique IV, 138:55, 2006.

[9] T. Ditmire, T. Donnelly, R. W. Falcone, and M. D. Perry. Phys. Rev. Lett., 75:3122, 1995.

[10] T. Ditmire, T. Donnelly, A. M. Rubenchik, R. W. Falcone, and M. D. Perry. Phys. Rev. A, 53:3379, 1996.

[11] T.H. Dunning Jr. Gaussian basis sets for use in correlated molecular calculations. i. the atoms boron through neon and hydrogen. Journal of Chemical Physics, 90(2):1007–1023, 1989.

[12] A. R. Edmonds. Angular Momentum in Quantum Mechanics. Princeton University Press, Princeton, New Jersey, 1996.

[13] Shalom Eliezer. The Interaction of High-Power Lasers with Plasmas. Institute of Physics Publishing, Bristol and Philadelphia, 2002.

[14] B. D. Esry and Chris H. Greene. unpublished, 1995.

[15] S. Estreicher and T. L. Estle. Phys. Rev. B, 31:5616, 1985.

[16] M. J. Frisch et al. Gaussian 98. Gaussian Inc., Pittsburgh, PA, 1998.

[17] V. Ayvazyan et al. Phys. Rev. Lett., 88:104802, 2002.

[18] Vladimir E. Fortov and Igor T. Iakubov. The Physics of Non-Ideal Plasma. World Scientific, Singapore, 2000.

[19] Harald Friedrich. Theoretical Atomic Physics. Springer Verlag, Berlin, 1991.

[20] H. Goldstein, C. Poole, and J. Safko. Classical Mechanics, Third Edition. Addison Wesley, 2002.

[21] M. C. Gutzwiller. Chaos in Classical and Quantum Mechanics. Springer, New York, 1990.

[22] F. Herman and S. Skillman. Atomic Structure Calculations. Prentice-Hall, Englewood Cliffs, N.J., 1963.

[23] M. H. R. Hutchinson, T. Ditmire, E. Springate, J. W. G. Tisch, Y. L. Shao, M. B. Mason, N. Hay, and J. P. Marangos. Phil. Trans. R. Soc. Lond. A, 356:297, 1998.

[24] J. Itatani, J. Levesque, D. Zeidler, Hiromichi Niikura, H. Pepin, J. C. Kieffer, P. B. Corkum, and D. M. Villeneuve. Nature, 432:867, 2004.

[25] C. Jungreuthmayer, L. Ramunno, J. Zanghellini, and T. Brabec. J. Phys. B., 38:3029, 2005.

[26] S. Kazamias and P. Balcou. Physical Review A, 69:063416, 2004.

[27] D. A. L. Kilcoyne, S. Nordholm, and N. S. Hush. Chemical Physics, 107:197, 1986.

[28] J. L. Krause, K. J. Schafer, and K. C. Kulander. Phys. Rev. A, 45:4998, 1992.

[29] W. L. Kruer. The Physics of Laser Plasma Interactions. Westview Press, Boulder,Colorado, 2003.

[30] T. Laarmann, M. Rusek, H. Wabnitz, J. Schulz, A. R. B. de Castro, P. Guertler, W. Laasch, and T. Moeller. Phys. Rev. Lett., 95:063402, 2005.

[31] Benjamin P. Lee and Michael E. Fisher. Phys. Rev. Lett., 76:2906, 1996.

[32] M. Lein. J. Phys. B, 40:R135, 2007.

[33] M. Lewenstein, P. Balcou, M.Y. Ivanov, A. L'Huillier, and PB Corkum. Phys. Rev. A, 49:2117, 1994.

[34] M. Lewenstein, Ph. Balcou, M. Yu. Ivanov, A.L'Huillier, and P. B. Corkum. Phys. Rev. A, 49:2117, 1994.

[35] M. Lezius, S. Dobosz, D. Normand, and M. Schmidt. Phys. Rev. Lett., 80:261, 1998.

[36] Wolfgang Lotz. Zeitschrift fur Physik, 216:241–247, 1968.

[37] W. H. Miller. J. Phys. Chem. A, 105:2942, 2001.

[38] W. Moffitt and W. Thorson. Phys. Rev., 108:1251, 1957.

[39] T. Morishita, A. T. Le, Z. Chen, and C. D. Lin. preprint.

[40] H. Nakamura. J. Theor. Comp. Chem., 4:127, 2005.

[41] L. Nugent-Glandorf, M. Scheer, D. A. Samuels, V. M. Bierbaum, and S. R. Leone. J. Chem. Phys., 117:6108, 2002.

[42] S. Patchkovskii, Z. Zhao, T. Brabec, and D. M. Villeneuve. J. Chem. Phys., 126:114306, 2007.

[43] J. Plenge, C. Nicolas, A. G. Caster, M. Ahmed, and S. R. Leone. J. Chem. Phys., 125:133315, 2006.

[44] William H. Press, Saul A. Teukolsky, William T. Vetterling, and Brian P. Flannery. Numerical Recipes in Fortran 77. Cambridge University Press, Cambridge, England, 2001.

[45] T. N. Rescigno and C. W. McCurdy. Physical Review A, 62:032706, 2000.

[46] Manuel Rotenberg. The 3-j and 6-j Symbols. Technology Press, Cambridge, Massachusetts, 1959.

[47] R. Santra and A. Gordon. Phys. Rev. Lett., 96:073906, 2006.

[48] R. Santra and C. H. Greene. Phys. Rev. A, 70:053401, 2004.

[49] Robin Santra and Chris H. Greene. Phys. Rev. Lett., 91:233401, 2003.

[50] A. Scrinzi and N. Elander. J. Chem. Phys, 98:3866, 1992.

[51] Y. L. Shao, T. Ditmire, J. W. G. Tisch, E. Springate, J. P. Marangos, and M. H. R. Hutchinson. Phys. Rev. Lett., 77:3343, 1996.

[52] Christian Siedschlag and Jan-Michael Rost. Phys. Rev. Lett., 93:043402, 2004.

[53] O. Smirnova, M. Spanner, and M. Ivanov. J. Phys. B, 39:S307, 2006.

[54] G. Snell, U. Hergenhahn, N. Mueller, M. Drescher, J. Viefhaus, U. Becker, and U. Heinzmann. Phys. Rev. A, 63:032712, 2001.

[55] A. F. Starace. Phys. Rev. B, 5:1773, 1972.

[56] J. Sugar. Physical Review B, 5(5):1785, 1972.

[57] S. Tonzani. Comp. Phys. Comm., 176:146, 2007.

[58] S. Tonzani and C. H. Greene. J. Chem. Phys., 122:014111, 2005.

[59] S. Tonzani and C. H. Greene. J. Chem. Phys., 124:054312, 2006.

[60] H. Wabnitz, L. Bittner, A. R. B. de Castro, R. Doehrmann, P. Guertler, T. Laarmann, W. Laasch, J. Schulz, A. Swiderski, K. von Haeften, T. Moeller, B. Faatz, A. Fateev, J. Feldhaus, C. Gerth, U. Hahn, E. Saldin, E. Schneidmiller, K. Sytchev, K. Tiedtke, R. Treusch, and M. Yurkov. Nature, 420:482, 2002.

[61] H. Wabnitz, A. R. B. de Castro, P. Guertler, T. Laarmann, W. Laasch, J. Schulz, and T. Moeller. Phys. Rev. Lett., 94:023001, 2005.

[62] Hubertus Wabnitz. Interaction of Intense VUV Radiation from a Free-Electron Laser with Rare Gas Atoms and Clusters. PhD thesis, Universitat Hamburg, 2003.

[63] N. L. Wagner, A. Wuest, I. P. Christov, T. Popmintchev, X. Zhou, M. M. Murnane, and H. C. Kapteyn. Proc. Natl. Acad. Sci. U.S.A., 103(36):13279, 2006.

[64] Z. Walters, R. Santra, and C. H. Greene. Phys. Rev. A, 74:043204, 2006.

[65] Z. Walters, S. Tonzani, and C. H. Greene. J. Phys. B, 40:F277, 2007.

[66] Z. B. Walters, S. Tonzani, and C. H. Greene. J. Phys. Chem. A, 112:9439–9447, 2008.

[67] Ya. B. Zel'dovich and Yu. P. Raizer. Physics of Shock Waves and High-Temperature Hydrodynamic Phenomena. Academic Press, New York and London, 1966.

[68] B. Ziaja, A. R. B. de Castro, E. Weckert, and T. Moeller. European Physics Journal D, 40:465, 2006.

[69] B. Ziaja, H. Wabnitz, E. Weckert, and T. Moeller. New Journal of Physics, 10:043003, 2008.

[70] B. Ziaja, H. Wabnitz, E. Weckert, and T. Moeller. European Physics Letters, 82:24002, 2008.